Doctoral Dissertation
Doctoral Program in Material Science and Technology (34th Cycle)

Sustainable Methods for Lithium Recovery from Water and Unconventional Resources

Luisa Baudino

******

Supervisors
Prof. A. Lamberti, Supervisor
Prof. C. F. Pirri , Co-Supervisor

Doctoral Examination Committee:
Dr. D. Brogioli, Referee, University of Bremen
Dr. A. Sanson, Referee, CNR-ISTEC
Dr. A. Sacco, Istituto Italiano di Tecnologia
Prof. F. Bella, Politecnico di Torino
Prof. E. Tresso, Politecnico di Torino

Politecnico di Torino
2022

Declaration

I hereby declare that, the contents and organization of this dissertation constitute my own original work and does not compromise in any way the rights of third parties, including those relating to the security of personal data.

Luisa Baudino

2022

* This dissertation is presented in partial fulfillment of the requirements for **Ph.D. degree** in the Graduate School of Politecnico di Torino (ScuDo)

I would like to dedicate this thesis
to my biggest cheerleader,
my grandmother Gianna

Acknowledgments

This work could not have been possible without the help and support of several groups of people, each with very different backgrounds and roles.

First of all, I would like to thank my academic support system, which spans from my supervisors, to my colleagues and even the students I had the opportunity and pleasure to tutor and teach. Each of these facets of the academic world allowed me to discover different sides of myself and to grow into the person I am (hopefully a decent enough human being). I would like to particularly thank Prof. Andrea Lamberti, my supervisor, who parachuted me into both the research and teaching world at lightning speed and with way more faith in my skills than I ever allowed myself to have. We may have bickered, and will probably continue doing so in the future, but you know I've always appreciated you and only did it out of affection and respect. I would also like to thank our research group leader, Prof. Fabrizio Pirri, and everyone else who helped me both in my didactic and research activities among which are Prof. Elena Tresso, Mara Serrapede, Nadia Garino, Micaela Castellino, Monica Barale, Stefano Bianco, Marco Laurenti.

Pietro Zaccagnini and Alessandro Pedico, you were the first supports I had in my research and the ones I relied most on whenever I had any trouble. You truly were my crutches and I could never thank you enough for your continuous patience. To all of my colleagues from the lab and the office, who brought me coffee when I was too taken by the students to remember it, who left me notes on my computer when I stayed too many hours in the lab, and who endured the sound of my tea kettle whenever I was writing or studying, thank you. Among those: Anna Aixalà Perellò, Davide Arcoraci, Nicolò Cacocciola, Marwan Channab, Marzia Conte, Vittorio Fra, Fabio Michieletti, Gianluca Milano, Giorgio Mogli, Davide Molino, Andrea Napolitano, Gianluca Palmara, Nicolò Percivalle, Federico Raffone, Marco Reina, Mattia Salomone, Clara Salvini, Matteo Segantini, Francesco Seller, Roberto Speranza, Veronica Vighetto. Thank you to the former students who kept working with us even after having me as a teacher and who helped me become an even better one (*group 4* you know who you are) and to those that left us but still talk to me after being their teacher.

To my *lunch group* from the chemistry wing, which in the years lost and acquired several people. When I started having lunch with you at the beginning of my PhD journey, it was mostly Luigi Capozzi, Prof. Marco Sangermano, Nicolò Razza, Marco Bazzano, Andrea Arsiccio, Angelo Romano, Duccio Gallichi Nottiani, Graziano Frungieri, and of course my wonderful work wife Fiora Artusio. I will not spend many words describing all the fun and relaxing times we had coupled with interesting and stimulating conversations. In the past years, people came and went from this group, to name a few, Michael Zanon, Merve Betul Adali, Maitê Harguindeguy, Manuel Peters, but almost everyone left Politecnico as of now. However, we managed to create quite a new group with the addition of Cristian Mendes, Rossella Sesia, Carlo Trentalange and Alberto Giubilini who seem to be up to the task of keeping the traditions alive.

To my now historic *Material Guys* group. Andrea Cosola, Camilla Noè, Matteo Caprioli, Lorenzo Vigna, Jacopo Barberi, Marina D'Aloiso and Marco Franzoso. We've know each other for almost ten years, studied and worked together, had lunch together almost every day for the majority of this time with some of you. The fact we still talk to each other and like each other is a testament of itself of our friendship, as will be the fact that we'll keep doing it even when physically apart.

Moving away from the academic world, let's dive into the *fun side of the force* and my *athletic* support group. When I started my PhD I also started practicing *light saber combat* and I don't think I could have chosen a better sport or better friends. I met people with the most diverse backgrounds and interests, but who soon became a second family to me and supported me more times than I can remember. As a token of this wonderful world, I would like to thank all of the *hares* from the *Sisma* clan, with past and present instructors and members: Prema *Morgana* Bickel, Giulia *Lepre* Palladino, Roberta *Rigida* Garagliano, Marilena *Larida* Verdi, Claudio *Pahton* Colombatto, Giorgio *Oiser* Ferraresi, Marco *Raynard* Palena (the hare king), Marco *Taras* Conserva (the hare master). A particular shout out to my *jedi knight*, Daniele *Daky* Panizza, and our *godmothers* Paola *LadyFlame* Bovero and Jessica *Raksha* Caruso who made me exit my comfort zone and discover the world of refereeing which opened a lot of doors both mental and physical.

To my best friends, Ginevra Giobbio and Alessia Decastelli, who are always there when needed (even if physically some hours away) and who had to endure several rants from both my darkest and most exciting moments. You helped me plot more interesting and incredible revenges than I could ever exact and were the first

people I went to with both good and bad news. I wouldn’t be here without the two of you.

And finally to my family, who more often than not did not entirely understand when and why I was excited or angry, or just worried, but always cheered me on and supported me as best as they could. Be it with a hug, be it plotting revenge or baking a cake to celebrate, thank you for everything.

Abstract

Lithium and sustainability are probably two of the most used words in today's economy, governance and research world, often combined with the terms *green process* and *renewable energies*. Lithium is indeed widely used in light of its many interesting properties in a variety of sectors, among which batteries are at the forefront. Although the market for this element constantly increases as does its use in hybrid vehicles, smart grids, portable and precision electronics, sadly its availability does not. Therefore, new unconventional resources have been researched and studied considering the fact that the processes currently employed to commercially extract it by evaporation from salt lake brines are both water and time consuming and ores are gradually degrading. More environmentally friendly alternatives to these processes have also been investigated in an attempt to reduce the footprints of this industry. Furthermore, as one of the critical raw materials recognized by the United Nations, a responsible and sustainable supply of lithium becomes part of the 12th Sustainable Development Goal (chapter 1).

Several attempts at recovering lithium from aqueous solutions have been conducted in the past years, focusing either on concentrated brines, geothermal water, and even seawater. After an introduction on the role of lithium availability, the state of the art of these different technologies is presented in chapter 2. Those processes can be divided into two main families, namely adsorption and electrochemical processes. However, although the many endeavors, only a few pilot plants can be now found commercially extracting lithium from aqueous resources.

In this work, two different sustainable approaches to recover lithium are proposed after a brief excursus on the experimental methods (chapter 3). The first one belongs to the passive adsorption family and comprises a functionalized graphene oxide membrane working in a pressure-assisted filtration setup (chapter 4). The selectivity of crown ethers was here used in combination with the properties of the highly stacked graphene oxide membrane prepared under vacuum. This

system proved to work well with fairly diluted streams and achieved an impressive recovery of 70% of lithium from a 1 mM solution.

The second system was instead used in an electrochemical setup and was composed of anodically grown TiO_2 nanotubes hydrothermally converted into $LiTiO_x$ (chapter 5). After optimizing the synthesis and hydrothermal treatment, the electrodes showed impressive stability and reversibility in morphology and composition when intercalating lithium into the structure. Indeed, up to 17 at.% lithium was stored into the nanotubes in two different compounds. Furthermore, a static acidic de-lithiation treatment was also investigated, after which the samples were able to recover their storage ability. Preliminary tests for their use in aqueous environments were also conducted, with promising results in terms of selectivity.

Contents

List of Figures……..XI

List of Tables……XVI

List of Acronyms…….....XVII

Introduction.....1

1.1 Thesis outline.....1

1.2 Sustainability and lithium.....2

1.3 The role of lithium in today's economy.....2

1.4 Lithium availability.....5

State of the Art.....9

2.1 Overview.....9

2.2 Passive processes.....10

2.2.1 Evaporation.....10

2.2.2 Ion Sieves.....11

2.2.3 Membrane techniques and supramolecular systems.....14

2.2.4 Focus on graphene oxide membranes.....15

2.3 Active processes.....17

2.3.1 Ion pumping.....17

2.3.2 CDI.....19

2.3.3 ED.....20

2.3.4 Focus on titanium dioxide nanotubes.....21

Experimental 25
3.1 Graphene oxide membranes 26
3.1.1 Synthesis 26
3.1.2 Filtration protocol 27
3.2 Lithiated titania nanotubes 28
3.2.1 Anodic oxidation 28
3.2.2 Hydrothermal conversion 28
3.2.3 Preparation of the carbon counter electrodes 29
3.2.4 Cell assemblage and testing 29
3.3 Physico-chemical analyses 31
3.3.1 Scanning Electron Microscopy 31
3.3.2 X-Ray Diffraction 32
3.3.3 Raman spectroscopy 33
3.3.4 Infrared spectroscopy 34
3.3.5 Z-Potential 35
3.3.6 Thermogravimetric analyses 36
3.3.7 Conductivity measurements 36
3.3.8 ICP mass spectrometry 36
3.3.9 XPS 37
3.4 Electrochemical analyses 37
3.4.1 Voltammetry techniques 39
3.4.2 EIS 43
3.4.3. Other electrochemical analyses 46
Functionalized Graphene Oxide Membranes 49
4.1. Membrane preparation 49
4.2 Characterizations 51
4.3 Filtrations 55
Lithiated Titania Nanotubes 61

5.1 Optimization of hydrothermal conversion parameters 61
5.2 Electrochemical characterizations in organic electrolyte 66
5.3 Electrochemical characterizations in aqueous solutions.....78
5.3.1 De-lithiation mechanism 78
5.3.2 Selectivity in LiCl, NaCl, Li/NaCl.....82
Conclusions.....89
6.1 Future developments.....90
References.....93

List of Figures

Figure 1.1. Global end-use market of lithium, according to the U.S. Geological Survey from 2013 to 2022.16,21,22 3

Figure 1.2. Publication trend on lithium recovery papers, from 2000 to 2021. Research done on Scholar with the terms "lithium" and "recovery" in journals relating to Chemical, Engineering and Materials Sciences. (uptaded on 15/02/2022) 4

Figure 2.1. Schematic overview of the classification of lithium adsorption processes. Reproduced under the CC-BY Agreement.[64] Copyright 2022, The Authors, published by Wiley-VCH. 10

Figure 2.2. Schematic representation of the evaporitic technique. Adapted with permission.[11] Copyright 2018, Elsevier. 11

Figure 2.3. Isothermal cross-section of the Li-Mn-O ternary phase diagram. Adapted with permission.[56] Copyright 2016, Elsevier. 12

Figure 2.4. Li-selective crown ethers: (a) 12-crown-4, (b) 14-crown-4, (c) dibenzo- 14-crown-4, (d) didecalino- 14-crown-4, (e) decalino-14-crown-4. Reproduced with permission.[130] Copyright 2017, Elsevier. 14

Figure 2.5 (a) Functionalization of the PVDF+GO membrane with a pDA layer. Reproduced with permission.[134] Copyright 2018, Centre National de la Recherche Scientifique (CNRS) and the Royal Society of Chemistry; (b) functionalization of GO flakes with 12C4E. Reproduced with permission.[135] 16

Figure 2.6. Crystallographic structure of (a) rutile, (b) anatase, (c) brookite and (d) TiO2-B. Titanium atoms are red, oxygen light blue whereas the coordination octahedron is highlighted in green, Adapted with permission.[218] Copyright 2009, Elsevier. 21

Figure 2.7. Schematic of the electrochemical anodic oxidation process with the possible resulting morphologies: (I) electropolishing of the metal, (II) formation of a compact oxide layer, (III) self-ordered nanopores or nanotubes, (IV) disordered nanotubes, (V) ordered nanoporous layer. Adapted with permission.[220] Copyright 2011, Wiley. 23

Figure 3.1. (a) Vacuum and (b) dead-end filtration apparatuses employed in the production and use of the GO-based membranes. 27

Figure 3.2. Cell configuration for the EC analyses in organic electrolyte. From the bottom the NTs grown on top of Ti foil constitute 30

the WE, which is in contact with the separator soaked with the organic electrolyte on top of which is the thick active carbon-based counter electrode.
Figure 3.3. Cell configuration for the de-lithiation process. In this case two symmetric NTs electrodes were used as both WE and CE, separated by the acidic solution and a glass fiber separator. 30
Figure 3.4. Cell configuration for the aqueous EC analyses. In this case the WE is made of the NTs grown on the Ti foil, and the CE is the thick active carbon-based counter electrode. Those were separated by the glass fiber separator soaked in aqueous electrolyte. 31
Figure 3.5. Geometric representation of Bragg's law. 32
Figure 3.6. Raman spectra of graphene-based materials: from top to bottom graphite, 3-layers graphene, single layer graphene, disordered graphene, graphene oxide and nano graphene. Reproduced with permission.[311] Copyright 2018, the Royal Society of Chemistry. 34
Figure 3.7. (a) Helmholtz, (b) Gouy-Chapman, and (c) Stern models of the electrical double layer. Adapted from [313]. Copyright 2010, Oxford University Press. 38
Figure 3.8. (a) Potential-time profile applied and current-voltage profile measured in a typical CV experiment on TiO2 electrodes with a scan rate of 0.59 mV s-1. 39
Figure 3.9. Example of a Nyquist plot of a DSSC with a TiO2 photoanode. The mathematical fitting performed on these data is drawn with a dotted blue line. 44
Figure 3.10. Possible circuital representation of the Nyquist plot of a DSSC with a TiO2 photoanode. 44
Figure 3.11. Bode plot of a DSSC with a TiO2 photoanode. 45
Figure 4.1. Pictures of the 10 mg membranes prepared. (a) f-GO, (b) f-GO + GO, (c) f-GO+PVDF, (d) f-GO+PVA. Adapted under the CC-BY license.[164] Copyright 2022, The Authors, published by MDPI. 50
Figure 4.2. (a) Wet membrane and (b) dried membrane after continuing operations for several months. 51
Figure 4.3. SEM micrographs of (a) GO, (b) f-GO, (c) f-GO+PVA membrane and (d) top view of the f-GO+PVA membrane after the filtrations. Adapted under the CC-BY license.[164] Copyright 2022, The Authors, published by MDPI. 52
Figure 4.4. (a) XRD diffractograms and (b) Z-potential of GO (in red), f-GO (in black) and f-GO+PVA (in blue) membranes. Adapted under 52

the CC-BY license.[164] Copyright 2022, The Authors, published by MDPI.

Figure 4.3. (a) Raman spectra, (b) FTIR spectra and (c) TGA and DTG curves of pure GO (in red), f-GO (in black) and f-GO+PVA (in blue) membranes. Adapted under the CC-BY license.[164] Copyright 2022, The Authors, published by MDPI. 54

Figure 4.4. Permeability curves of GO (in red) and f-GO+PVA (in blue) membranes. Adapted under the CC-BY license.[164] Copyright 2022, The Authors, published by MDPI. 55

Figure 4.5. (a) Conductivity measurements (of the salt solutions) and (b) lithium and sodium recovery rates from ICP mass analyses (of the stripping solutions). 57

Figure 4.6. Comparison of the experimental data with other literature works, in terms of uptake as a function of (a) feed solution and (b) adsorption time. The experimental data of the lithium adsorption from the f-GO+PVA membrane are represented with blue stars. 59

Figure 5.1. SEM micrographs of TiO2 anatase nanotubes. (a) cross-section of the NTs, (b) inset of the top view, (c) inset of the bottom view. Adapted under the CC-BY license.[308] Copyright 2022, The Authors, published by Wiley-VCH. 62

Figure 5.2. (a) XRD diffractograms of the anatase samples treated at 120 °C for 2 hours at different LiOH concentrations; (b) SEM micrograph of a sample unsuccessfully converted into LiTiOx. Adapted under the CC-BY license. [308] Copyright 2022, The Authors, published by Wiley-VCH. 63

Figure 5.3. (a) XRD diffractograms of the anatase samples treated at 150 °C for 2 hours at different LiOH concentrations; (b) SEM micrograph of a sample crystallographically converted into LiTiOx but where the morphology was not conserved. Adapted under the CC-BY license.[308] Copyright 2022, The Authors, published by Wiley-VCH. 64

Figure 5.4. (a) XRD diffractograms of the anatase samples treated at 200 °C for 2 hours at different LiOH concentrations; (b) SEM micrographs of a sample successfully converted into LiTiOx with (c) inset of the tubular morphology. Adapted under the CC-BY license.[308] Copyright 2022, The Authors, published by Wiley-VCH. 64

Figure 5.5. XRD diffractograms of the anatase and amorphous samples treated at different temperatures for 2 hours in 0.25 M LiOH, with schematic representations of successful (bottom) and unsuccessful 65

(top) conversions. Adapted under the CC-BY license.[308] Copyright 2022, The Authors, published by Wiley-VCH.
Figure 5.6. (a) Cyclic voltammograms of TiO2, LiTiOx and *deLi-TiOx* electrodes in organic electrolyte and (b) Coulombic efficiencies of the scans at 0.2 mV s-1. 67
Figure 5.7. Cathodic peak current densities as a function of the square root of the applied scan rates in the electrochemical reversibility range. All linear fittings present a value of R2>0.9985. 68
Figure 5.8. *b-value* graphs of the cathodic peak currents of the three electrodes analyzed. 69
Figure 5.9. Deconvolution of the current into diffusive and capacitive components by applying the Dunn method on the 0.59 mV s-1 voltammograms in the (a) 0.2 mV s-1 to 0.8 mV s-1 and (b) 0.59 mV s-1 to 1.4 mV s-1 ranges. 70
Figure 5.10. Tafel plot of the lithiated electrodes with 50% of the current integrated at 100 μV s-1. 71
Figure 5.11. Tafel plots of the lithiated electrodes performed at (a) different scan rates with 50% off current integrated and (b) different % of integrated current at 100 μV s-1. 72
Figure 5.12. Normalized cyclic voltammetries of TiO2, LiTiOx and *deLi-TiOx* electrodes with scan rates spanning from 0.2 mV s-1 to 200 mV s-1. 73
Figure 5.13. Mott-Schottky plots of TiO2, LiTiOx and *deLi-TiOx* electrodes at 10 Hz. The potential window was restricted to focus on the region near the intercept of the linear fitting. 74
Figure 5.14. XRD patterns of the TiO2 and lithiated samples before and after the EC characterizations. Stars indicate the anatase phase, circles the lithium-poor phase, reversed triangles the lithium-rich phase, and rhombuses the titanium foil underneath**.** 75
Figure 5.15. SEM micrography of the LiTiOx nanotubes after the EC characterizations. Adapted under the CC-BY license.[308] Copyright 2022, The Authors, published by Wiley-VCH. 76
Figure 5.16. Survey XPS acquisition of (a) LiTiOx NTs after the hydrothermal conversion and (b) LiTiOx samples after the EC characterization. 77
Figure 5.17. HR XPS aquisition of the Li 1s region of (a) LiTiOx NTs after the hydrothermal conversion and (b) LiTiOx samples after the EC 77

characterization. Adapted under the CC-BY license.[308] Copyright 2022, The Authors, published by Wiley-VCH.
Figure 5.18. HR XPS aquisition of the Ti 2p region of (a) LiTiOx NTs after the hydrothermal conversion and (b) LiTiOx samples after the EC characterization. Adapted under the CC-BY license.[308] Copyright 2022, The Authors, published by Wiley-VCH. 78
Figure 5.19. XRD patterns of the lithiated and de-lithiated samples before and after the EC characterizations, with schematic representations of the morphologies of lithium-rich and lithium-poor structures. Circles index the lithium-poor mixed oxide, reversed triangles the lithium-rich mixed oxide, and rhombuses the titanium foil underneath. Adapted under the CC-BY license.[308] Copyright 2022, The Authors, published by Wiley-VCH. 79
Figure 5.20. SEM micrograph of the delithiated samples. 81
Figure 5.21. Survey XPS acquisition of *deLi-TiOx* NTs (a) before and (b) after the EC characterizations. 80
Figure 5.22. HR XPS aquisition of the Li 1s region of *deLi-TiOx* NTs (a) before and (b) after the EC characterizations. Adapted under the CC-BY license.[308] Copyright 2022, The Authors, published by Wiley-VCH. 81
Figure 5.23. Polarization of the carbon-based counter electrode during the cycling of the working electrode of lithiated nanotubes over a 3V potential window. 82
Figure 5.24. Nyquist plot of the (a) lithiated nanotube electrode and (b) carbon-based counter electrode, (c) equivalent circuit of the cell. 83
Figure 5.25. (a) two-electrodes and (b) three-electrode cyclic voltammetries profiles of LiTiOx samples in LiCl 100 mM. 83
Figure 5.26. Cyclic voltammetries of (a) LiTiOx and (b) TiO2 anatase samples in LiCl at different concentrations. 84
Figure 5.27. (a) Cyclic voltammetries and (b) EIS profiles of LiTiOx samples in LiCl (blue), NaCl (green) and LiCl/NaCl 100 mM (purple). 85
Figure 5.28. XRD patterns of LiTiOx in LiCl (in blue), NaCl (in green) and mixed cation solution (in purple) at half cycle. The reference sample of LiTiOx is shown in black. 86
Figure 5.29. XRD patterns of LiTiOx in LiCl (in blue), NaCl (in green) and mixed cation solution (in purple) at full cycle. The reference sample of LiTiOx is shown in black. 86

List of Tables

Table 1.1. Worldwide distribution of lithium resources, according to the 2022 USGS Mineral Commodities Summary. Only the countries with more than 1 Mt are reported.[22] 6
Table 2.1. Comparison between the different forming technologies 13
Table 4.1 Characteristic values obtained from the thermos-gravimetrical analyses performed on the three membranes. 54
Table 5.1. Summary of the outcomes of the different conversion parameters combinations 66
Table 5.2. Summary of the electrochemical properties of the TiO2-based electrodes in organic electrolyte at 0.2 mV s-1. 74
Table 5.3. Compositional analyses of the samples tested in Li/NaCl, NaCl and LiCl at half cycle conditions. 88

List of Acronyms

Acronym	Meaning
(FE)SEM	(Field Emission) Scanning Electron Microscopy
2M12C4E	2-Hydroxymethyl-12-crown-4
AC	Alternated current
ATR	Attenuated Total Reflection
CaCl2	Calcium Chloride
CDI	Capacitive Deionization
CE	Counter Electrode
CV	Cyclic Voltammetry
DCC	Dicyclohexylcarbodiimide
***de*Li-TiO$_x$**	de-lithiated LiTiO$_x$
DIW	Deionized Water
DMAP	4-(Dimethylamino)pyridine
DMSO	Dimethyl sulfoxide
DSSC	Dye-sensitized Solar Cell
DTG	Derivative ThermoGravimetric Analysis
EC	ElectroChemical
ED	Electrodialysis
EDL	Electrical Double Layer
EDS	Energy-Dispersive Spectroscopy
EG	Ethylene Glycol
EIS	Electrochemical Impedance Spectroscopy
f-GO	functionalized Graphene Oxide
GO	Graphene Oxide

HCl	Hydrochloric Acid
HF	Hydrofluoric Acid
HR	High Resolution
ICP-MS	Inductively Coupled Plasma Mass Spectrometry
IR	InfraRed
KCl	Potassium Chloride
LFP	Lithium Phospho-Olivine
LIBs	Lithium-Ion Batteries
LICs	Lithium-Ion Capacitors
LiCl	Lithium Chloride
LiOH	Lithium Hydroxide
LIS	Lithium Ion Sieve
LiTiOx	Lithium Titanium Mixed Oxide
LMO	Lithium Manganese Oxide
LMTO	Lithium Manganese Titanium Oxide
LTO	Lithium Titanium Oxide
LSV	Linear Sweep Voltammetries
MgCl2	Magnesium Chloride
Mt	Megatons
NaCl	Sodium Chloride
NTs	Nanotubes
OCP	Open Circuit potential
OHP	Outer Helmholtz Plane
pDA	Polydopamine
PTFE	Polytetrafluoroethylene
PVA	Poly(vinyl alcohol)
PVDF	Poly(vinylidene fluoride)
REF	Reference electrode
SEI	Solid Electrolyte Interface

SDGs	Sustainable Development Goals
TGA	ThermoGravimetrical Analyses
USGS	United States Geological Survey
WDS	Wavelength-Dispersive Spectroscopy
WE	Working Electrode
XPS	X-Ray Photoelectron Spectroscopy
XRD	X-Ray Diffraction

Chapter 1

Introduction

1.1 Thesis outline

The work reported in this thesis deals with two different sustainable methods of recovering lithium from water resources. The structure of the work herein reported is as follows. A first introductory chapter is focused on sustainability, lithium, and why lithium harvesting from aqueous solutions could be part of the solution to a possible shortage of this critical element in today's economy.

After that, Chapter 2 presents the state of the art on this topic, introducing the difference between adsorption (passive) and electrochemical (active) processes. This distinction will be the foundation of the two different approaches explored in the experimental part related in chapter 3. Chapter 3 will also feature a small overview of the theoretical background and experimental setups of the characterization techniques employed throughout the analyses.

Chapter 4 will then focus on the results obtained through the use of crown ether functionalized graphene oxide membranes in a pressure assisted dead-end filtration setup. Chapter 5, instead, will be devoted to the lithiation of titanium dioxide nanotubes and their application in an electrochemical setup. A comparison between the two different methods and their possible applications to larger setups in finally reported in Chapter 6, dedicated to the conclusions of this work.

1.2 Sustainability and lithium

Sustainability is an ever present and often abused word in todays' politics, economy and regulations. *Green* approaches and environmental management systems are strongly encouraged to limit the environmental impact of mankind in almost all sectors and incentives are often offered to those who undertake this path in the industrial world.[1] In 2015, the United Nations adopted the *2030 Agenda for Sustainable Development* which contained the definition of the 17 Sustainable Development Goals (SDGs). Those act as thematic guidelines at every level of management and range from energy and water to poverty and education and inequalities.[2]

Lithium is nowadays almost as popular as all the possible declinations of the *sustainability* concept. As will be properly shown in the next section, the capillary use of lithium ion batteries (LIBs) is so widespread that both the European Commission in 2020 and the U.S. Geological Survey in 2022 classified lithium as one of the *critical raw materials*.[3,4] The following materials were defined as such: antimony, baryte, bauxite, beryllium, bismuth, borate, cobalt, coking coal, fluorspar, gallium, germanium, hafnium, heavy rare earth elements, indium, light rare earth elements, lithium, magnesium, natural graphite, natural rubber, Niobium, platinum group metals, phosphate rock, phosphorus, scandium, silicon metal, strontium, tantalum, titanium and tungsten. This list, first created in 2011, contains all the elements and materials of high importance to the economy whose supply is considered at high risk. They pertain, but are not limited to, the energy industry and clean technologies and are irreplaceable in modern technologies. As one can see most of the materials presented in this list are used to produce batteries and circuitry boards. With the recent addition of lithium in this list, its production and use as raw material has now become one of the topics of the SDG 12, *Responsible Consumption and Production*.[5] A sustainable way of extracting this element is therefore of critical importance, and new ways and resources have to be explored.

1.3 The role of lithium in today's economy

In the past decades, lithium has become one of the most used and sought-after materials in the energy production sector. Its many interesting properties, such as low density (0.534 g cm^{-3}), high specific heat capacity and low electrode potential in the electrochemical scale (-3.045 V) have made it the leader in the field of both

single-discharge (primary) and rechargeable (secondary) batteries.[6–8] These batteries, in turn, have a wide range of applications in light of their specific power, energy density and lifetime characteristics (250-340 W kg^{-1}, 100-265 Wh kg^{-1}, and 400 to 1200 cycles). They can be found not only in precision electronics and portable electronic devices, but also in electric and hybrid vehicles and are even employed in energy storage smart grids.[7,9–13] All of this contributes to a rise in the market size of lithium-ion batteries which is said to increase from USD 41.1 billion in 2021 to 116.6 billion by 2030.[14]

While the battery world is the primary use of lithium, representing nowadays 74% of its world market share and 37% of the world market of batteries, several other fields benefit from its many important features.[8,15,16] From a historical point of view, lithium was first used as process additive in the ceramics and glass production. It can, in fact, not only lower both their viscosity and melting point, but also their thermal expansion coefficient and increase their hardness. Other uses include lubricant and greases for high performances sectors, the aluminum electrolytic refinery process, cooling systems, and the cure of bipolar disorders. Furthermore, lithium isotopes can also be used as fuel in nuclear energy reactors.[6–8,15–21] An overview of its uses and their evolution in the last ten years, as reported by The United States Geological Surveys (USGS), is reported in Figure 1.1.

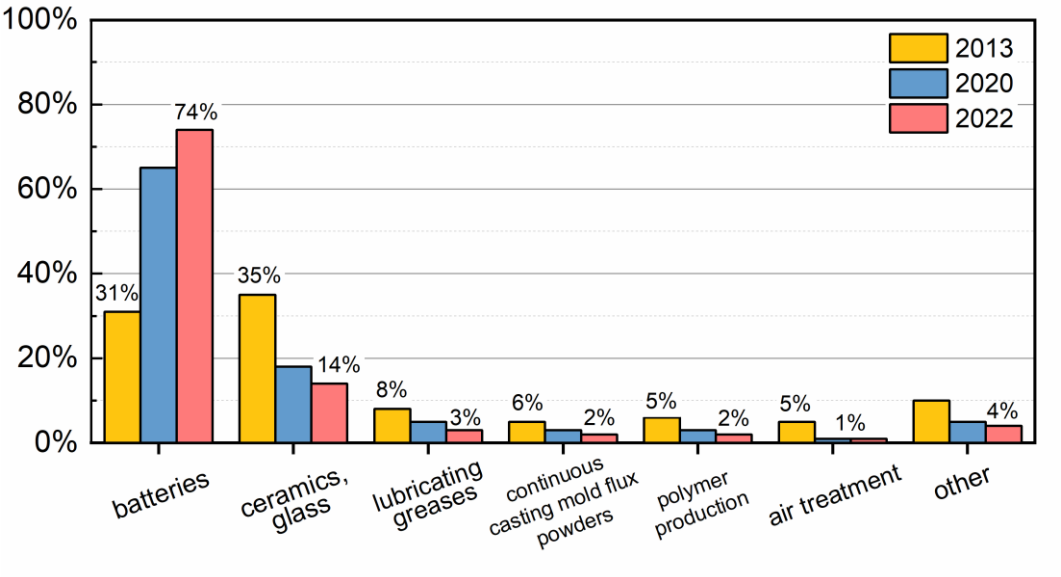


Figure 1.1. Global end-use market of lithium, according to the U.S. Geological Survey from 2013 to 2022.[16,21,22]

Together with its use, the price of lithium also underwent some substantial escalation in the last years. The USGS Mineral Commodities reports that together with the reprise of common operations after the pandemic, the annual average price for battery-grade lithium carbonate (Li_2CO_3) doubled in the past two years, going from 8,000 dollars per metric ton[2] in 2020 to 17,000 dollars per metric ton[2] in 2021, reaching similar values to the highest reported in the past years.[16,22] These high costs are partially due to the complexity of the extraction processes, often time, energy and water consuming, which require several preprocessing steps and the strategical locations of its deposits.

This *race for lithium* is also reflected in the number of publications pertaining to lithium recovery, one of the hot topics due to its limited availability. The result of a simple search on Scopus for publications with the key terms "lithium" and "recovery" in journals relating to Chemical, Engineering and Materials Science in the last twenty years is reported in Figure 1.2. It is possible to see that the interest in this topic increased in an exponential way in the last decades, coherently with the demand of this critical element.

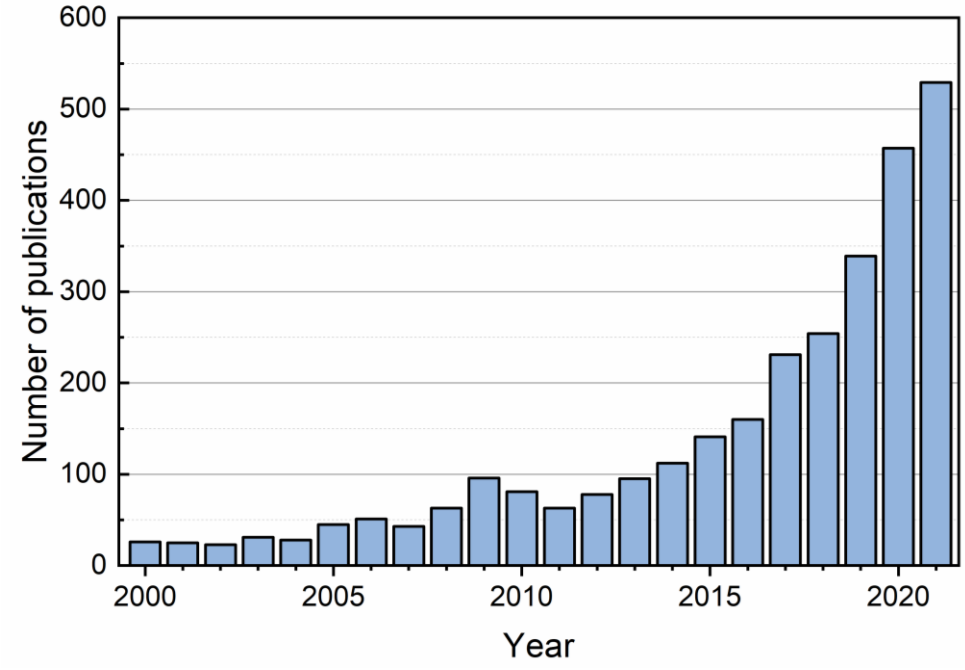


Figure 1.2. Publication trend on lithium recovery papers, from 2000 to 2021. Research done on Scholar with the terms "lithium" and "recovery" in journals relating to Chemical, Engineering and Materials Sciences. (uptaded on 15/02/2022)

1.4 Lithium availability

Due to its high reactivity, lithium cannot be naturally encountered in its elemental form, and is generally found in minerals or water basins. In the following, in accordance with the USGS Reports, both the denomination of lithium reserves and resources to account for its availability will be used. Although these two terms are often used as synonyms, they have indeed different meanings. While in the academic world the term resource is more common as it is the geological available amount, the term reserve is often found more suitable in technical reports as it takes into account the technological and socio-economical extraction feasibility criteria.[11,16,18,20,23,24]

Lithium deposits can be divided in two different categories:[6,8] primary resources comprehend minerals, seawater and brines, i.e. natural deposits of lithium, whereas secondary ones comprise artificial sources like spent batteries and wastewaters.[23,25–27] Despite being present in 145 different minerals, lithium can only be obtained from five of them. Of these, four are lithium aluminosilicate, i.e. spodumene, lepidolite, petalite and eucryptite, while amblygonite is an aluminum phosphate.[26] These minerals can generally be found in pegmatite districts. The most common one is spodumene, but their destination can determine the most suitable mineral for that use, in light of impurities that lithium carbonate can retain after the extraction. For example, petalite is most commonly used in glass production for its iron content, while lepidolite has been recently disregarded due to its fluorine contents.[9,10,24,26] The extraction of lithium from secondary products like spent batteries is becoming more and more relevant not only to limit the raw material extraction but also to manage more properly the recycling process of these products. Indeed, while metals like cobalt and nickel are normally recovered during the recycling of LIBs, lithium is oftentimes left in the final slag, when it is said that up to 90% of it could be retrieved from this kind of processes.[7,23,28,29]

The amount of lithium reserves and resources greatly differs in the literature as the methods of assessing it change overtime and the technological advancements make extraction from new sources possible. In the past ten years, the estimated amount of lithium available worldwide doubled, going from ca. 40 megatons (Mt) in 2011 according to several sources to the latest USGS which reported around 89 Mt.[9,11,18,22–24] An overview of the distribution of these deposits according to the 2022 USGS is reported in Table 1.1. When looking at these data it is evident how uneven the distribution of these resources is. Furthermore, Gruber reported in 2011 than more than 80% of these were contained in the top ten lithium deposits, which

accounted for six brines, two pegmatites and two sedimentary rocks deposits.[23] Similarly, the latest USGS reported that the majority of the world production resided in two brines in Argentina, the Australian mineral operations, two brines in Chile, and a brine and a mineral operation in China.[22] This further highlights the need for a sustainable governance of this element and environmentally sound policies, backed by lifecycle and sustainability assessments.[30–35]

Table 1.1. Worldwide distribution of lithium resources, according to the 2022 USGS Mineral Commodities Summary. Only the countries with more than 1 Mt are reported.[22]

Country	Total Reserves (Mt)	Mine Reserves (Mt)
Bolivia	21.0	--
Argentina	19.0	2.2
Chile	9.8	9.2
US	9.0	0.75
Australia	7.3	5.7
China	5.1	1.5
Congo	3.0	--
Canada	2.9	--
Germany	2.7	--
Mexico	1.7	--
Czechia	1.3	--
Serbia	1.2	--
Russia	1.0	--
Others	4.0	3.075

Despite the different accounts on the total amount of lithium deposits, most studies agree that two thirds of lithium globally available resides in water resources.[8,21,23] The extraction from this kind of deposits, although in theory less

rich than the mineral ones, often result less energy consuming.[36,37] The term *water resource* covers seawater, geothermal water and brines. Going from lower to higher lithium concentrations, seawater has an average of 0.17 ppm of lithium, it being the most abundant metal ion after sodium, magnesium, calcium and potassium, which are already commercially extracted. Despite this apparently low concentration, both Bardi and Can Sener estimated that its commercial extraction could be economically possible.[36,38] Furthermore, the purity grade of the mineral would not decrease during the extraction processes in light of the vast availability of this source and the energetic requirements could be partially met by coupling this extraction with desalination plants and/or renewable resources.[37]

Although with higher concentrations, geothermal brines present several other limitations, like high temperatures and pressures of the reinjection branch, which can be as high as 80-100°C and 20 bars. Several studies have been undertaken to assess the feasibility of the extraction from this source,[33,39–45] but to the best of the author's knowledge only one plant in Europe is now successfully working.[46,47]

Finally, salars brines, commonly referred to as brines, are water solutions with a higher salinity than seawater, generally higher than 50 g L^{-1}. Lithium extraction from salar by evaporation has been in use since 1938 and is nowadays considered to cover close to two thirds of commercially available lithium.[10,11,21] These salar brines are mostly concentrated in the so-called *Puna Plateau*, or *Lithium triangle*, a high altitude Andean region in South America, which accounts for almost 80% of the world brine resources. This area and the Qinghai-Tibet plateau, the second area for high salinity lakes, share the same geological characteristics: arid climates, high altitude and geothermal/igneous activity, which are fundamental for the successful exploitation of the evaporitic technique.[11,48] As will be further explained in Chapter 2, the evaporitic technique is indeed the technique most used in commercial extraction from salars.

Chapter 2

State of the Art

This chapter will address the state of the art of the different technologies available to recover lithium from water resources. After an introduction on the different processes available and the ones that are already industrialized, a different section will be devoted to each of the two main families, i.e. passive processes and active processes. While presenting the passive processes, a specific subsection on graphene oxide membranes will give more details on the technology herein chosen. The same will be done for titania nanotubes in the section on active (electrochemical) processes.

2.1 Overview

There are many possible ways to classify the different methods with which one can recover lithium from water resources. A first classification could be based on the source of lithium, i.e. spent batteries,[49] geothermal water,[41] salt lake brines.[19,50] seawater desalination brine.[51] However, even though some techniques and issues can be specific to some feed solutions, this classification can result sectorial. Other authors preferred to divide the processes based on the main feature of the process employed or the driving mechanism, whether it be membrane processes,[52] battery approaches,[53,54] ion sieving techniques,[55–57] precipitation,[58] or electrodialysis.[59] A further classification often involves the kind of the active material/electrode adopted.[57,60–62]

In this work, we employ a classification based on the driving force behind lithium adsorption, followed by the kind of process and the material used, as was

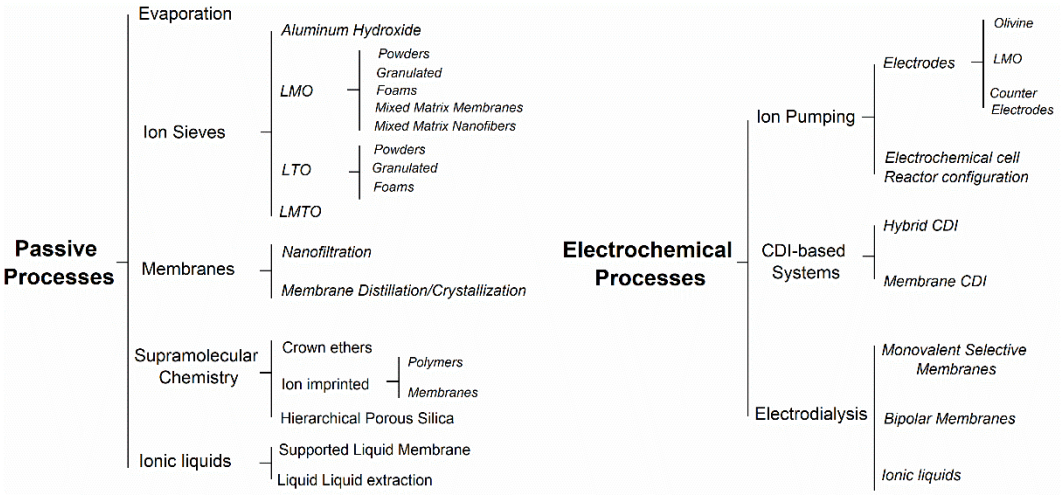


Figure 2.1. Schematic overview of the classification of lithium adsorption processes. Reproduced under the CC-BY Agreement.[64] Copyright 2022, The Authors, published by Wiley-VCH.

previously done in other works.[63,64] This results in a primary distinction between passive processes, based on physical adsorption, and electrochemical techniques in which an electrical field is applied, and a further one based on the technique or driving mechanism employed.[65–67] In particular, the use of the term *passive processes*, was taken from LiVecchi et al. who used it to define processes in which no external electrical field was applied in blue energy and seawater mining applications.[63] An overview of this classification can be seen in Figure 2.1.

2.2 Passive processes

In the classification here adopted, passive processes comprehend evaporation, ion sieves techniques, membranes, supramolecular systems and ionic liquids. Among these, to the best of the author's knowledge the only technique that is currently being used for large scale commercial purposes is evaporation, which nowadays accounts for a considerable share of lithium worldwide production.

2.2.1 Evaporation

According to the study conducted by Flexer et al. eight facilities were active in 2018: two in Argentina (on the Salar de Hombre Muerto and de Olaroz), two in Chile (at the Salar de Atacama), one in the USA (Clayton Valley) and three at a pilot stage in China (Chaerhan Salt Lake, West Taijinar and Zabuye).[11] These data

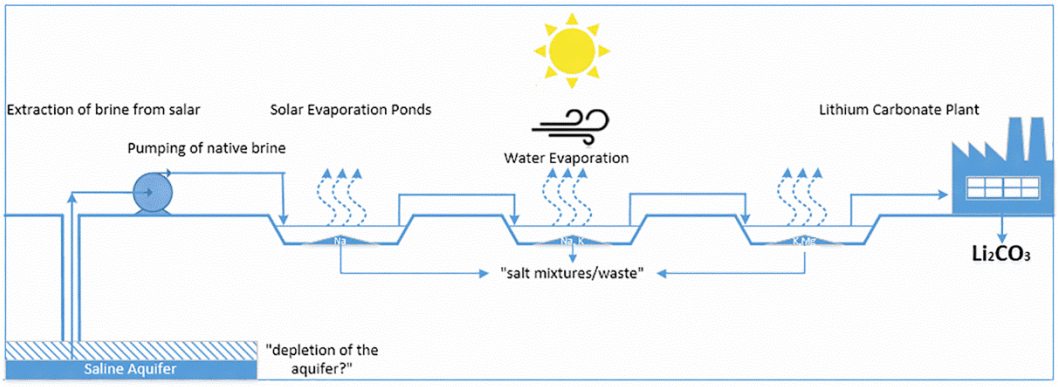


Figure 2.2. Schematic representation of the evaporitic technique. Adapted with permission.[11] Copyright 2018, Elsevier.

are in general agreement with the latest USGS 2022 Report which accounts for six brine operations outside of the US and one in Nevada.[22] The evaporitic technique takes advantage of the climatic conditions in which these salt lake are found, which consist in arid and windy climates combined with the presence of one or more aquifers and closed basins.[11,21,48] After a first stage in which the brine is pumped from the aquifer, it undergoes a concentration process up to 6 g_{Li} L^{-1} in wind and solar evaporation ponds. The brine is then pumped into a recovery plant in which lithium carbonate is obtained through successive precipitation steps, depending on the composition and pH of the brine. The lithium carbonates thus obtained can then be re-dissolved and re-precipitated to further purify it and thus obtain higher grades.[11,17] A schematic of this kind of operations is displayed in Figure 2.2.

Although this process exploits the arid and windy conditions peculiar to the basins zones, it can take up to twenty four months to complete and further stokes the aridification of those areas. Furthermore, even though the use of solar and wind evaporation can limit the operation cost, this kind of plant generally has a large footprint,[68] and specific measures have to be implemented in order to minimize the depletion of the aquifers.

2.2.2 Ion Sieves

Amidst all the other passive processes, adsorption by ion sieves might be the most promising technique with reference to quality of the final product and efficiency. Furthermore, ion sieves could be integrated in industrial setups and even used for less concentrated feed solutions. Ion sieves are inorganic compounds where

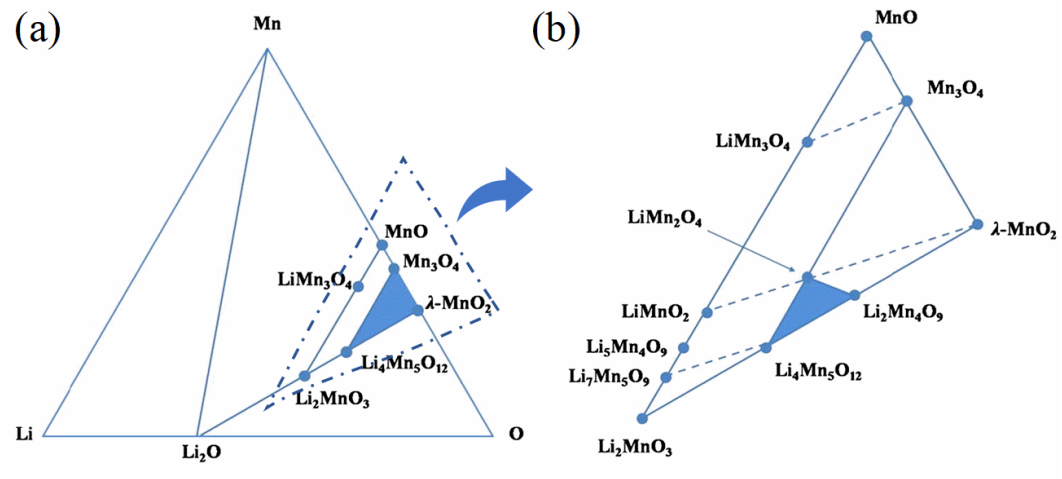


Figure 2.3. Isothermal cross-section of the Li-Mn-O ternary phase diagram. Adapted with permission.[56] Copyright 2016, Elsevier.

previously introduced template ions are eluted from the structure leaving ion-specific vacancies.[56,62] The first example of this class of materials dates back to 1971, when Volkhin studied the ion-exchange properties of mixed ferrocyanides.[69] In the case of Lithium Ion Sieves (LIS) three main families of compounds can be found, depending on their chemistry: aluminum hydroxides, lithium manganese oxides (LMO) and lithium titanium oxides (LTO). An intermediate version of the latter two, a mixed lithium manganese and titanium oxide (LMTO) can also be found in literature, as well as different attempts of doping canonic stoichiometries.[56,70–73]

The most common ion sieves are the LMO ones, because of the high variety of stoichiometries they can present which increase their versatility for both ion sieves and electrochemical applications. The Li-Mn-O ternary phase diagram is displayed in Figure 2.3 (a) in the isothermal cross-section at 25°C, with an inset of the defect spinel phase in Figure 2.3 (b). LMO-type LIS were first studied by Hunter in 1981,[74] who discovered the stability of the $LiMn_2O_4$ spinel structure after acidic elution. Other frequently employed precursors are $Li_{1.33}Mn_{1.67}O_4$ (or $Li_4Mn_5O_{12}$), and $Li_{1.6}Mn_{1.6}O_4$.[75,76]

LTO ion sieves, instead, have been used in primarily two structures: the layered titanate Li_2TiO_3 and the spinel $Li_4Ti_5O_{12}$.[76,77] The spinel has also been deeply investigated for battery applications together with the different polymorphs of titanium dioxide, i.e. rutile, anatase, brookite and TiO_2-B.

LIS technologies are supposedly less energy consuming and more environmentally friendly than other technologies,[56,62] however they also generally require longer adsorption times as they need to reach the thermodynamical equilibrium during the adsorption process and the usually require forming processes. All the different preparation methods, be them solid state or soft chemical processes, provide indeed LIS in the powder morphology. Although powder morphologies are usually used as reference for all the other morphologies because it shows the highest efficiencies, their handling can be difficult and energy consuming. Several forming technologies have been proposed to overcome these limitations, among which granulation, foaming and membrane preparation are the most common ones. All these forming techniques are characterized by the addition of a binder which will act as support for the adsorbents and will shape them into their final form. Although conventional polymers have been widely employed as binders, recently biopolymers have attracted a lot of attentions. Among those, the most commonly used for these applications are the chitin/chitosan couple, agar and cellulose, to reduce the processes environmental footprint while increasing their water permeability.[78–84] The main advantages and disadvantages of each morphology is displayed in Table 2.1.

Table 2.1. Comparison between the different forming technologies

Forming technique	Advantage	Disadvantage
Powders	Superior adsorption capacity	Difficult handling
Granulation	Good mechanical strength, can be used in industrial column operations	Lower adsorption capacity
Foaming	Superior mechanical properties, good regeneration, more adaptable (shape and recovery)	Lower adsorption capacity, internal structure can degenerate faster, expensive, hazardous substances,
Membrane	Modular and scalable	Complex, expensive

2.2.3 Membrane techniques and supramolecular systems

Membrane techniques have been deeply investigated in light of their modular design, and high separation efficiency which make them suitable candidates for industrial scale-ups. Their versatility make their use possible both in the form of nanofiltration membranes, as support for ion sieves, in mixed matrix membranes and even in membrane-assisted electrosorption processes.[52,85,86]

Although being historically used for desalination purposes before the last steps involving reverse osmosis or for the retention of pharmaceuticals and pollutants in water purification processes,[87–91] nanofiltration membranes have been recently introduced in raw material recovery applications.[92] Nanofiltration membranes exploit the combination of steric hindrance and the Donnan effect, meaning the inequal permeant ions distribution at an interface, to selectively exclude multivalent ions.[93] While these membrane show selectivity towards the ion valence, they do not recognize one monovalent ion from another and therefore require either a pre-processing or a post-processing to isolate the target ion.[92,94] Membranes can also be functionalized in order to display a positive superficial charge to increase their Li^+/Mg^{2+} separation ability.[95–102] This kind of membrane can also be used in combination with membrane distillation or crystallization reactors where a vapor pressure gradient across the membrane will induce the formation of a super-saturated solution or a crystalline specimen.[103–105]

In this dissertation, the term *supramolecular chemistry*, or *supramolecular systems*, will be used in relation to the chemistry of crown ether molecules. Ever since Steward's patent of 1957 and Pedersen's pioneering work from 1967, the coordination chemistry of crown ether has been widely investigated.[106,107] Indeed, Pedersen was the first to notice the cavity-cation size correlation that determined the selectivity of these molecules, and started a whole supramolecular chemistry branch. Crown-4 and crown-5 derivatives (see Figure 2.4) were found to be the best

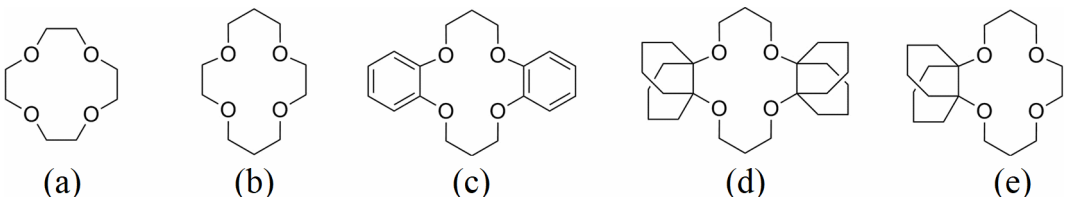


Figure 2.4. Li-selective crown ethers: (a) 12-crown-4, (b) 14-crown-4, (c) dibenzo- 14-crown-4, (d) didecalino- 14-crown-4, (e) decalino-14-crown-4. Reproduced with permission.[130] Copyright 2017, Elsevier.

suited to accommodate the smaller cations like lithium and sodium and several molecules were synthetized depending on their application fields, which ranged from extraction photometry to serum lithium assay, even with reports of dual crown ether functionalized structures to successfully recover different target ions.[108–117] Among the family of crown-4 derivatives, 12-crown-4-ethers have been proved to be particularly selective towards lithium,[114,118–124] and theoretical investigations were also conducted to support and better understand the selectivity of these molecules.[125–131]

Crown ether molecules can be grafted onto polymers, thus creating ion imprinted polymers or membranes, respectively.[113,114,119,122,132–135] Different polymers were investigated for this kind of applications, the main being Poly(vinylidene fluoride) (PVDF), polysulfone and natural polymers.[120,133–136]

2.2.4 Focus on graphene oxide membranes

Graphene oxide (GO) membranes have been extensively used in several different fields in light of their versatility, ease of functionalization and preparation.[84,137,146–150,138–145] Its possible use in targeting ions in water streams by tailoring its filtration properties through functionalization of its hydrophilic and oxygen-rich channels has already been demonstrated, both theoretically and experimentally.[151–154] Moreover, the use of preparation techniques like vacuum or pressure-assisted filtration can provide a highly stacked morphology with different degrees of order,[155] where the layered structure is responsible for the filtration properties.[140,141,156–160] Although its use is well-known for water treatment and oil-water separation,[137,139,141,147,148,161] its popularity in lithium recovery is still on the verge of rising. Indeed, its role has been generally relegated to additive to take advantage of its anti-fouling, mechanical properties and hydrophilicity.[119,133–135,162].

Two different routes can be taken when using GO as an additive in this kind of applications (see Figure 2.5). A first option, proposed by Sun et al. and Cui et al,[133,134] was to prepare a PVDF membrane by phase inversion and then use a polydopamine (pDA) adhesion layer to graft onto it the crown ethers (Figure 2.5 (a)). Otherwise, Sun et al.,[135] firstly functionalized GO with crown ether molecules (see Figure 2.5 (b)), then mixed them with the main material which in this case was PVDF and finally prepared the membrane by phase inversion. A similar method was employed by Zheng et al. who functionalized GO flakes and then mixed them with chitosan and Poly(vinyl alcohol) (PVA) before spinning the nanofiber which would constitute the membrane.[119]

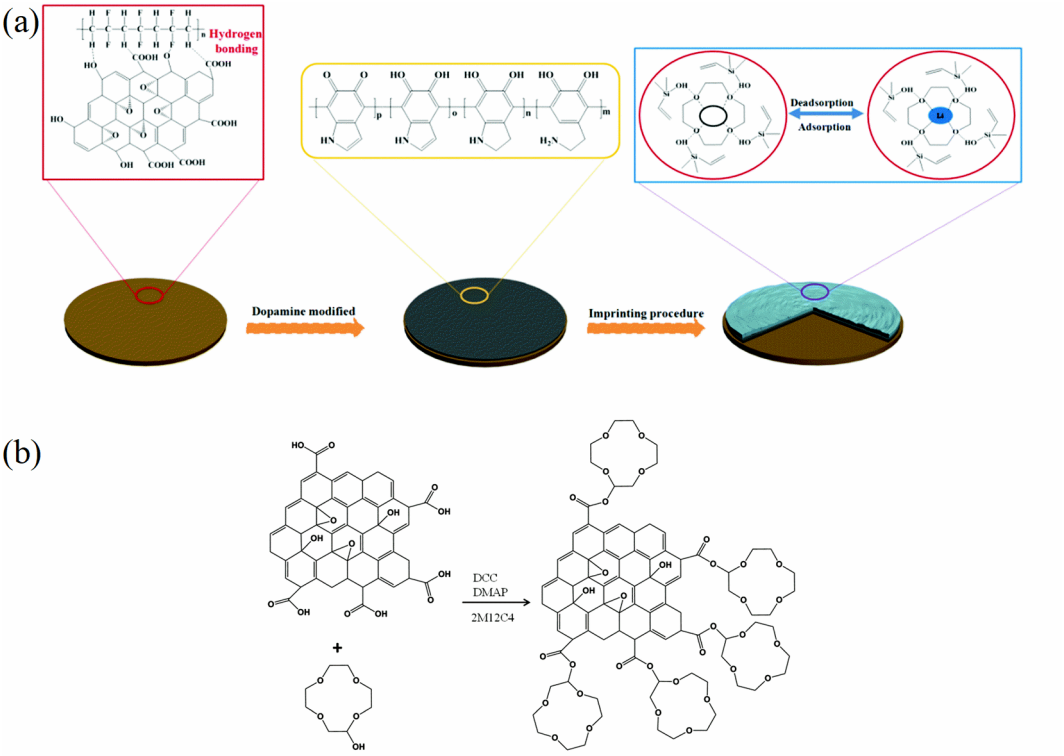


Figure 2.5 (a) Functionalization of the PVDF+GO membrane with a pDA layer. Reproduced with permission.[134] Copyright 2018, Centre National de la Recherche Scientifique (CNRS) and the Royal Society of Chemistry; (b) functionalization of GO flakes with 12C4E. Reproduced with permission.[135] Copyright 2018, Centre National de la Recherche Scientifique (CNRS) and the Royal Society of Chemistry.

In the approach proposed in Chapter 4, *Functionalized Graphene Oxide Membranes*, a crown ether functionalized graphene oxide membrane is presented.[163] Differently from what was previously reported in the literature, in this case previously functionalized GO was used as primary material of the membrane, to which PVA was added to provide mechanical stability. Furthermore, the membrane was prepared in a pressure-assisted setup and presented a highly stacked morphology, another rare feature in this field, to exploit the shorter filtration times specific of these setups. Details on the preparation of the membranes can be found in section 3.1, *Graphene oxide membranes.*

2.3 Active processes

Lithium recovery by means of passive adsorption processes is limited by the efficiency and low capacity rate of such systems. However, the slow lithium diffusion rate in aqueous solutions and the moderate ion-exchange rate with the adsorbents can be improved by applying a driving force. By applying either an electrical potential difference or a current flow, in fact, the system will vary its entropy by carrying on alternative reactions or by facilitating ion migration. In these processes, lithium is removed from a feed solution through redox reactions or electrode polarization. It is then released in a recovery solution short-circuiting the cell, reversing the voltage or the current density direction.[164] Furthermore, these systems allow for a reduction of the use of strong acids and therefore of the environmental impact of the processes also requiring less energy.[56,165–167]

Electrochemical processes can be divided into three main families based on the mechanism of lithium adsorption: ion-pumping (with battery-like electrodes), capacitive deionization (CDI, with asymmetric capacitors), and electrodialysis (ED). However, recently two new methodologies have been proposed: redox-mediated and ion concentration polarization lithium recovery.[168,169] After presenting the three classes of electrochemical processes, an excursus on titanium dioxide and its applications for lithium recovery will be presented.

2.3.1 Ion pumping

The first reports of a battery-like system to recover lithium date back to the nineties when Kanoh et al. studied the selective intercalation into a Pt/λ-MnO_2 electrode and later applied it to geothermal water.[170,171] Since then this technology has attracted a lot of interest but only in 2012 did it receive a technical name to its own by Pasta et al., i.e. electrochemical ion-pumping. [29,53,54,60,65,67,172–174]

Two different strategies have been reported in literature to achieve charge neutrality in the system during the intercalation/deintercalation process: ion capturing electrodes and ion exclusion electrodes. In the first case, chloride ions are captured or released simultaneously to lithium ions on the negative electrode, whereas in the second case Prussian blue analogues release or capture other cations. While the two options are equally possible and present in the literature, their outputs are fairly different: systems with ion capturing electrodes provide higher efficiencies and grades whereas ion exclusion ones are less energy consuming.

Working electrodes in this kind of systems generally use active materials already known in ion sieves or batteries technologies, such as olivine and LMO electrodes, whereas counter electrodes can either be platinum, silver, Prussian blue analogues, bismuth or electroconductive polymers like polyaniline and polypirrole.[164,170,182,173,175–181] In the following, a brief overview only on the working electrode will be given. More information and an accurate analysis on the counter electrode can be found elsewhere.[64]

Lithium phospho-olivine electrodes, LFP, and LMO spinel structures are crystallographically speaking very dissimilar. Whereas spinel structures can accommodate lithium ions in tetrahedral positions, olivines present two different octahedral sites where lithium can insert itself with minor disruptions in the crystallographic structure.[183] An olivine electrode was indeed used coupled with a silver counter electrode in the first mixing entropy batteries and desalination batteries proposed by Pasta et al. in 2012. [172,173,184] In this kind of setup the capture step was thermodynamically favorable and released energy, whereas the release consumed energy. In between these two steps the solutions were mechanically changed and thus a conversion of a sodium rich solution to a lithium rich solution was achieved, both in simple and brine-like solutions.[185]

A different approach can be the use of rocking-chair electrodes in which the negative electrode is prepared by electrochemically pretreating, i.e. de-lithiating, the positive one. An example of this was reported by Zhao et al. with a $LiFePO_4/FePO_4$ electrolytic cell.[186] In this case lithium ion from the feed solution, i.e. the brine, were adsorbed on the negative electrode, while the positive one released them in the recovery solution after which the electrodes were switched.

Unfortunately, olivine electrodes while displaying a higher theoretical capacity and lower insertion potential than LMOs also have lower stability and recyclability.[187] LMOs also show a better selectivity towards both monovalent and divalent cations and have therefore generally been preferred to LFPs in case of magnesium rich brines.[56,61,187] Several studies have been conducted on the optimization of both crystallinity, purity and composition of the LMO electrodes.[175,177,180,181,187–190] Marchini et al., for example, worked with LMOs prepared by thermal decomposition or pulsed laser deposition to avoid the use of conductive additives or binders,[177,180,181,189] whereas Xu et al. prepared their electrode via cathodic deposition.[190]

Rocking-chair systems were proposed for LMO electrodes too, as reported by Zhao et al.[191,192] In these systems, $Li_xMn_2O_4/Li_{1-x}Mn_2O_4$ electrodes were separated by an anion-exchange membrane. Similarly to what reported for the LFP system, lithium ions were adsorbed on the negative electrode and the electrodes were switched between chambers in successive operational steps.

2.3.2 CDI

Capacitive deionization was introduced in the sixties by Blair and Murphy to demineralize water by electrosorption onto porous carbon electrodes.[193] By imitating the working principle of supercapacitors at low potentials, this technique accumulates ions in the electrical double layer (EDL) of a porous electrode and successively release them when the polarization is reversed. Although widely used in the desalination field, only recently did this technique attract attention as a viable candidate for selective removal and/or recovery of target ions.[194] The most common implementations of a CDI setup comprise the addition of ion selective electrodes, and or the use of ion selective membranes.[167,194–201]

Hybrid CDI systems are characterized by battery-like electrodes which can improve both the selectivity and the performance of the setup.[202,203] In the case of lithium recovery, these systems differentiate themselves from ion-pumping ones in terms of counter electrodes. Whereas in ion-pumping applications those guarantee the electroneutrality of the process by adsorbing or releasing ions, in hybrid CDI setups this role is covered by the formation of an EDL on the surface of the capacitive electrode. For these reasons, counter electrodes based on activated carbons are widely used in these setups. This is the case of the system proposed by Kim et al. in which a λ-MnO_2/AC hybrid supercapacitor system was proposed, which adsorbed Li+ ions during the discharge phase and released them during the charging.[204] Similarly, Siekierka et al. reported a system in which the positive electrode was a LMTO where 5 wt.% titania was added to a conventional LMO electrode to improve its hydrophilicity which at the same time increased the adsorption capacity and lowered the energy consumption.[200]

On the other hand, membrane CDI systems try to enhance the counter-ion transport by placing membranes adjacent to one or both electrodes, thus limiting the repulsion effect between co-ions.[196] For lithium recovery applications, ion exchange membranes are the ones most used, however ion exchange resin coatings and nanofiltration ones have also been explored.[194] In the case of Shi et al. two activated carbon electrodes were wrapped into commercial ion exchange

membranes to increase the selectivity towards divalent cations such as magnesium.[198]

An intermediate solution between the two systems can also be found, where both battery-like electrodes and membranes are used. Those systems are generally called hybrid membrane CDI.[197] This is the case of the setup proposed by Lee et al., where a LMO electrode was coupled with an activated carbon one wrapped with an anion exchange membrane. An evolution of the previously presented LMTO setup was also proposed by Siekierka et al.,[200] who in this case wrapped the activated carbon counter electrode in an anion exchange membrane and reached high efficiencies and low energy consumptions.[201]

A different solution was instead adopted by Ryu et al. who attempted to recover lithium by means of electrostatic field assisted desorption. In this case, the electrodes were LMO and activated carbon covered by an anion exchange membrane. The peculiarity of this setup resided in the fact that the adsorption was carried out just like in the case of ion sieves, whereas the desorption was performed by applying an electrostatic field to avoid the use of acidic solutions. Furthermore, by using an electrostatic field instead of a stripping solution, elution of manganese ions from the spinel could be avoided.[166] The application of the electrostatic field during the adsorption process was also investigated and proved beneficial to increase the performances.[167]

2.3.3 ED

Electrodialysis is a membrane-based technique commonly used for desalination purposes, in which an electric field separates ions of different sizes. By adopting suitable membranes and alternating them in stacks to create separate chambers of dilute and concentrated solutions, one can use it to enrich solutions of target ions.[59] Contrary to CDI techniques, the energy consumption is mainly caused by the thermodynamical component of lithium removal and thus cannot be recovered.

Different kinds of membranes can be used in ED: when monovalent selective ion exchange membranes are used this technology is called Selective-ED. In this case the divalent ions will be concentrated in the desalting department but further selectivity among monovalent cations must be achieved. To this end, several functionalizations have been studied, and ionic liquids have also been impregnated onto support membranes.[205–211] Bipolar membranes, formed by layers of polymers with opposite charges, have also been employed for the simultaneous recovery of boron and lithium from the same feed. When employing this kind of membranes, a

disproportionation reaction of water will take place at the hydrophilic junction: lithium will be recovered in the form of LiOH while boron in the form of boric acid.[212–216]

2.3.4 Focus on titanium dioxide nanotubes

Titanium dioxide is one of the most investigated transition metal oxide in the field of material sciences in light of its many interesting and diverse applications. The abundance of polymorphs and mix of peculiar properties make titania an excellent candidate for applications in catalysis, photovoltaics, biomedicine, batteries and environmental applications.[217–219] Amongst its many interesting properties, its biocompatibility, non-toxicity and corrosion resistance are worth-mentioning. Furthermore, all of its crystallographic forms present a band gap of ≈3 eV and are therefore wide-gap semiconductors.[219,220]

Its different polymorphs, rutile, anatase, brookite and TiO_2-B, are displayed in Figure 2.6 with their unit cell and crystallographic axes. While the first three are widely known as titania polymorphs, titanium bronze was discovered by Marchand in 1980 and takes its name from Wadsley bronze, Na_xTiO_2, with which it has many similarities.[219,221,222] TiO_2-B while having more in common with titanates than some of its other polymorphs, is generally considered the most stable of them all due to its small density.[223] However, this ranking is strictly related to the size of the crystallites as the different phases have similar surface energies. Indeed, both theoretical and experimental studies have proven that at the nanoscale anatase is most stable under 11 nm, brookite between 11 and 35 nm and rutile with sizes higher than 35 nm.[224,225] The crystallite size is not the only factor to be take into

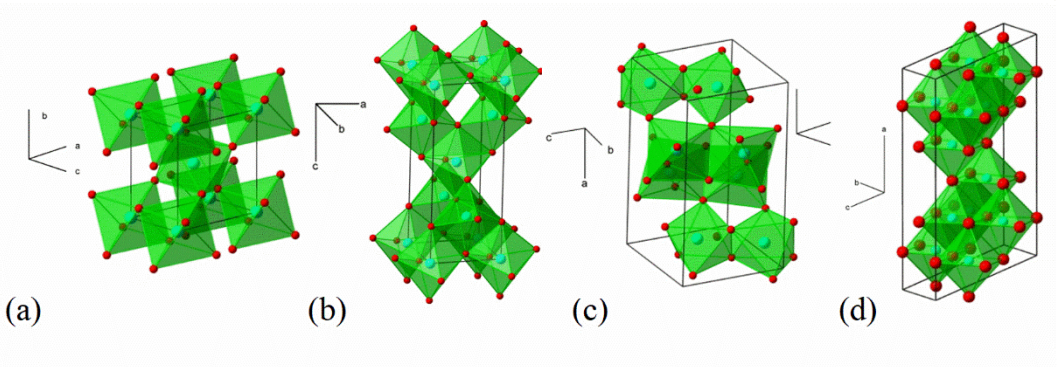


Figure 2.6. Crystallographic structure of (a) rutile, (b) anatase, (c) brookite and (d) TiO_2-B. Titanium atoms are red, oxygen light blue whereas the coordination octahedron is highlighted in green, Adapted with permission.[218] Copyright 2009, Elsevier.

account when talking about the stability of the different titania polymorphs. Indeed, the temperature also heavily influences the relative stability of the phases. While amorphous titania can be easily converted into anatase when annealed in air at temperatures between 300 and 500 °C, rutile can be obtained at temperatures higher than 550°C. TiO_2-(B) instead can be obtained from a thermal annealing of the hydrogen titanate at 500°C. [218,220]

The crystallography of the different polymorphs also influences the lithium insertion mechanisms. While anatase and rutile both have a tetragonal unit cell, brookite has an orthorhombic one and TiO_2-B a monoclinic with a perovskite-like structure. Lithium insertion in TiO_2 polymorphs is widely recognized as anisotropic, with the diffusion happening mostly along the c-axis channels connecting the TiO_6 octahedra interstices.[218,220,226] Lithium is more easily inserted in anatase and TiO_2-B because of smaller distortions in their framework.[218,226–228] Similarly to the stability of the different polymorphs, lithium insertion has also been shown to be size-dependent with smaller crystallites able to host more lithium than bigger ones.[229–232] Amorphous structures were also shown to store even more lithium as a result of the absence of short range order to disrupt.[233] Furthermore, it is worth mentioning that while lithium insertion appears to be a diffusion controlled process in anatase or rutile phases, it appears to be a pseudocapacitive process in TiO_2-B.[218,228,234,235]

In the past twenty years, nanostructures of TiO_2 have been widely investigated, and most of all self-organizing nanotubes (NTs). Those can be obtained through an electrochemical anodic oxidation treatment of a suitable metallic substrate. Anodic oxidation consists in the application at constant voltage of a potential step for a certain amount of time in an electrolytic solution (see Figure 2.7). The window of applied voltages depends on the chemistry of the electrolyte, in case of non-aqueous solutions higher voltages can be reached, and is strictly linked with the diameter of the resulting tubes.[236–238] Instead, the length of the nanotubes will be related to the step duration.[220,239] The presence in the electrolyte solution of fluoride ions is very important for the morphology of the tubes: when too low a compact oxide layer will be formed and when too high no oxide will grow because $[TiF_6]^{2-}$ will become more stable.[240] Similarly, the water content in organic electrolytes will influence both the growth rate and etching speed.[238,241,242] The use of organic electrolytes allows for not only long tubes with large diameters to be grown but also for smooth walls.[242] In the case of ethylene glycol an hexagonal disposition of the tubes is also reached.[243] The use of organic electrolytes containing fluoride ions also causes the resulting nanotubes to have significant amounts of residual fluoride and carbon

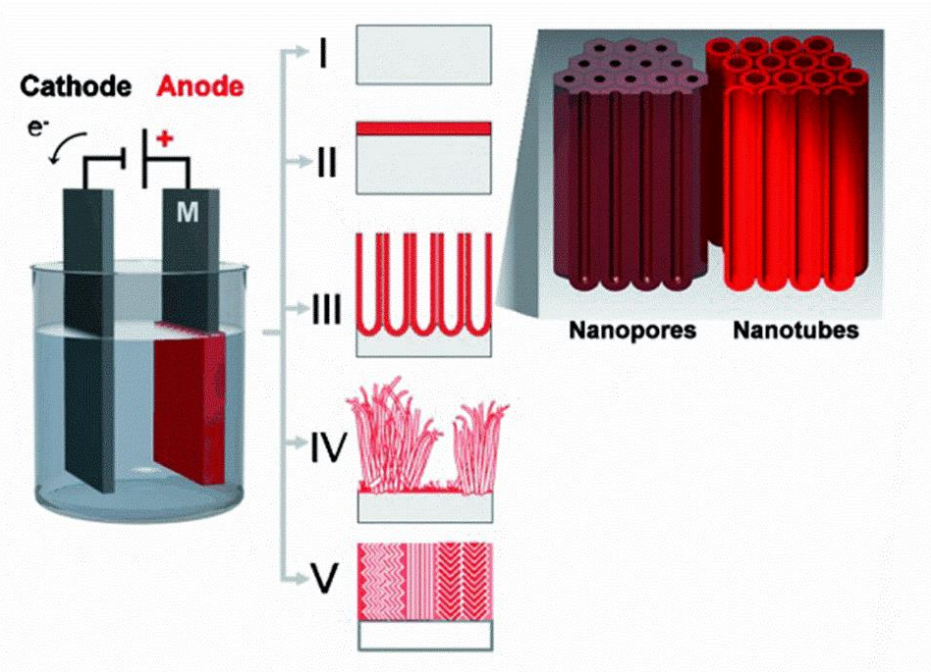


Figure 2.7. Schematic of the electrochemical anodic oxidation process with the possible resulting morphologies: (I) electropolishing of the metal, (II) formation of a compact oxide layer, (III) self-ordered nanopores or nanotubes, (IV) disordered nanotubes, (V) ordered nanoporous layer. Adapted with permission.[220] Copyright 2011, Wiley-VCH.

species as decomposition products of the electrolyte. However, these can be mostly purged during the thermal annealing process to obtain anatase nanotubes from the amorphous as-grown ones.[220]

After the first reports of anodically grown nanotubes from the early 2000s,[244,245] this peculiar morphology has been extensively used for energy and environmental applications, with photovoltaics and batteries at the top of the list.[220,228,254–260,246–253] In particular TiO_2 NTs grown on top of a conductive titanium foil have been directly used as electrodes in LIBs.[261–269] The substrate can indeed work as a current collector in this configuration while the ordered 1D structure of NTs can ensure ionic and electronic conductivity.[270] They have also been used in supercapacitors, more specifically in lithium ion capacitors (LICs),[262,271,272] which are a kind of hybrid supercapacitor device which could be able to bridge the gap between batteries and supercapacitors. Indeed, the former shows high specific energies, while the latter presents high cyclability and specific powers. By displaying at the same time a battery-like and a capacitor-like electrode, LICs should be able to combine the best of both worlds.[273]

When used in electrochemical systems like batteries or hybrid supercapacitors, pre-lithiation of these structures is a well-known strategy to improve the storage capacity of the electrodes. Spinel and titanates structures have also been investigated to this end, both for batteries and for lithium recovery systems, as anticipated in section 2.2.2, *Ion sieves*.[274–280] These classes of material show indeed excellent stability, almost zero stress during lithium ion insertion and removal and regeneration abilities in acidic solutions.[57,76,77,279,281–285]

The conversion of TiO_2 nanotubes into titanates has also been investigated. In particular hydrothermal conversions of TiO_2 NTs into sodium and barium titanate have been explored. The stability of sodium titanate NTs has been studied both in acidic and aqueous environments,[286–288] but those were mostly prepared by hydrothermal treatment from powders. In the case of $BaTiO_3$, instead, Lamberti et al. reported a shape-conserving conversion of anodically grown NTs.[289,290] Lithium titanates have been widely investigated as ion sieves in different morphologies, with their structural stability in acid environment considered superior to the one of LMOs.[70,282,299–305,291–298] However, only few reports exist of lithium spinel or titanates in the form of NTs and none of them were used in an electro-assisted setup. In fact Moazeni and coworkers used hydrothermally grown disordered NTs, while Taghvaei et al. obtained NTs by anodic oxidation but then calcinated the hydrothermally lithiated NTs and used them as powders.[306,307]

In Chapter 5, *Lithiated Titania Nanotubes*, the hydrothermal conversion of anodically grown TiO_2 NTs into $LiTiO_x$ with a procedure similar to the one of barium titanate is presented.[289] These NTs are then used to electrochemically harvest lithium from a lithium rich solution. Their morphological stability and recyclability is investigated both in an organic electrolyte and then in aqueous solutions.[308] While the capturing phase of the process is done under electrochemical conditions, the release part, i.e. the de-lithiation of the electrodes, is performed in open circuit conditions, reversing the procedure used by Ryu et al.[166] who used an electrostatic field to avoid the use of acids. Details on the anodic oxidation parameters and on the electrochemical testing parameters can be found in the experimental section 3.2, *Lithiated titania nanotubes*.

Chapter 3

Experimental

In this chapter, the experimental part will be presented. The synthesis and filtration protocols of graphene oxide (GO)-based membranes will be introduced first. The preparation of titanium dioxide nanotubes (NTs) via anodic oxidation and their hydrothermal conversion into lithium titanium mixed oxide ($LiTiO_x$) will then be presented as well as the characterization performed on them.

An overview of the characterization techniques used in both setups will then be provided. The techniques were divided into physico-chemical and electrochemical analyses. The former comprises: scanning electron microscopy (SEM) to investigate the morphology, X-Ray diffraction (XRD) to assess the crystallographic properties, Raman and Infrared (IR) spectroscopies, Z-potential, thermogravimetrical analyses (TGA), conductivity and Inductively Coupled Plasma (ICP) Mass Spectrometry measurements and finally X-Ray Photoelectron Spectroscopy (XPS). Among the electrochemically techniques, voltametric, potentiodynamic techniques, and electrochemical impedance spectroscopy (EIS) will be presented. A short introduction to each technique will focus on its fundamentals, then the details of its use for each setup will be addressed.

3.1 Graphene oxide membranes

3.1.1 Synthesis

The membranes used in this project were of three different types: pristine GO, crown ether functionalized graphene oxide membranes (f-GO), and f-GO with the addition of a polymeric binder.

Commercial GO flakes (Single layer GO, 300-800 nm of lateral dimension, Cheap Tubes Inc., Cambridgeport, VT, USA) were functionalized following the procedure adapted from a previous work via carbodiimide esterification.[135] The GO flakes were sonicated for one hour at 40 kHz in Dimethyl sulfoxide (DMSO, >99.5%) in an ultrasonication bath (LBS2, Falc Instruments SRL, Treviglio, Italy). No further selection of their size by centrifugations was performed. N,N'-Dicyclohexylcarbodiimide (DCC, >99%) and 4-(Dimethylamino)pyridine (DMAP, >99%) were used as catalysts for the esterification reaction and added to the solution with a 10:20:1 weight ratio of GO:DCC:DMAP. After a 30 minutes sonication a mixture of 2-Hydroxymethyl-12-crown-4 (2M12C4E, >95%) in DMSO (previously sonicated for one hour) was added with a 4:1 weight ratio of 2M12C4E:GO. The resulting solution of functionalized flakes, called f-GO, was further sonicated for 2 hours at 40 kHz. If no otherwise specified the reagents were provided by Sigma Aldrich, St. Louis, MO, USA.

In the case of f-GO membranes with binder, the binders were added in a concentration of 40 wt.% to the solution in DMSO and sonicated for 30 minutes. Three materials were tested: pristine GO, and the two polymeric binders Poly(vinyl alcohol) (PVA, M_w 31000-50000, 98-99%) and Poly(vinylidene fluoride) (PVDF, M_w 534000). The solvent extraction was performed through successive centrifugations with acetone, after which the flakes were put in deionized water and sonicated for 30 minutes.

The membranes were obtained by filtrating the water dispersions on top of a polycarbonate support membrane (Whatman® Nuclepore™ Track-Etched Membranes, diameter 47 mm, pore size 0.1 μm). Two different setups were used to prepare the membranes (see Figure 3.1): a vacuum assisted filtration apparatus (VWR, Radnor, PA, USA) and a dead-end filtration apparatus (Sterlitech HP4750, USA). These two setups were chosen because they are the two providing more ordered flakes in a stacked morphology. However, the pressure-assisted setup was ultimately chosen in light of the superior order degree it could provide.[155] The

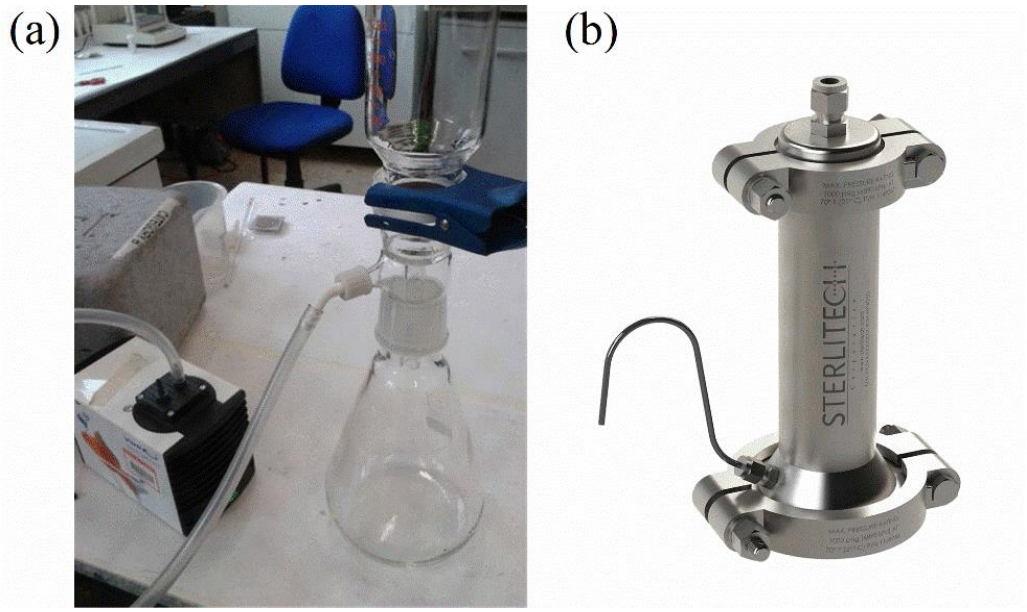


Figure 3.1. (a) Vacuum and (b) dead-end filtration apparatuses employed in the production and use of the GO-based membranes.

membranes were then used as prepared, without performing any further treatment to chemically graft or polymerize the polymeric binders, which acted as physical spacers between the flakes to stabilize the mechanical properties of the membranes.

3.1.2 Filtration protocol

The filtration properties of the membranes were characterized in the pressure assisted dead-end filtration apparatus. Different pressures in the range 1-5 bar were investigated using a nitrogen tank as pressure source. The permeability curve of the different membranes was firstly evaluated by filtering specific amounts of deionized water (DIW, Direct-Q 3 UV, Merck Millipore, Burlington, MA, USA) at increasing pressure, as reported elsewhere.[141]

Successive filtrations of chloride salts and eluting solutions were performed to assess the selectivity of the membranes. In the optimized protocol five successive filtrations of each couple of solutions were performed, deionized water was flushed in the chamber after each filtration to avoid any contamination in the hold-up volume and each membrane was tested for at least three filtration cycles. Each solution underwent conductivity measurements after each filtration and ICP mass

measurements were conducted at the end of each filtration cycle. The solutions tested were lithium chloride (LiCl, >99%), sodium chloride (NaCl, >99.5%), potassium chloride (KCl, >99%, Carlo Erba, Italy), magnesium chloride ($MgCl_2$, >98%), calcium chloride ($CaCl_2$, >99%) and hydrochloric acid (HCl, 37%). 15 ml of each solution was filtrated, and the concentrations used were 1 mM for the salts and 100 mM for the acid.

3.2 Lithiated titania nanotubes

3.2.1 Anodic oxidation

Titanium dioxide nanotubes were anodically grown on a Titanium foil substrate (0.1 mm, > 99.9%, MTI Corporation, USA) following the procedure reported elsewhere. [309,310] The samples were subjected to a thorough cleaning pretreatment consisting in a 10 minutes sonication in DIW followed by etching in hydrofluoric acid 1 wt.% (HF, 40%, Carlo Erba, Italy) and abundant rinsing in DIW. The anodic oxidation was performed in two different steps, the first one to create the tube template and the second to grow highly ordered nanotubes. Both were performed under continuous stirring in a thermostatic bath at 25 °C in an ethylene glycol (EG) based electrolyte. The electrolyte was made of 0.5 wt.% of ammonium fluoride (>98%) and 2.5 wt.% of DIW in EG (≥99.5%, Honeywell, NC, USA). Titanium foil was used as both working and counter electrodes.

The tube template was created during the first anodization step while 60 V were applied for five minutes by a constant power generator (GW Instek SPD- 3606, Good Will Instruments, Taiwan). The layer obtained was then removed in hydrogen peroxide (30%) by ultrasonication. The second anodization step was performed applying a constant potential of 60 V for 15 minutes to grow a highly ordered layer of amorphous titanium dioxide nanotubes, followed by a thorough wash in DIW.

Since as-grown titania nanotubes are in the amorphous phase, a thermal annealing process was performed for 30 minutes at 450 °C in a muffle furnace (Muffle Furnace L9/11, Nabertherm GmbH, Germany) to crystallize them into the anatase phase.

3.2.2 Hydrothermal conversion

Titania NTs were subjected to hydrothermal conversion into lithium titanium mixed oxide ($LiTiO_x$) in Teflon-lined stainless-steel acid-digestion vessels (Parr general purpose acid digestion vessel 23 mL, Parr Instrument Company, Moline, IL, USA).

The samples were immersed in lithium hydroxide solutions (LiOH monohydrate, >99%, Alfa Aesar, USA) of different concentrations and heated for two hours in a muffle furnace. Several concentrations in the range 0.25 to 1 M and temperatures in the range 120 °C to 200 °C were investigated. The samples were then cooled and removed from the vessels, then rinsed in DIW and dried under nitrogen flow.

3.2.3 Preparation of the carbon counter electrodes

Highly capacitive carbon-based counter electrodes were prepared by means of a slurry composed of 5 wt.% Polytetrafluoroethylene (PTFE, 60 wt.% dispersion in water) acting as binder, 10 wt.% carbon black (Timcal Super C45, CES Cambridge Energy Solutions, UK) acting as conductive agent and. 85 wt.% activated carbon (Kuraray Activated Carbon, Japan). The components were dispersed in ethanol and continuously stirred at 100 rpm at 60°C until the amalgama became a wet dough suitable for calendering. The flat, self-sustaining electrodes were shaped into cylindrical tablets by means of a punch tool of 18 mm diameter and then baked at 60°C to remove any trace of the solvent.

3.2.4 Cell assemblage and testing

Lithiated and titania nanotubes underwent different morphological and physico-chemical characterizations to assess their ability to recover lithium from different media. In particular, NTs underwent several electrochemical measurements (EC) in different setups, all connected to a VMP3 Potentiostat (version 11.34, Biologic, France). The *history* of these electrodes is as follows: NTs of both TiO_2 and $LiTiO_x$ were first tested in an organic electrolyte and three electrodes configuration to only focus on Li^+ diffusion in our structure. Before and after these EC measurements the electrodes were investigated in terms of both morphology, crystallinity and composition.

In the case of organic measurements, the electrochemical characterizations were performed in three-electrodes PAT-Cells (EL-CELL, GmbH, Germany). The experimental setup of these stacked cells is shown in Figure 3.2 with the electrical connections indicated with standard labels. The working electrode (WE) is the NT layer grown on top of Ti foil and dried overnight at 120°C. The WE was assembled in a PEEK insulation sleeve with a lithium ring reference (REF) and a double-layered FS-5P separator (200 um, EL-CELL GmbH, Germany). The separator was soaked with the organic electrolyte (LiPF6 1 M in EC:DMC 1:1 Solvionic E00350)

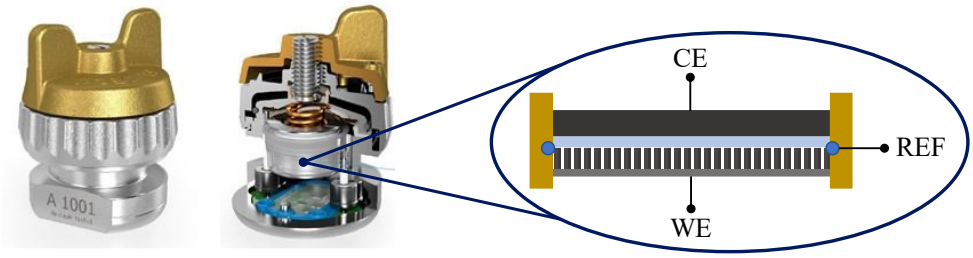


Figure 3.2. Cell configuration for the EC analyses in organic electrolyte. From the bottom the NTs grown on top of Ti foil constitute the WE, which is in contact with the separator soaked with the organic electrolyte on top of which is the thick active carbon-based counter electrode.

on top of which the high capacitance thick active carbon-based counter electrode (CE) was in contact with the upper plunger and ended the stack.

Afterwards, $LiTiO_x$ NTs were subjected to a de-lithiation process in HCl 0.1 M for 48 hours at room temperature to investigate their recyclability and stability, after which they underwent the same physico-chemical analyses as $LiTiO_x$. This de-lithiated NTs were called *de*Li-TiO_x and were then again tested in organic electrolyte under the same conditions as $LiTiO_x$ NTs. The de-lithiation process was conducted in a two-electrode configuration in Aqu EC Cell (EL-Cell GmbH, Germany), with a Silver 20 separator (DreamWeaver, USA) and two symmetrical $LiTiO_x$ electrodes (see Figure 3.3).

$LiTiO_x$ NTs were finally tested in aqueous solutions in the same Aqu EC Cell, with a Silver 20 separator (see Figure 3.4). In this case the counter electrodes were again thick active carbon-based slabs, and these measurements were conducted in LiCl, NaCl or LiCl/NaCl solutions of different concentrations (10 mM to 1M).

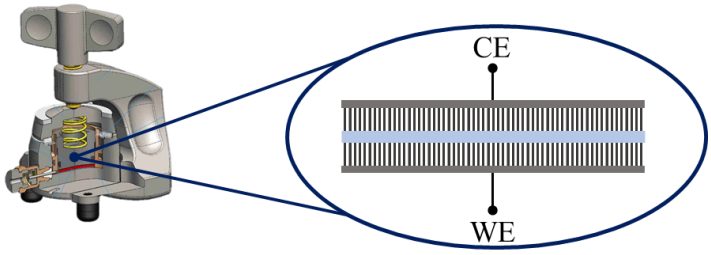


Figure 3.3. Cell configuration for the de-lithiation process. In this case two symmetric NTs electrodes were used as both WE and CE, separated by the acidic solution and a glass fiber separator.

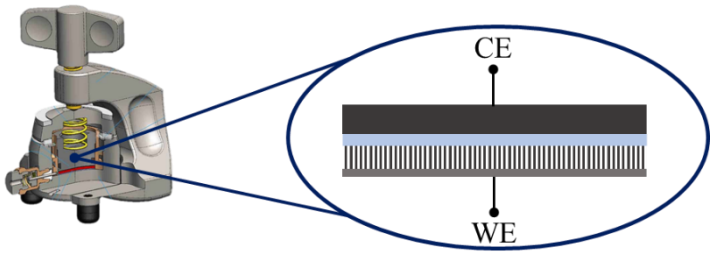


Figure 3.4. Cell configuration for the aqueous EC analyses. In this case the WE is made of the NTs grown on the Ti foil, and the CE is the thick active carbon-based counter electrode. Those were separated by the glass fiber separator soaked in aqueous electrolyte.

3.3 Physico-chemical analyses

3.3.1 Scanning Electron Microscopy

Morphological characterizations were performed with Field Emission Scanning Electron Microscopy (FESEM). In this advanced imaging technique, an electron beam collides with the surface of the specimen and topographical and elemental information can be obtained from the response of the sample. The interaction between the primary beam and the surface has a volumetric distribution and results in several signals, depending from the depth of the interaction. Among these, the most used are secondary electrons, back-scattered electrons and X-rays.

Secondary electrons are the result of inelastic interactions between the beam and valence electrons and have very low energy (< 50 eV). They are released from the first nanometers and are highly localized, giving information on the topography of the sample. Back-scattered electrons are instead produced by elastic interactions with the nuclei. They have higher energies and larger escape depth. With the help of specific detectors, they can give images with atomic number contrast. However, these images have lower resolution due to their larger escape path. Finally, characteristics X-rays originate even deeper in the sample when the electron beam displaces an inner shell electron, causing an electron transition and the release of photons. They can be analyzed by Energy-Dispersive Spectroscopy (EDS) or Wavelength-Dispersive Spectroscopy (WDS) to map the presence and distribution of the different elements in the sample.

In the experiments herein reported, a FESEM Supra 40 (Zeiss, Oberkochen, Germany) equipped with a Si(Li) detector (Oxford Instruments, Abington, UK) for energy-dispersive X-ray spectroscopy was used to investigate both the membranes and the nanotubes. In the case of GO-based membranes, their morphology and the interaction between the flakes and the polymeric binders were investigated. When working instead with the NTs, the evolution of their morphology was examined after the hydrothermal conversion, the electrochemical cycling, and the delithiation.

3.3.2 X-Ray Diffraction

X-Ray Diffraction (XRD) is a technique that allows to investigate the crystalline structure of materials. Among the different information that can be extracted from a diffractogram one can find: the chemical composition, crystallite size, crystallographic phase (qualitatively and quantitatively), orientation, layer thickness and residual stresses.

XRD crystallography takes advantage of the fact that a crystallographic atomical lattice can be seen as a regular array of atoms and an incident X-Ray beam is an electromagnetic radiation. The elastic scattering of the radiation will undergo constructive interference in the directions described by Bragg's law (Equation (3.1) which in turn will give rise to a diffraction pattern:

$$n\,\lambda = 2\,d_{hkl}\,sin\theta_{hkl} \tag{3.1}$$

where n is an integer, λ is the wavelength of the radiation, d_{hkl} is the interplanar distance and θ_{hkl} is the diffraction angle (see Figure 3.5).

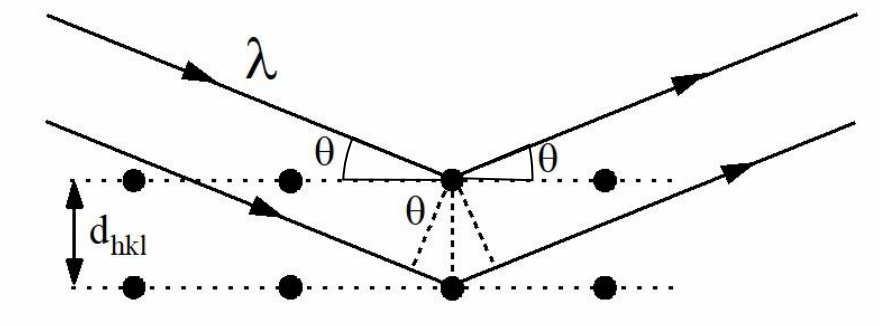


Figure 3.5. Geometric representation of Bragg's law.

Since each crystallographic phase has different lattice parameters, the pattern obtained from XRD measurements can be used to identify an unknow crystallographic phase. The crystallite size can also be obtained via the diffraction patterns, following Scherrer's Equation (Equation (3.2)):

$$B(2\theta) = \frac{K}{L\,cos\theta} \tag{3.2}$$

where $B(2\theta)$ is the full width at half maximum of the peak, K a dimensionless shape factor, L is the crystallite size and θ the diffraction angle.

In the experiments herein presented, XRD measurements were performed on a X'Pert MRD Pro X-ray diffractometer (Malvern Panalytical, UK) with a Cu Kα source (λ=1.5405980 Å) and the obtained diffractograms were further analyzed with the Highscore Plus Software (Malvern Panalytical, UK). All measurements were recorded in Brag-Brentano configuration, with a step size of 0.026° and a scan speed of 200 s step^{-1}.

In the case of the GO-based membranes, the interlayer between the flakes of GO in the different kind of membranes was obtained through XRD measurements, while when working with the NTs the presence and evolution of the different crystallographic phases was thus monitored.

3.3.3 Raman spectroscopy

Raman and Infrared (IR) spectroscopies are complementary molecular spectroscopy techniques. In Raman spectroscopy, the sample is irradiated with a monochromatic excitation beam and the scattered light is then detected. This signal is analyzed in terms of frequency and polarization: the shift between the incident and scattered beam, called Raman Shift, depends on the intrinsic properties of the sample and its change in polarizability. Raman spectroscopy relies on inelastic scattering interactions in the UV-near IR region and investigates the symmetric vibrational modes of the molecules.

Raman spectroscopy is widely used to investigate carbonaceous materials. Its versatility and high sensitivity to covalent bonds make it unvaluable to determine the electronic properties and structure of graphene-based materials. The characteristics peak of graphene-based structures are the so called G and D peaks (see Figure 3.6). The first one pertains to the graphitic structure and is usually found at ~1575 cm^{-1}, whereas the D (and 2D) peaks arise from the presence of defects in

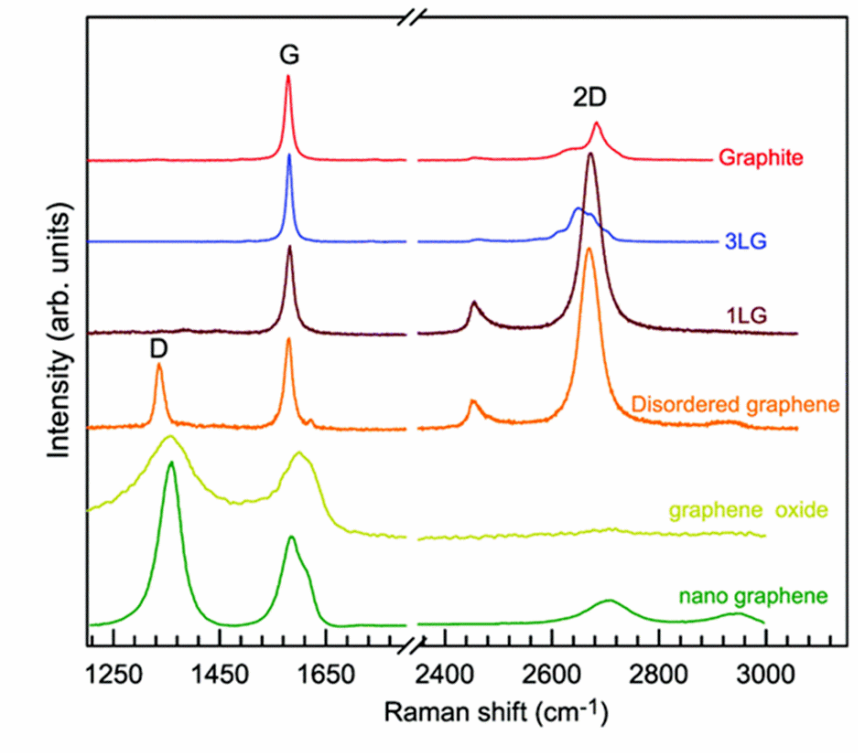


Figure 3.6. Raman spectra of graphene-based materials: from top to bottom graphite, 3-layers graphene, single layer graphene, disordered graphene, graphene oxide and nano graphene. Reproduced with permission.[311] Copyright 2018, Royal Society of Chemistry.

the graphitic structure. The D peak can be found around 1355 cm^{-1} and its intensity is proportional to the crystallite size, and the 2D peak is absent in graphene oxide structures. The crystallinity of a graphene-based sample is generally given by the ratio of the D and G peaks.[311]

In the work herein reported, Raman Spectroscopy was performed on the GO-based membrane to investigate the possibility of further reduction of the GO flakes during the functionalization and the preparation of the nanocomposite membranes. Spectra were recorded on a InVia Micro-Raman (Renishaw, England) with a 785 nm excitation laser. Acquisitions were performed with a 20x microscope objective at 5% of the nominal power.

3.3.4 Infrared spectroscopy

IR spectroscopy focuses on the adsorbed portion of the incident beam, and is sensitive to changes in the dipole moments of the molecules, hence its complementarity with Raman spectroscopy. In this case a multi-frequency

excitation beam is directed onto the sample which only adsorbs the frequencies matching its asymmetrical vibrational modes. IR spectra can be computed in terms of adsorbance, more suited for quantitative analyses, or transmittance, more suited for qualitative analyses.

IR adsorption bands can provide several useful information on the polar bonds present in the molecules and are unique to functional groups. Their shape, intensity and position all address different aspects: the shape relates to the local interactions of the functional group, while their intensity depends on the efficiency of the energy transfer. Finally, their position is correlated to the vibrational mode energy. Two different regions can be identified in an IR spectrum: functional groups are found at $\tilde{\nu} > 1500$ cm^{-1}, whereas the region for which $\tilde{\nu} < 1000$ cm^{-1} is generally called *fingerprint region*.

FTIR analyzes were performed on the GO-based membranes as they were to assess the success of the functionalization with the crown ether molecules. They were completed in attenuated total reflection (ATR) with a step size of 0.4 cm^{-1} and a scan speed of 6.33 cm s^{-1} on a Nicolet 5700 FTIR (Thermo Fisher Scientific, Waltham, MA, USA).

3.3.5 Z-Potential

Every time a solid and a liquid come into contact, an electronic charge is developed on the solid surface and a superficial electrical double layer (EDL) is formed. This double layer is usually divided into two components, the Stern layer, where the ions are strongly bound to the particle, and the diffuse layer where the bond is less firm.

In this diffuse layer, we can further distinguish a zone in which the ions are still attracted, however feebly, and form a stable system, and an outer one where the dispersant is the stable system. The Z-potential ζ is defined as the potential at the radius of hydrodynamic shear, and can indicate whether a colloidal solution is stable or not. It can be measured through the optical properties of a very diluted solution to which a varying electric field is applied, by counting the number and speed of the particles moving in the presence of a light source.

This superficial charge is of particular interest in the case of membranes, where it can affect the electrostatic repulsions between the membrane surface and the ions or charged molecules of the solution. In the case of GO-based membranes, which are generally negatively charged, the functionalization can change their surface chemical properties. In the following, the surface chemical properties of the

different GO membranes investigated were tested in aqueous solutions with a concentration of 0.05 mg ml^{-1} of GO by Zetasizer Nano ZS90 (Malvern Panalytical, Malvern, UK).

3.3.6 Thermogravimetric analyses

Thermogravimetric analysis (TGA) is an important characterization technique which monitors the weight variation of a specimen as a function of time and temperature under controlled atmosphere. In order to underline the weight losses as a function of the increasing temperature it can be useful to plot not only the weight variation but also its derivative (DTG), which is indicative of its degradation speed. This kind of measurement can be coupled with IR spectroscopy to analyze the gases released during the degradation the sample.

TGA were performed on approximately 8 mg of each GO-based membrane tested in 100 µl alumina pans with a TGA1 instrument (Mettler Toledo, USA). The analyzes were conducted under nitrogen gas (50 ml min^{-1} rate) with a heating rate of 10 °C min^{-1}.

3.3.7 Conductivity measurements

Conductivity measurements were conducted on the solutions filtrated by the GO-based membranes to qualitatively monitor whether the H^+/Li^+ was successful. As previously said in 3.1.2, conductivity measurements were performed on each solution at the end of each filtration. Five values for each solution were recorded and standard deviations were calculated for each sample. The measurements were performed on an Edge HI2003 Conductivity Meter (Hanna Instruments, USA).

3.3.8 ICP mass spectrometry

ICP mass measurements were conducted on the solutions filtrated by the GO-based membranes to quantify the amount of lithium/sodium recovered in the eluting solutions after each filtration cycle. Those were performed on diluted nitric acid digested 1:1000 diluted solutions with an iCAP Q ICP-MS (Thermo Fisher Instruments, USA) and the data were processed with the Thermo Fisher ICP Software.

3.3.9 XPS

X-Ray Photoelectron Spectroscopy (XPS) is a surface spectroscopic technique based on Einstein's photoelectric effect. By irradiating the sample surface with X-Rays, elemental and chemical information can be obtained from the kinetic energy of the core photoelectrons ejected, by means of Equation (3.3):

$$BE = h\nu - KE - \Phi \tag{3.3}$$

where *BE* is the binding energy, $h\nu$ is the x-ray energy of the source (generally Mg K_α or Al K_α), *KE* is the kinetic energy of the photoelectrons, and Φ the spectrometer work function (a few eV). By analyzing the binding energies it is possible to identify the elemental composition of the first few nm of the sample and eventual contaminations. The chemical state of the elements of the sample can also be obtained, meaning their oxidation sate, binding energy, chemical environment and functional groups. Two different spectra can be obtained from an XPS analysis: survey spectra are the result of wide energy scans and are made to obtain a general idea of the elements in the samples, whereas high resolution (HR) spectra focus only on one element at the time to obtain information on its spin-orbit coupling.

XPS analyses were performed on the different NT samples before and after the electrochemical characterizations. They were conducted on 500 µm x 500 µm areas with a PHI 5000 VersaProbe system (Physical Electronic, USA), equipped with Al K_α radiation (1486.6 eV) as X-ray source. Survey and HR spectra were collected and analyzed with a CasaXPS software (version 2.3.18). BE calibrations were performed according to the C 1s peak position for adventitious carbon at 284.8 eV and a Shirley background subtraction was completed before deconvoluting the HR spectra into individual mixed Gaussian-Lorentzian peaks. The analysis of HR XPS spectra resulted in the semi-quantitative analyses herein reported.

3.4 Electrochemical analyses

The term electrochemical analyses groups all the techniques in which an electrical stimulus is used to investigate the chemical reactivity of a specimen. By means of this kind of techniques one can investigate the material behavior at interfaces by either controlling the potential (potentiostatic measurements) or the current (galvanostatic measurements). The techniques used in this work are:

- Voltametric techniques
- Electrochemical Impedance Spectroscopy

- Other potentiostatic measurements

Before going into the details of the techniques, it is important to address a few fundamentals of the interfacial interactions, i.e. the nature of these interfaces. As anticipated in 3.3.5, (page 35), when in contact with an electrolytic solution, an electrical double layer will rise at the interface with the electrode due to the charge redistribution. The simplest and first model was the *Helmholtz layer model* in which the interface can be modeled as a parallel plate capacitor (see Figure 3.7 a). In this early model the potential was supposed to change linearly between the plane of the electrode and the one created by the hydrated ions in the bulk solution, called Outer Helmholtz Plane (OHP). Unfortunately, this didn't account for the thermal motions that would disturb the rigid plane of charge. A model with mobile ions was then proposed in the *Gouy-Chapman model* (see Figure 3.7 b). However, this model was still lacking some elements as it underestimated the complexity of the double layer structure, with results accurate only in the case of diluted solutions. These two models were then combined in the *Stern model* (see Figure 3.7 c) and successively the *Grahame model*, which assumed the presence of both fixed and mobile charges depending on the distance from the electrode surface.

Electrochemical measurements are usually preceded by an open circuit potential (OCP) to assess the initial state of the cell. As the name suggests, in this

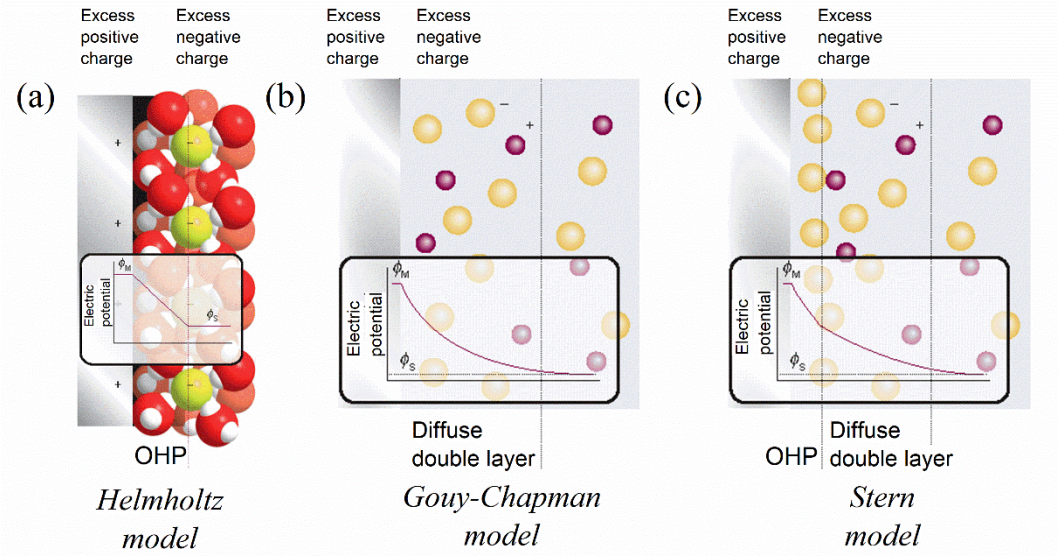


Figure 3.7. (a) Helmholtz, (b) Gouy-Chapman, and (c) Stern models of the electrical double layer. Adapted from [341] Copyright 2010, Oxford University Press.

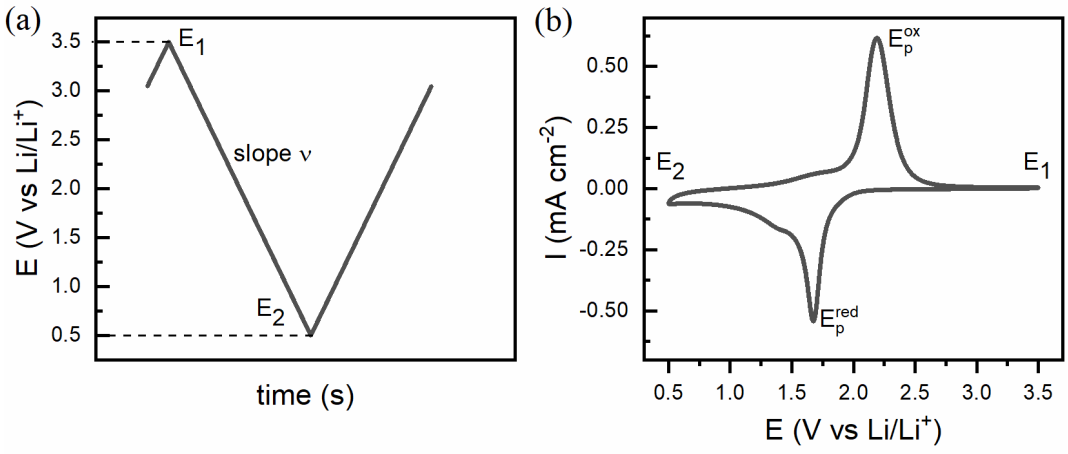


Figure 3.8. (a) Potential-time profile applied and current-voltage profile measured in a typical CV experiment on TiO_2 electrodes with a scan rate of 0.59 mV s^{-1}.

kind of measurement the potential of the cell is monitored until the equilibrium is reached while no current flows in it.

3.4.1 Voltammetry techniques

Voltammetry techniques are powerful potentiostatic techniques that make an investigation of the kinetic evolution of interfaces possible. In this kind of sweep potential techniques, the potential between the WE and the REF is set to vary between two extremis at a constant rate named *scan rate* (ν), while the current between the WE and CE is measured. In this work, two different types of voltammetries were conducted on the titania-based electrodes: Cyclic voltammetries (CV) and Linear Sweep Voltammetries (LSV). While in the first case the potential is repeatedly increased and reduced between the two limits (E_1 and E_2, see Figure 3.8 a) in a triangular profile, in LSV only one sweep direction is employed. In the following, the IUPAC notation will be adopted, following which the forward sweep (with increasing potentials) is investigating the oxidation phase and the reverse one the reduction.[312,313] A typical profile of CV for a TiO_2 electrode in reported in Figure 3.8 (b): one can see the so-called *duck shape* of CV in organic electrolyte with two well defined peaks for the oxidation and reduction reaction.[313,314]

The shape of the cyclic voltammogram can already give some information on the kind of the undergoing reaction. A reaction is considered reversible when the potential difference between the two peaks $\Delta E = E_p^{ox} - E_p^{red} < 59\,mV$.

Furthermore, the position of the peaks, their shape, their current densities are valuable information on the investigation of the electrode kinetics.

Different data analyses were conducted on the CV measurements conducted in organic electrolyte. The equations used to compute the energetical parameters for each cycle are the following:

- the specific charge Q [mAh cm^{-2}] of each branch is given by Equation (3.4):

$$Q = \frac{1}{3600\ Area}\int_{t}^{t+\Delta t} I(t)\ dt \tag{3.4}$$

- the Coulombic efficiency, which can be seen as an index of the proper functioning of the cell, with minimal self-discharge phenomena, by Equation (3.5) for anodic materials. Similarly, an energetic efficiency can also be calculated as the ratio between the energies of the two branches.

$$\eta_{Coulomb} = \frac{Q_{ox}}{Q_{red}} \tag{3.5}$$

Furthermore, the analysis of the intensity of the current peaks and their relationship with the applied scan rate was used to investigate whether the processes were diffusion or surface-controlled.[315] As a matter of fact, the generical relationship between the resulting current and the applied scan rate in a voltammogram can be expressed with Equation (3.6):

$$I(V) = av^{b} \tag{3.6}$$

By plotting the *log(I)* as a function of *log(v)*, one can determine the value of the slope *b* (this can also be referred to as *b-value analysis*). The two limiting cases are processes diffusion-controlled *(b=0.5)* and surface-controlled *(b=1).* In the case of diffusion-controlled processes one can also apply the Randles-Ševčik relationship (Equation (3.7) to evaluate the diffusion coefficient D (in cm^2 s^{-1}), as a solution for the Nernst equation. For irreversible couples, characterized by a dependence of the voltage peak from the scan rate, Randles-Ševčik can be rewritten as Equation (3.8):

$$I_p = 0.4958\, n\, FAC^* D^{0.5} \left(\frac{\alpha n F}{RT}\right)^{0.5} \nu^{0.5} \tag{3.7}$$

$$I_p = 3 * 10^5\, n\, AC^* D^{0.5} (\alpha n)^{0.5} \nu^{0.5} \tag{3.8}$$

where I_p is the current peak in A, *n* is the number of electrons per reaction, *A* is the area in cm^{-2}, *C** is the concentration of mobile ions in mol cm^{-3}, α the transfer coefficient and *F, R,* and *T* have their usual meaning. A rough estimation of the transfer coefficient can be obtained from Randles-Ševčik equation. Indeed by applying (3.7) to the oxidation and reduction branches, assuming that the diffusion coefficients for insertion and disinsertion of lithium are the same and that the anodic and cathodic charge transfer coefficients follow equation (3.9), one can easily obtain equation (3.10):

$$\alpha_{ox} + \alpha_{red} = 1 \tag{3.9}$$

$$\alpha_{ox} = \frac{slope_{ox}}{slope_{ox} + slope_{red}} \tag{3.10}$$

Particular attention should be paid to the choice of the area considered. Two choices are possible: the geometrical area and the superficial area. In the case of porous electrodes, such as the ones herein presented, an estimation of the superficial area was attempted by using the formula of the capacitance C for a parallel plate capacitor (3.11), to which the system can be assimilated at high frequencies:

$$C = \frac{\varepsilon_r\, \varepsilon_0\, A}{\lambda_D} \tag{3.11}$$

where $\varepsilon_0, \varepsilon_r$ have their usual meaning of dielectric permittivity of the vacuum and dielectric constant, A is the geometric area and λ_D the Debye length, given by (3.12), where k_B is the Boltzmann constant, N_A Avogadro's constant, *e* the elemental charge and *z* the valence:

$$\lambda_D = \sqrt{\frac{\varepsilon_r\, \varepsilon_0\, k_B\, T}{N_A\, C^*\, e^2 z^2}} \tag{3.12}$$

In the case of mixed control, i.e. $0.5 < b < 1$, it is instead possible to rewrite the relationship between the current and the scan rate (3.6) as Equation (3.13)

$$I(V, \nu) = k_1(V)\nu + k_2(V)\nu^{0.5} \tag{3.13}$$

In order to deconvolute the diffusion and capacitive contributions of the total current, it is possible to adopt the procedure of Dunn et al.[316,317] The so-called *Dunn method* rearranges Equation (3.13) by dividing both terms by $\nu^{0.5}$ and finds the value of the constants k_1 and k_2 at specific potentials across multiple scan rates. It then allows to quantify both contributions in relation to the total current. However, ohmic losses at increased scan rates are not taken into consideration in this method, which can therefore be applied only at relatively low scan rates.

CV on TiO_2, $LiTiO_x$ NTs and *de*Li-TiO_x were conducted in both organic and aqueous electrolytes at different scan rates. Linear Sweep voltammetries were also conducted on $LiTiO_x$ samples in aqueous electrolytes.

In the case of the measurements performed in $LiPF_6$ 1 M in EC:DMC 1:1, the CVs were performed in a three volts potential window [0.5:3.5] V vs Li/Li^+ with a 100 μV resolution, after conducting OCV and EIS measurements. Different scan rates in the range 0.05 mV s^{-1} to 200 mV s^{-1} were used in both linear and square root spacing over the decades. If not further specified, the current was averaged over ten voltage step and measured on the second half of each. The number of cycles performed increased with the scan rate: four were conducted for scan rates smaller than 2 mV s^{-1}, six in the range 2-10 mV s^{-1}, and finally eleven for higher scan rates. The bandwidth was selected in all measurements to allow the system to remain stable.

In the case of aqueous solutions, lithium and sodium chloride solutions were used as electrolyte. In this case, as mentioned when the cell configurations were explained in section 3.2.4, two-electrode measurements were conducted in a [-2;0.5] V potential window with a 100 μV resolution, after conducting OCV and EIS measurements. The scan rate was 1 mV s^{-1} for all measurements, and the current was measured on the whole step and averaged over ten voltage steps. Six cycles

were performed per each sample, and the bandwidth was selected in all measurements to allow the system to remain stable. Half of the specimen were subjected to a LSV after the CV measurements in order to investigate the behavior at half cycle. The scan rate of LSV was set to 0.5 mV s^{-1} while the other parameters were left unchanged.

3.4.2 EIS

Electrochemical impedance spectroscopy is a technique in which a small sinusoidal AC signal V_0 of frequency *f* is applied to the cell and its response is recorded (in the case of potentiostatic EIS). The signal can be written as Equation (3.14):

$$V(f,t) = V_0 \sin(2\pi f t) \tag{3.14}$$

whereas the cell response will be a sinusoidal current with same frequency but different phase. When conditions of stability, linearity, causality and finiteness are met within an experiment, one can define the complex impedance spectroscopy Z by means of Equation (3.15) following Ohm's law:

$$Z(f,t) = \frac{V(f,t)}{I(f,t)} = |Z(f)|e^{j\varphi} = Z'(\omega) - iZ''(\omega) \tag{3.15}$$

with $|Z|$ the impedance modulus, φ the phase angle, *j* the imaginary unit and *Z'* and *Z''* the real and imaginary part of the impedance, respectively. It follows from Euler's relationship that $Z' = |Z|cos\varphi$ and $Z'' = |Z|sin\varphi$.

When conducting an EIS experiment, one will record a different set of numerical parameters which can be either *Z'* and *Z''* or the modulus $|Z|$ and phase angle φ as a function of the frequency *f*. Generally the real and imaginary part are obtained in frequency resolved analyses, while modulus and phase angle can be computed with Equations (3.16) and (3.17):

$$|Z|(f) = \sqrt{Z'^2 + Z''^2} \tag{3.16}$$

$$\varphi(f) = \arctan\left(\frac{Z''}{Z'}\right) \tag{3.17}$$

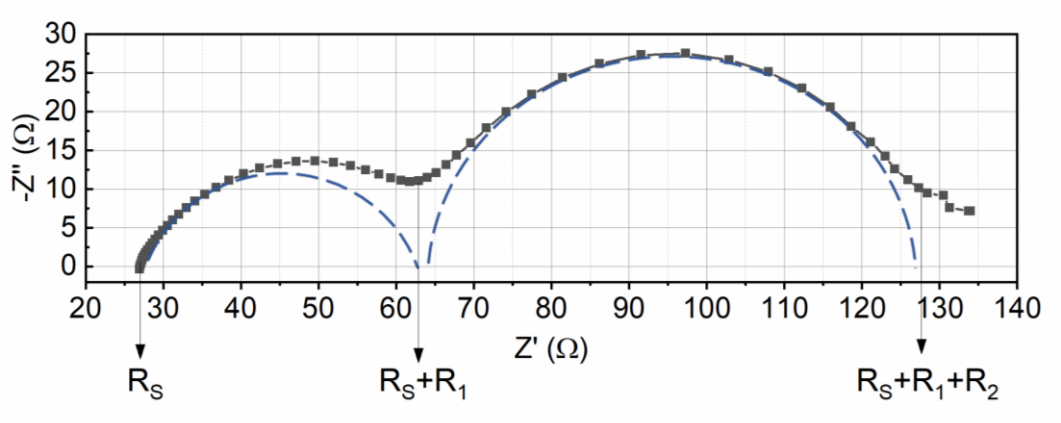


Figure 3.9. Example of a Nyquist plot of a DSSC with a TiO_2 photoanode. The mathematical fitting performed on these data is drawn with a dotted blue line.

Two different graphical representations can be obtained, namely the Nyquist plot and the Bode plot.[318–320] Nyquist plots, or Argand plots, are complex plane plots in which the imaginary impedance is plotted versus the real impedance, with isometric axes. These plots can be fitted by mathematical models to evaluate some parameters of the system, but this fitting can be misleading and must be used with caution and bearing in mind the physics behind the investigated system. An example of Nyquist plot of a dye-sensitized solar cell (DSSC) with a TiO_2 photoelectrode is reported in Figure 3.9.

At a first glance, it is possible to identify two different contributions in the response of the cell analyzed. In fact, each semicircle can be fitted by a RC parallel in the circuital model. In the case here presented the two semicircles represent the TiO_2 and the counter electrode contributions. The circuital representation of our system is proposed in Figure 3.10, where R_S is the series resistance of the system,

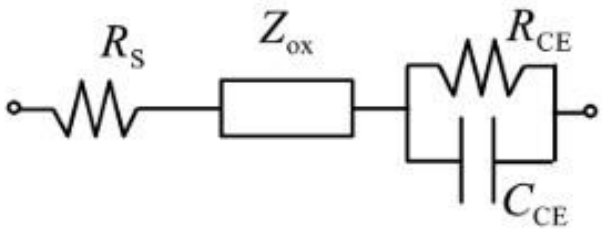


Figure 3.10. Possible circuital representation of the Nyquist plot of a DSSC with a TiO_2 photoanode.

Z_{ox} the impedance of the TiO_2 electrode and R_{CE} and C_{CE} the resistance and the capacitance of the counter electrode, respectively.

Bode plots instead explicitly display the frequency dependence and show $log|Z|$ and φ versus $log(f)$, oftentimes in a double-Y axis graph (see Figure 3.11). While Nyquist plots do not contain explicit information on the frequency, they are more accessible and easier to read at first glance. On the other hand, while more cryptical at first, the combination of the two possible Bode plots contain all necessary information to study the interfaces.

EIS analyses are performed at a single potential, usually the OCP of the cell to fulfill the linearity, causality, finiteness and stability hypotheses. However, several interesting information can be retrieved from a succession of EIS analyses performed at increasing potentials. These are called Mott-Schottky impedance measurements and are usually performed in the same potential window as the CV measurements. This kind of analysis is of particular importance when dealing with semiconductor electrodes as it allows for an investigation of the potential bending

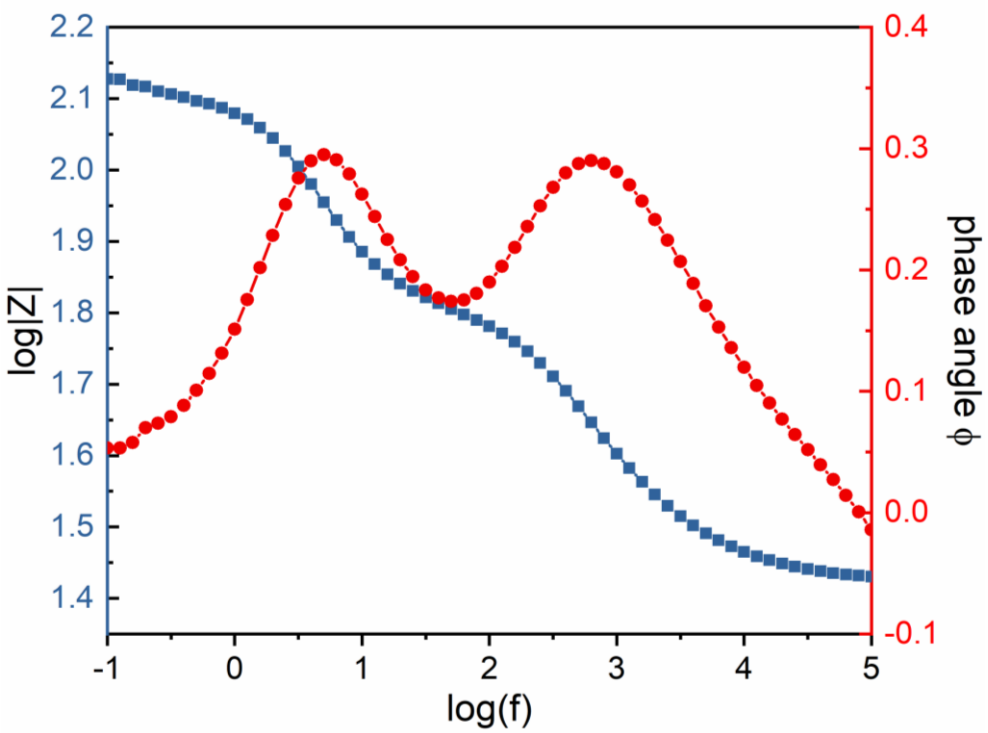


Figure 3.11. Bode plot of a DSSC with a TiO_2 photoanode.

at the surface and the determination of the flat band potential.[318] Under depletion conditions the superficial capacitance C_{SC} of the electrode is related to its flat band potential E_{FB} by means of Equation (3.18):

$$\frac{1}{C_{SC}^2} = \frac{2}{\varepsilon_0\, \varepsilon_r\, e\, N_D}\left(E - E_{FB} - \frac{kT}{e}\right) \tag{3.18}$$

where ε_0 is the vacuum dielectric permittivity, ε_r the dielectric constant of the semiconductor, N_D the mobile charge density, *k, T* and *e* have their usual meaning of Boltzmann constant, temperature and elemental charge, respectively. By plotting the evolution of the capacitance C_{SC}^{-2} as a function of the potential one can find the flat band potential as the intercept, whereas the mobile charge density is given by the slope.

In the following, EIS measurements were conducted on the nanotubes samples prior and successively to the cyclic voltammetries and other analyses to assess the cell parameters. An AC signal of 5 mV of amplitude was applied in the $[10^5:10^{-2}]$ Hz frequency range. Mott Schottky impedance measurements were also performed on the different nanotubes sample in the same potential window used for the CV analyses, with a 0.1 V potential step. As for the CV, the instrument resolution was kept at 100 µV throughout all measurements and the bandwidth was selected in accordance with the stability of the systems.

3.4.3. Other electrochemical analyses

When investigating the material properties, it is important to bear in mind the Butler-Volmer equation (Equation (3.19), which relates the current density to the overpotential:

$$j = j_0\left(exp\frac{\alpha_a nF\eta}{RT} - exp\frac{\alpha_c nF\eta}{RT}\right) \tag{3.19}$$

where j_0 is the exchange current density, η is the overpotential, $\alpha_a + \alpha_c = 1$ are namely the anodic and cathodic transfer coefficient and *n, F, R* and *T* have their usual meaning. By plotting $log(j_0)$ versus the overpotential, one obtains the so-called *Tafel plot*. The kinetics parameters α_a and α_c of the reaction investigated can be obtained by the slope of the linear ranges of the anodic and cathodic branches of the Tafel plot.

In the following experiments, Tafel plots were used to obtain the charge transfer coefficient for the nanotubes samples. After conditioning the cell to the OCP value for one hour, an overpotential of 0.1 V was reached with a scan rate of 100 $\mu V\ s^{-1}$ while recording the current over 50% of each step and with a resolution of 100 μV. The cell was then conditioned again to the OCP value for another hour and then taken to a -0.1 V overpotential value following the same parameters as before.

Chapter 4

Functionalized Graphene Oxide Membranes

In this chapter the results obtained for lithium extraction by means of pressure-assisted filtration on GO-based membranes will be presented.[163] At first, the optimization of the preparation of the membrane and its functionalization will be addressed. The actions undergone to optimize the experimental setup will then be provided, and finally the selectivity of the membrane will be proved.

4.1. Membrane preparation

The preparation of the membranes underwent several different optimization processes. First of all, following the procedure adapted from Sun et al.[135] and presented in section 3.1.1 the GO flakes were functionalized through carbodiimide esterification. The vacuum filtration setup illustrated in Figure 3.1 (a) was then employed to obtain the first membranes to test the stability of the flakes. To this end, 10 mg of f-GO were used for each membrane and an initial concentration of 0.2 mg mL^{-1} was chosen for the water dispersion. Unfortunately, the membrane thus obtained resulted fairly brittle and showed cracks and ridges when left drying on the support, as can be seen in Figure 4.1 (a).

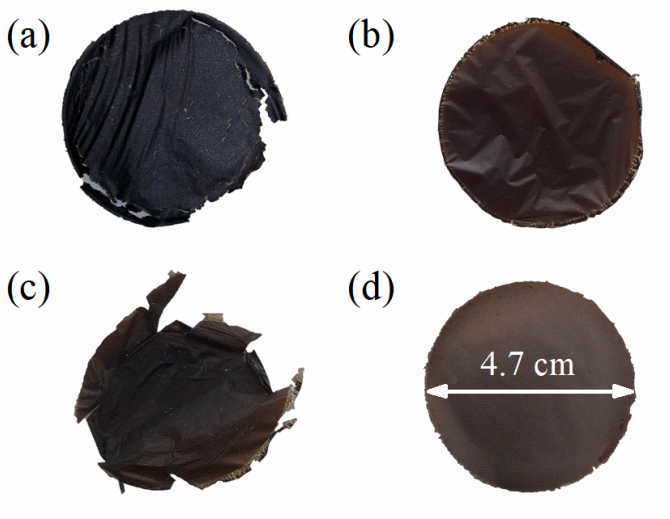


Figure 4.1. Pictures of the 10 mg membranes prepared. (a) f-GO, (b) f-GO + GO, (c) f-GO+PVDF, (d) f-GO+PVA. Adapted under the CC-BY license.[163] Copyright 2022, The Authors, published by MDPI.

The concentration of the water dispersion was then increased up to 1.0 mg mL^{-1}, following the work reported by Pedico et al.[141] The addition to the formulation of polymeric binders was also taken into consideration and three candidates were chosen based on their previous use as support material for water treatment applications.[167,321,322] A first trial was conducted by adding 40 wt.% pristine GO to the mixture (see Figure 4.1 (b)) to balance the partial reduction the GO flakes underwent during the functionalization. The resulting membrane showed a fairly good stability. A second option consisted in using PVDF, as the original work from which this formulation was taken used PVDF as the membrane main material. However, as can be seen in Figure 4.1 (c), the f-GO+PVDF membrane resulted to be the less stable of the three prepared and crumpled on itself. Finally, PVA was also tested in the same amount in light of its hydrophilicity,[119,167] and showed the best results in terms of mechanical stability (Figure 4.1 (d)). Furthermore the membrane resulted easily peelable from its support and when left in water for more than three months showed no signs of degradation.

The formulation of f-GO and 40 wt.% of PVA was thus chosen as the optimal one and tested for lithium recovery. All successive tests were performed on membranes prepared by pressure-assisted filtration in order to optimize the order degree of the stacked morphology.[155] Throughout all of the analyses, pristine GO and a f-GO membranes were used as references for the f-GO+PVA one. The weight

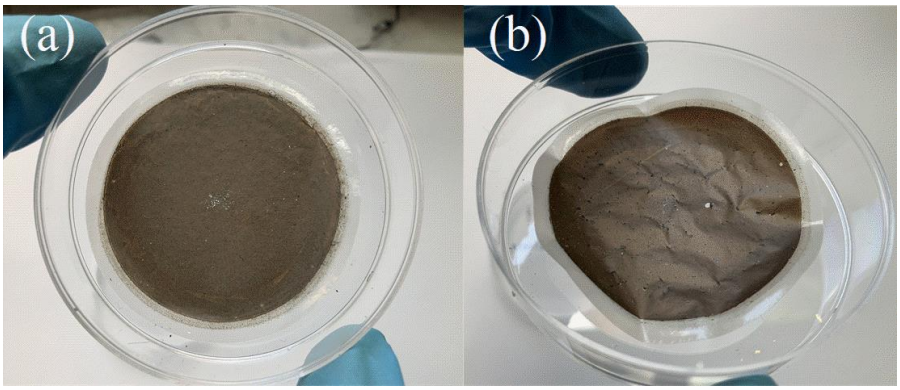


Figure 4.2. (a) Wet membrane and (b) dried membrane after continuing operations for several months.

of the membrane was also reduced to 3 mg for all successive analyses, following a previous work,[141] to optimize the flux. In this case the membranes were integral with the support and resulted reusable even after several months of operation and after drying in an open-air environment (see Figure 4.2).

The morphology of the prepared membranes was further investigated through scanning electron microscopy to assess whether the binder was homogeneously inserted among the GO flakes. The three cross sections of GO, f-GO and f-GO+PVA membranes are shown in Figure 4. (a), (b) and (c) respectively. The three membranes showed similar thicknesses and the typical highly stacked structure of GO membranes prepared by vacuum or pressure-assisted filtration. Furthermore no aggregates of binder were visible, thus indicating a good interaction between GO and PVA. A top view of the f-GO+PVA membrane is also displayed.

4.2 Characterizations

Since the filtration properties of highly stacked GO membranes are predominantly influenced by the dimension of the channels between the flakes, XRD measurements were performed on the three different membranes before the filtrations. The diffractograms obtained in the surroundings of the (001) diffraction peak of GO (around 10°) are displayed in Figure 4. (a). By applying Bragg's law, it can be seen that the average interlayer distance increases from an initial 7.6 Å of GO to 8.2 Å when GO had been functionalized and 8.9 Å when the polymeric binder was added. This in good accordance with what previously reported in the

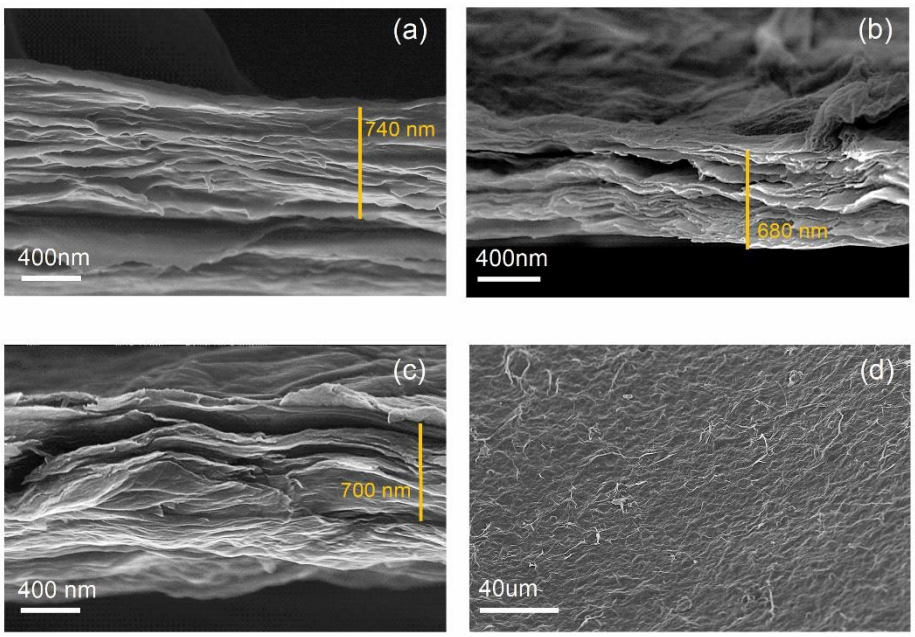


Figure 4.3. SEM micrographs of (a) GO, (b) f-GO, (c) f-GO+PVA membrane and (d) top view of the f-GO+PVA membrane after the filtrations. Adapted under the CC-BY license.[163] Copyright 2022, The Authors, published by MDPI.

literature about crown ethers acting as spacers between the GO flakes.[151] On a side note, the distances thus obtained should be taken as average interlayer distances since one should also consider the influence of its increase due to the humidity, and

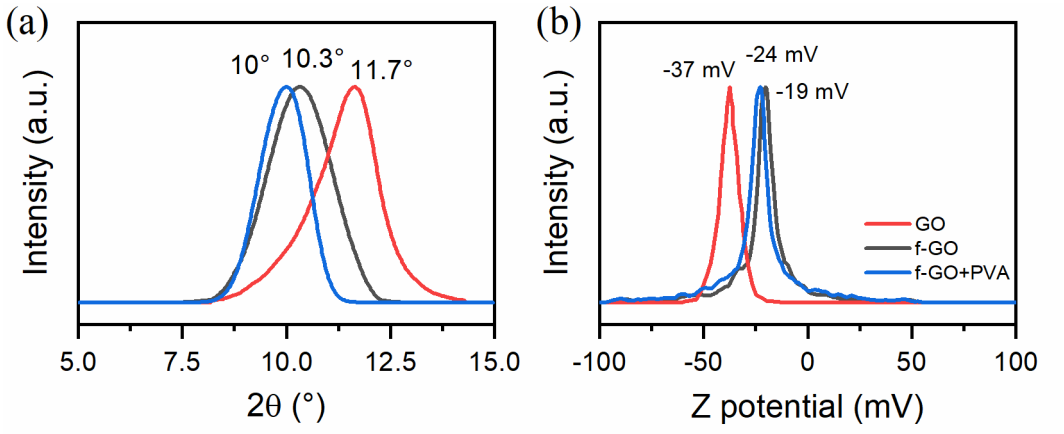


Figure 4.4. (a) XRD diffractograms and (b) Z-potential of GO (in red), f-GO (in black) and f-GO+PVA (in blue) membranes. Adapted under the CC-BY license.[163] Copyright 2022, The Authors, published by MDPI.

the thickness of the graphene oxide layer, which should balance each other out.[141,323]

The superficial charge of the membranes was also investigated by means of Z-potential measurements on the aqueous solutions of graphene oxide prior to the filtrations. The results of this analyses are shown in Figure 4. (b) and are in good agreement with the values reported in literature.[141,324] In particular, it is interesting to notice that while all three solutions maintain a negative charge, typical of GO, this charge decreases from an initial -37 mV of GO to -19 mV of f-GO and then slightly increases up to -24 mV when the binder is added.

The conservation of the graphitic structure of the GO flakes even after the partial reduction undergone during the functionalization was investigated through Raman spectroscopy (see Figure 4.3 (a)). It is possible to observe that the typical peaks of GO, the D peak and the G peak didn't change shape nor position after the functionalization. Indeed, they could be observed at 1324 and 1585 cm^{-1}, respectively. The signals from the Raman active modes of the functional groups, theoretically located between 1250 and 1300 cm^{-1},[128] instead, could not be appreciated because of an overlap with the signals from GO which are more intense.

The presence of the crown ether molecules was indeed confirmed by the FTIR analyses, displayed in Figure 4.3 (b). The peaks between 1100 cm^{-1} and 950 cm^{-1} are related to the O-C-O and C-O stretching vibrations of the aromatic rings and can be clearly seen in the spectrum of f-GO (in black).[119,128,129,135] The broad adsorption band corresponding to O-H stretching vibrations between 3000 and 3500 cm^{-1} could be appreciated in all samples, although the partial reduction of f-GO can be seen in the reduction of this signal between the red and black curves of Figure 4.3 (b). The other characteristic peaks of GO, the C=C vibrations at 1620 cm^{-1} and the C=O at 1720 cm^{-1} were also visible as was the adsorption peak of the C-H alkyl groups of PVA at 2940 cm^{-1} in the blue curve.[325]

Thermogravimetric analyses were also conducted on the different membranes (see Figure 4.3 (c) and Table 4.1.) and evidenced a reduction in the onset of the thermal degradation of the two membranes in which the GO was functionalized, probably due to the partial reduction the GO underwent during the functionalization process and the presence of more volatile molecules, such as the crown ethers. In the case of f-GO and f-GO+PVA, in fact, the DTG curve highlights how the thermal degradation starts at around 200 °C instead of 220 °C and the weight loss increases from 34% up to 44% (see Table 4.1.).

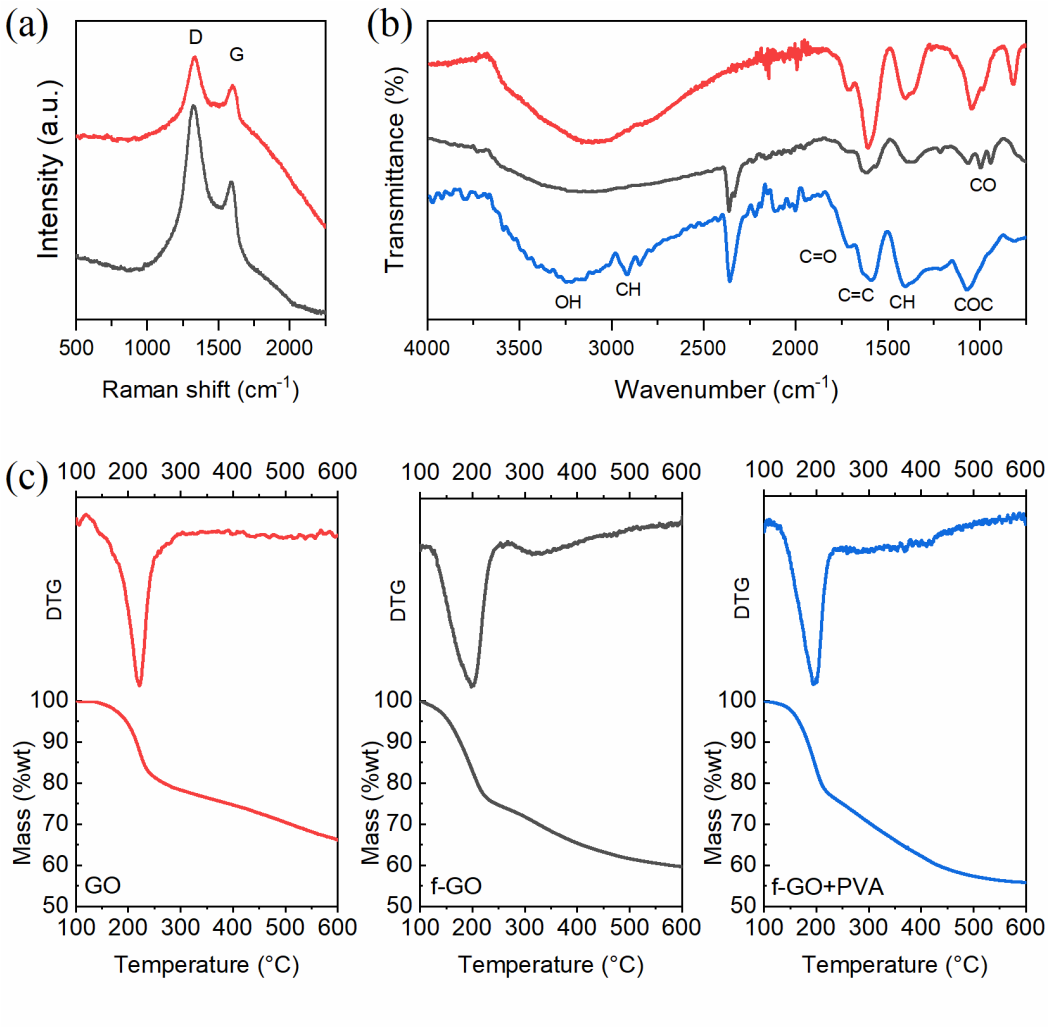


Figure 4.3. (a) Raman spectra, (b) FTIR spectra and (c) TGA and DTG curves of pure GO (in red), f-GO (in black) and f-GO+PVA (in blue) membranes. Adapted under the CC-BY license.[163] Copyright 2022, The Authors, published by MDPI.

Table 4.1 Characteristic values obtained from the thermos-gravimetrical analyses performed on the three membranes.

	GO	**f-GO**	**f-GO+PVA**
Thermal degradation onset	220 °C	198 °C	196 °C
Weight loss	34%	40%	44%

4.3 Filtrations

The experimental setup underwent several optimization in the course of the filtrations. The first one was the reduction of material used to prepare the membranes, which initially weighted 10 mg and were then reduced to 3 mg, as previously explained in section 4.1. A few immersion tests without any pressure applied were also conducted in the beginning. However these proved to be non-satisfactory and were discarded in favor of pressure assisted filtrations, which are in greater agreement with the stacked membrane morphology.

An initial run test was done under a pressure of 1 bar, however the pressure was then increased to optimize the flux conditions. The water flux of the functionalized membrane, showed indeed a peculiar non-linear relationship between the flux and the pressure applied and an operating pressure of 5 bar of nitrogen was chosen for the filtrations (see Figure 4.4).

After several trials and initial ICP mass measurements the optimized filtration protocol was determined to be five consecutive filtrations alternating the salt solution and the stripping solution, with a DIW wash of the chamber in between. The DIW wash was motivated by the fact that the hold-up volume of the dead-end

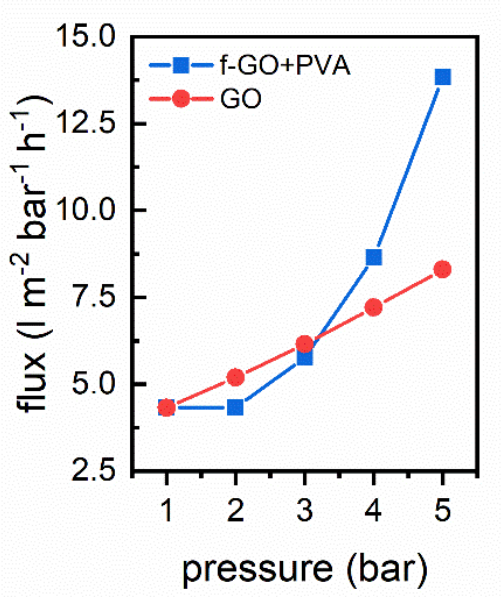


Figure 4.4. Permeability curves of GO (in red) and f-GO+PVA (in blue) membranes. Adapted under the CC-BY license.[163] Copyright 2022, The Authors, published by MDPI.

filtration setup, around 1 mL, caused contaminations which distorted the results of lithium uptakes. This was first noticed in abnormous standard deviations in the conductivity measurements of the solutions and then confirmed by ICP mass measurements which, although confirming the presence the lithium in the stripping solutions also evidenced inconsistencies in the uptakes, with relative standard deviations values up to ±35%.

The protocol was further improved by filtrating the same solutions for five filtration cycles, to test both the membranes recyclability and to achieve higher quantifiable amounts of recovered ions, since a quantification from such diluted streams could result problematic. Indeed, the concentration of all five chloride salts tested, the four already commercially extracted and lithium,[36] was 1 mM. This concentration was chosen as a compromise between the lithium concentration generally found in freshwater (ca. 0.17 mg L^{-1}) and the first stages of lithium enrichment operations.[121,326,327] The concentration of the acidic solution instead was chosen as 0.1 M as a compromise between a pH sufficiently low to correctly regenerate the crown ether molecules and a limited use of corrosive solutions.

As anticipated in section 2.2.3, *Membrane techniques and supramolecular systems*, the lithium adsorption mechanism of this system is composed of two different steps: a first one, during the salt filtration, in which lithium ions are immobilized into the crown ether molecules, and a second one where lithium ions are released into the acidic stripping solution. This system has been extensively studied in batch adsorption mode, however some studies report a successful application in flow conditions too.[151,165]

Conductivity measurements were conducted on all solutions at 25 °C under 100 rpm of magnetic stirring after their filtration step. An average over three measurements was performed for each step and a normalized delta of the conductivity increase between the first and last step of each cycle was computed. The choice of displaying only the normalized delta instead of the numerical values of conductivity rose from the need of properly comparing solutions with different starting conductivity and to highlight whether the exchange with the proton was taking place or not. The normalized delta was computed following Equation (4.1):

$$\frac{\Delta EC}{EC_{start}} = \frac{Conductivity\ after\ 5\ filtrations - Starting\ conductivity}{Starting\ conductivity} \qquad (4.1)$$

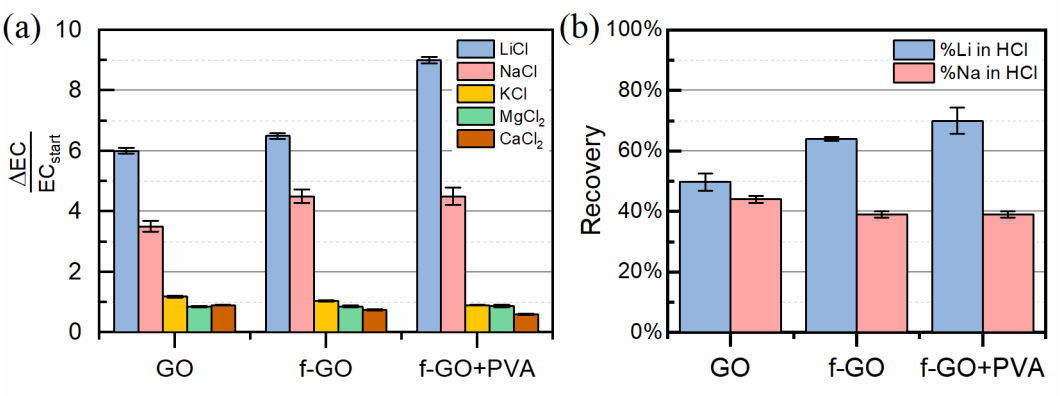


Figure 4.5. (a) Conductivity measurements (of the salt solutions) and (b) lithium and sodium recovery rates from ICP mass analyses (of the stripping solutions).

While the conductivity changes were computed for both the salt and the acid solutions, only the results of the salts are reported in Figure 4.5 (a). In light of the higher conductivity of the stripping solutions, both in relative and absolute terms, when the exchange H^+/Li^+ takes place, the salt solution conductivity should rise, whereas the one of the stripping should decrease. Since the variation should be more evident in the salt solution, this delta was chosen as the more representative one.

The ICP mass measurements, instead, were performed on the stripping solutions to quantify the amount of cations recovered after the filtrations. As can be seen in Figure 4.5 (b) those were performed only on the sets of solutions with lithium and sodium. Those were indeed the only filtration sets in which the conductivity measurements underwent a significant change, because the size of the cations could compete with the ring cavity. The recovery rate of lithium and sodium ions in the stripping solution was computed by means of Equation (4.2):

$$Recovery\ rate = \frac{Final\ stripping\ solution\ concentration}{Initial\ feed\ solution\ concentration} * 100 \qquad (4.2)$$

When looking at Figure 4.5 (b) it is possible to notice that when using the functionalized membranes, both the lithium uptake and the sodium rejection increase, confirming the selectivity of the system. The uptakes observable in the case of pristine GO membranes, 50% of lithium and 44% of sodium, could be the result of electrostatic bonding between the cations and the negative membrane, as resulted from the Z-potential measurements. Indeed, in this case the recovered

amount was pretty similar between the two cations. It is particularly interesting to notice that the presence of PVA in the membrane not only ensures better mechanical stability, but also results in a slight improvement of the selectivity of the membrane. Calculating the separation coefficient as the ratio between the recovery of both cations, the Li^+/Na^+ separation coefficient rises from 1.64 to 1.79, when the lithium recovery rate goes from 50% to 70% whereas the sodium one decreases to 39%.

Overall, 70% of the lithium initially present in the feed was recovered after five filtration cycles, with a total 24.5 $mg_{Li}\ g^{-1}_{membrane}$ and an average of 4.9 $mg_{Li}/g_{membrane}$ for each cycle when working with the f-GO+PVA membrane.[163] In order to draw a proper comparison with the other experimental results reported in the literature in similar systems, two figures of merit were chosen (see Figure 4.6): the uptake as a function of the feed solution and the uptake as a function of the time. Indeed, the high dispersity of this field in terms of feed and stripping solution compositions, operating parameters and technologies makes drawing fair comparisons a difficult task, as highlighted elsewhere.[64]

In this case the results were confronted with four studies in which a membrane functionalized with crown ether was used.[119,133–135] It can be easily seen that the membrane herein reported (indexed as a blue star in Figure 4.6) is fairly competitive with the literature works. Absolute values of uptakes would indicate lower performances with respect to the 27.1 $mg_{Li}\ g^{-1}_{membrane}$ reached by the PVDF membranes with the pDA adhesion layer of both Cui et al.[134] and Sun et al.[133] and the 97.23 $mg_{Li}\ g^{-1}_{membrane}$ reported by the spinned nanofibers of PVA and f-GO by Zheng et al.[119]

However, it must be noted that those values were reached while working with feeds twenty times and a hundred times more concentrated than the one here reported, which considerably facilitates adsorption. This can be easily seen when computing a recovery rate in percentages: whereas this membrane recovered 70% of the total lithium available, other works only reached values around 30%. Furthermore, while reaching very similar values of adsorption in similar feeds with the PVDF membrane with 20 wt.% of GO by Sun et al.,[135] our work reported the lowest eluent concentration, 0.1 M compared to 0.5 M to 1 M in the other works, hence minimizing the possible environmental impact, which was also considered when using DMSO instead of Dimethylformamide as a solvent for the preparation of the membranes. Overall, the membrane herein reported resulted to be an

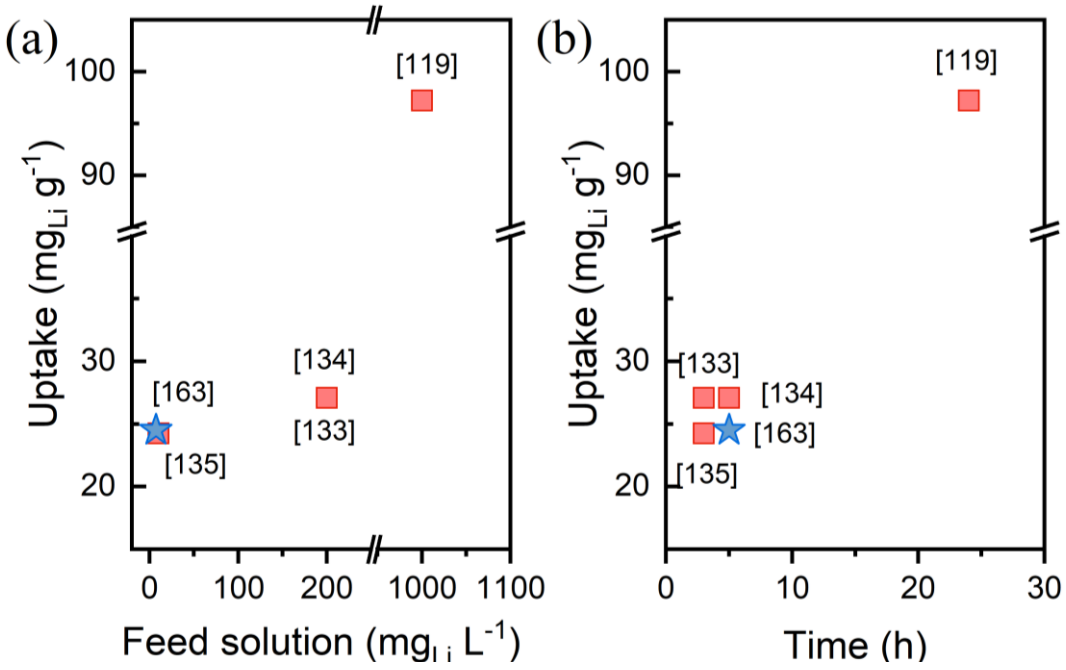


Figure 4.6. Comparison of the experimental data with other literature works, in terms of uptake as a function of (a) feed solution and (b) adsorption time. The experimental data of the lithium adsorption from the f-GO+PVA membrane are represented with blue stars.

excellent candidate for lithium recovery applications and further studies are now ongoing to assess the selectivity of this system in multi-cation solutions.

Chapter 5

Lithiated Titania Nanotubes

This Chapter will address all the results pertaining to lithium recovery by means of lithiated titania nanotubes. The anodic oxidation and subsequent optimization of the hydrothermal conversion treatment will be presented together with the study on the evolution of the morphology. The electrochemical characterizations and will then be divided in two different sections depending on the electrolyte in which they were performed. A deep analysis of their properties evolution throughout the characterizations will be presented, then the stability of this structure in the different environment will be addressed.[308]

5.1 Optimization of hydrothermal conversion parameters

Titania nanotubes were grown by anodic oxidation as explained in section 3.2.1, *Anodic oxidation*. As previously stated when first describing the anodic oxidation technique, several parameters need to be finely tuned to grow suitable nanotubes. Among them, the applied voltage, anodization time and electrolyte composition are worth-mentioning. For these experiments, an ethylene glycol electrolyte was used, with low concentrations of both water and fluoride ions. This composition was chosen following previous works to obtain an hexagonal morphology and smooth tube walls.[309,328] Furthermore a potential of 60 V was applied for 15 minutes in order to obtain tubes of 80-100 nm of diameter and ca. 7 μm of length. Nanotubes grown by anodic oxidation are spontaneously amorphous, hence a thermal

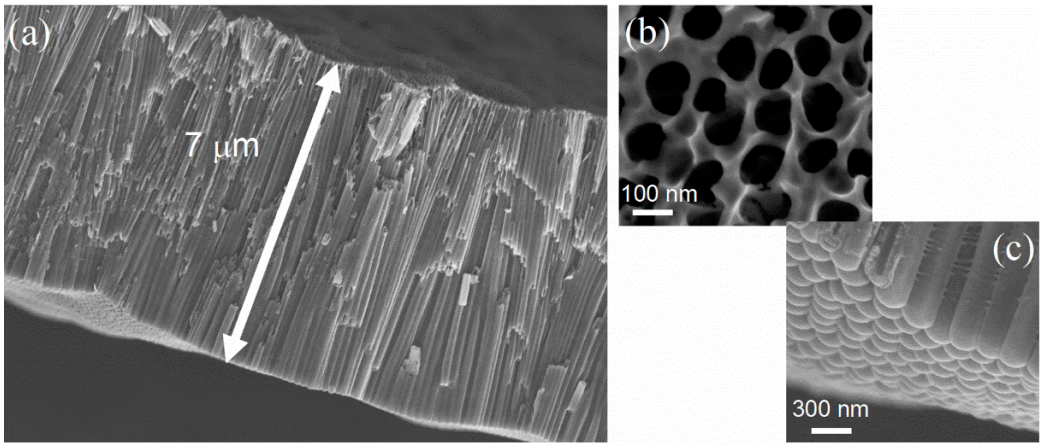


Figure 5.1. SEM micrographs of TiO_2 anatase nanotubes. (a) cross-section of the NTs, (b) inset of the top view, (c) inset of the bottom view. Adapted under the CC-BY license.[308] Copyright 2022, The Authors, published by Wiley-VCH.

annealing step at 450 °C for 30 minutes was performed in order to convert them into the anatase phase. The morphology of the resulting nanotubes can be seen in Figure 5.1, where a cross-section and insets of the top and bottom of the tubes are reported. Anatase samples were kept as reference for all successive characterizations.

Hydrothermal conversion of anatase NTs into lithium spinel or titanates was attempted adapting the procedure previously reported for barium titanate.[289,290] Several parameters were taken into consideration, namely the temperature, the LiOH concentration and the starting TiO_2 phase. Fixing the time of thermal treatment at two hours, three temperatures, i.e. 120 °C, 150 °C and 200 °C, and four different concentrations were chosen, from 0.25 M to 1 M with 0.25 M intervals.

A first trial at 120 °C with the four different LiOH concentrations was first conducted. As can be seen in the diffractograms reported in Figure 5.2, the conversion was unsuccessful at 0.25 M and only partially achieved at 0.5 M. Indeed, no peaks of the mixed oxide can be appreciated at 0.25 M and all the typical peaks of anatase are still quite strong such as the characteristic (101) peak at 25°, indexed with stars. A typical morphology in the case of unsuccessful conversion is displayed in Figure 5.2 (b), where the morphology of the anatase nanotubes remains unchanged as their composition and crystallography. However, at higher concentrations, it is possible to see that the anatase peak at 25° fades while a characteristic peak at 43.3° appears. This peak, indexed with circles, is peculiar to the mixed oxide phase and therefore signals a successful conversion. However, at

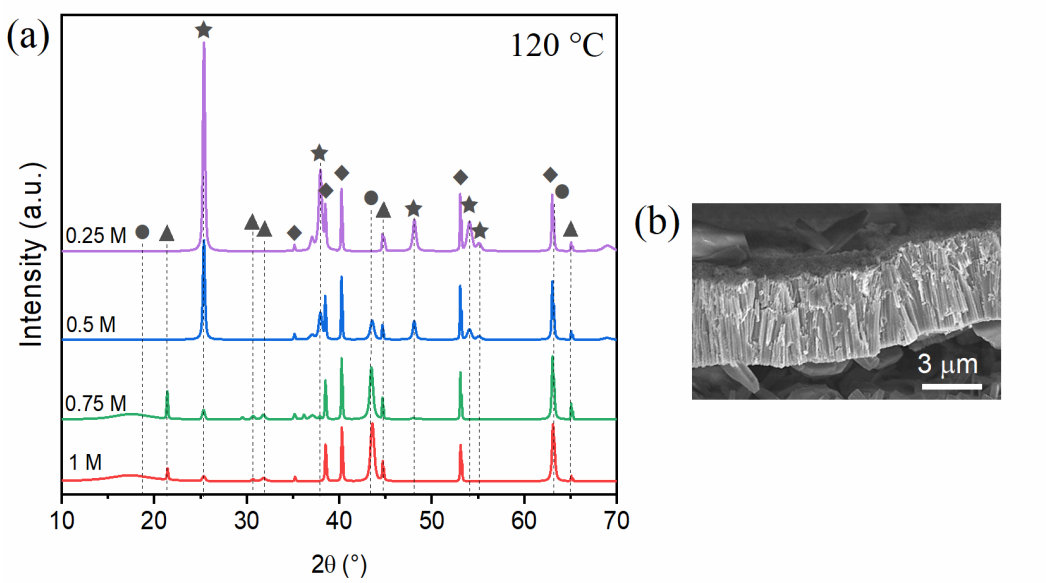


Figure 5.2. (a) XRD diffractograms of the anatase samples treated at 120 °C for 2 hours at different LiOH concentrations; (b) SEM micrograph of a sample unsuccessfully converted into $LiTiO_x$. Stars indicate the anatase phase, circles the lithium-titanium oxide, triangles the carbonates and rhombuses the titanium foil underneath. Adapted under the CC-BY license.[308] Copyright 2022, The Authors, published by Wiley-VCH.

such low temperatures, carbonates also form as by-products, as evidenced by the presence of the peaks indexed with triangles at around 21°, 31° and 45°.

A different situation is encountered when treating the samples at 150 °C. As can be seen in Figure 5.3 most of the conversions were successful, except for 0.25 M, and less carbonates were present, except for the sample treated with 0.75 M LiOH. This is confirmed by the presence of the well-defined characteristic peaks of the mixed oxide at 43.3°. However, as can be seen in the micrograph reported in Figure 5.3 (b), while the conversion was successful from a crystallographic point of view the morphology was not completely maintained. It is possible to see that the nanotubes partially collapsed in a thinner and more compact layer, with a more particle-like morphology than tubular.

Conversely, when treating the samples at 200 °C all concentrations proved to lead to successful conversion, both from a crystallographic and morphological point of view. As can be seen in Figure 5.4 (a), all samples thus treated showed the characteristic 43.3° peak of the mixed oxide as well as a broad peak at around 18°, whereas the 25° anatase peak was mostly absent or just hinted. The conversion appears to be fairly repeatable and could be indexed with a cubic Li:Ti spinel phase.

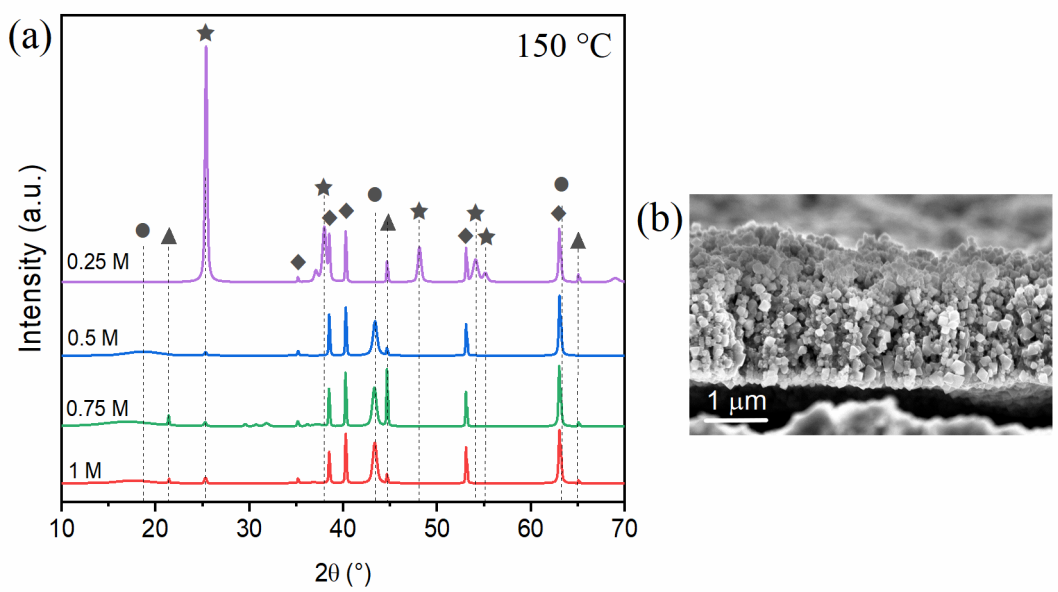


Figure 5.3. (a) XRD diffractograms of the anatase samples treated at 150 °C for 2 hours at different LiOH concentrations; (b) SEM micrograph of a sample crystallographically converted into $LiTiO_x$ but where the morphology was not conserved. Stars indicate the anatase phase, circles the lithium-titanium oxide, triangles the carbonates and rhombuses the titanium foil underneath. Adapted under the CC-BY license.[308] Copyright 2022, The Authors, published by Wiley-VCH.

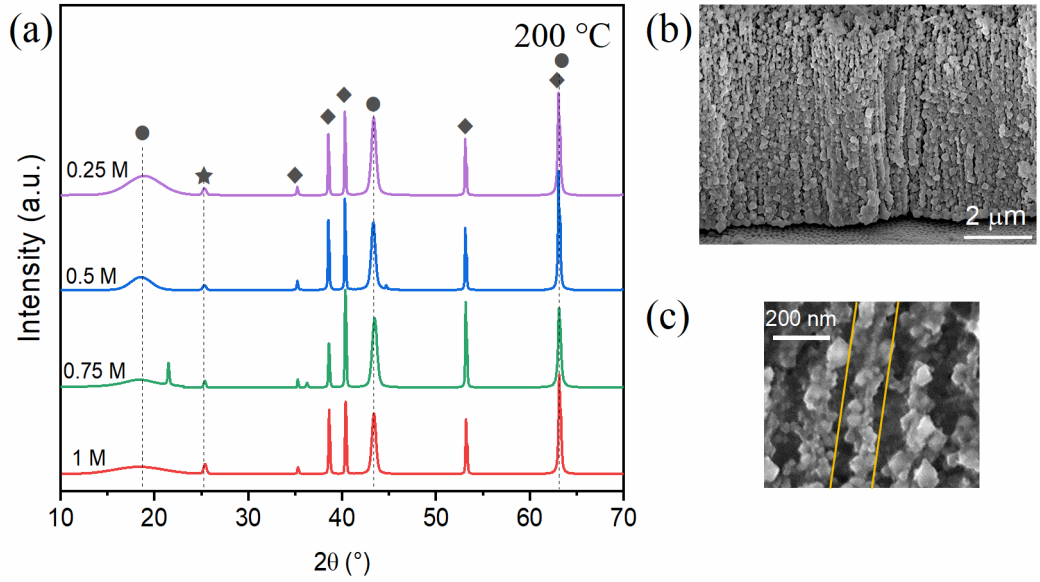


Figure 5.4. (a) XRD diffractograms of the anatase samples treated at 200 °C for 2 hours at different LiOH concentrations; (b) SEM micrographs of a sample successfully converted into $LiTiO_x$ with (c) inset of the tubular morphology. Stars indicate the anatase phase, circles the lithium-titanium oxide, triangles the carbonates and rhombuses the titanium foil underneath. Adapted under the CC-BY license.[308] Copyright 2022, The Authors, published by Wiley-VCH.

A particular morphology was also reached, as the cross section of Figure 5.4 (b) and the inset of Figure 5.4 (c) display. While the tubular morphology was maintained, the smooth walls left their place to rough particle-like structures protruding from the tubes themselves.

By combining the results obtained by morphological and crystallographic characterizations, the optimal conditions to perform the hydrothermal conversion treatment of the anatase samples were deemed to be 2 hours at 200 °C on 0.25 M LiOH. Indeed this combination of parameters allowed one to minimize the concentration of the basic solution. A focus of the various treatments performed with this same concentration is displayed in Figure 5.5, where a trial performed with amorphous titania nanotubes, labelled *am*, is also reported. Indeed, when trying to convert titania nanotubes into barium titanate, the conversion only turned out successful when starting from amorphous nanotubes.[289] This was not the case when working with lithium, as extensively proved by the results herein reported, although from the asymmetricity of the peak and its broadness the mixed oxide

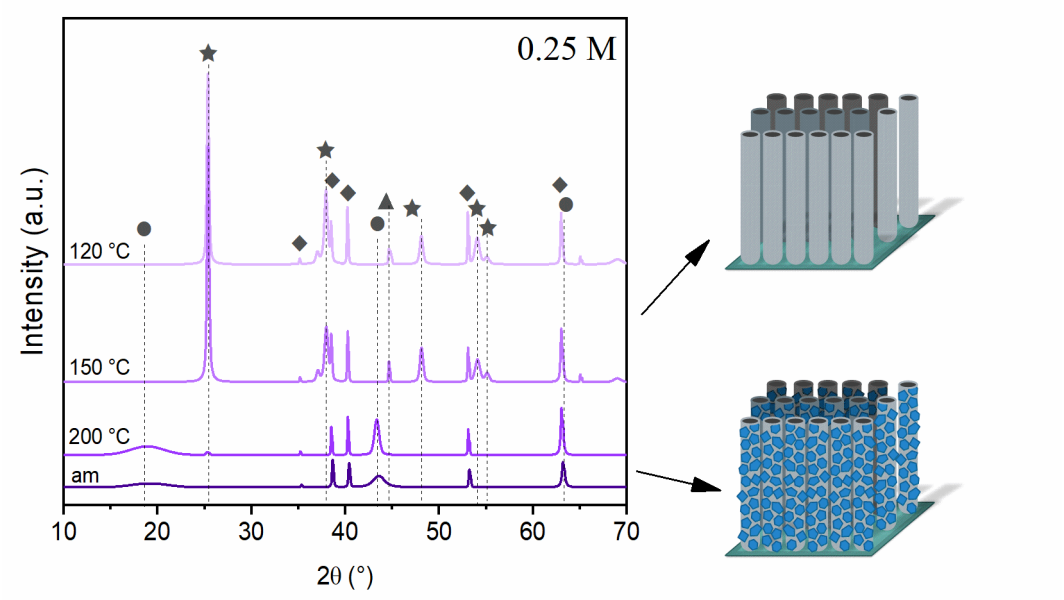


Figure 5.5. XRD diffractograms of the anatase and amorphous samples treated at different temperatures for 2 hours in 0.25 M LiOH, with schematic representations of successful (bottom) and unsuccessful (top) conversions. Stars indicate the anatase phase, circles the lithium-titanium oxide, triangles the carbonates and rhombuses the titanium foil underneath. Adapted under the CC-BY license.[308] Copyright 2022, The Authors, published by Wiley-VCH.

would present itself in a less ordered phase. Furthermore, since amorphous titania nanotube spontaneously convert into anatase in aqueous solutions, starting from anatase samples was deemed the best operating choice. [310,329] Figure 5.5 also shows some schematic drawings of the two structures of pristine titania and $LiTiO_x$ nanotubes, which will be further used to exemplify the structure under examination.

Finally, a summary table of all the combinations of temperature and LiOH concentrations attempted to convert titania nanotubes into mixed lithium oxides is reported in Table 5.1.

Table 5.1. Summary of the outcomes of the different conversion parameters combinations

	0.25 M	**0.5 M**	**0.75 M**	**1 M**
120°C	no conversion	conversion incomplete, carbonates	conversion almost complete, carbonates	conversion almost complete, carbonates
150°C	no conversion	conversion almost complete, carbonates	conversion almost complete, carbonates	conversion almost complete, carbonates
200°C	conversion complete	conversion complete	conversion complete, some carbonates	conversion complete

5.2 Electrochemical characterizations in organic electrolyte

As previously stated, the suitability of $LiTiO_x$ electrodes for lithium intercalation was first tested in organic electrolyte to only focus on the lithium ion diffusion. To assess the storage properties of the electrodes, compositional characterizations were performed before and after their electrochemical cycling. In the following the results of cyclic voltammetries, potentiostatic and sequential electrochemical impedance spectroscopy, potentio-dynamic and XPS analyses are reported.

At first, the possibility of lithium ion insertion in the structures under analysis was investigated. To this mean, three different sets of electrodes were tested in

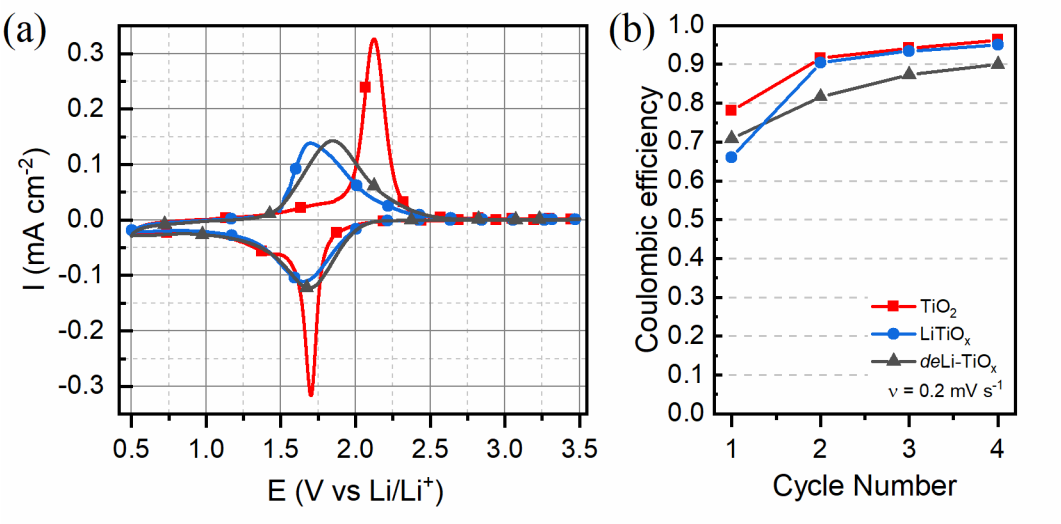


Figure 5.6. (a) Cyclic voltammograms of TiO_2, $LiTiO_x$ and *de*Li-TiO_x electrodes in organic electrolyte and (b) Coulombic efficiencies of the scans at 0.2 mV s^{-1}.

organic electrolyte: anatase TiO_2, $LiTiO_x$ and *de*Li-TiO_x, which will be further discussed in section 5.3.1, *De-lithiation mechanism*. The last cyclic voltammogram in $LiPF_6$ 1 M in EC:DMC 1:1 at 0.2 mV s^{-1} of each electrode can be seen in Figure 5.6. After the first cycles it is indeed reasonable to believe the solid electrolyte interface (SEI) was formed and the interface can therefore be considered stable, as evidenced by the coulombic efficiency reaching stable values (see Figure 5.6 (b)). The color code used in this figure will be maintained throughout the whole chapter when plotting characterization of the three electrodes: anatase will be always displayed in red, $LiTiO_x$ in blue and *de*Li-TiO_x in black.

Focusing first on the anatase sample, it can be seen that the voltammogram presents the classic shape of a battery-like material, with very sharp peaks due to the highly ordered structure. Furthermore, while presenting a first couple of primary peaks at about 1.70 V/2.10 V, responsible for the transition from lithium-poor Li_xTiO_2 phase to the titanate one, it also shows a secondary couple at about 1.41 V/1.74 V which is well-known in the literature as the one indicating a second phase transition from the titanate to the fully lithiated phase. [233,270,330]

The lithiated and de-lithiated nanotubes, instead, show a voltammogram with broader peaks, as a result of a partial loss of order after the hydrothermal conversion, and most of all closer peaks. This indicated that the insertion/disinsertion of lithium ions in this kind of structures is a more reversible

process, as evidenced by the difference between the two peaks < 59 mV in the lithiated samples. It should also be noted that while the insertion peak of lithium is at a similar potential in all three structures, the de-lithiation one greatly differs. However, it is compatible with the secondary de-lithiation peak reported for anatase, which is usually attributed to the de-lithiation from the fully lithiated phase to the titanate phase. Although the lithiated samples could not be univocally indexed with a stoichiometric compound, they present several properties close to the titanate class, which could explain this de-lithiation potential. Further information on the specifics data of the three electrodes can be found in Table 5.2.

Cyclic voltammetries at increasing scan rates were also used to investigate the kinetic behavior of the electrodes. To this mean two different scan rate spacings were chosen over two decades (from 0.2 mV s^{-1} to 200 mV s^{-1}), an equidistant on a linear scale and an equidistant on a square-root scale. Indeed, as anticipated in section 3.4.1, *Voltammetry techniques*, a relationship exists between the absolute value of current peaks and the scan rate applied. The cases of a linear relationship with linearly spaced and squared-rooted spaced scan rates represent the two limiting cases of surface-limited and diffusion limited processes. As can be seen in Figure 5.7 where the cathodic peak currents are plotted as a function of the square root of

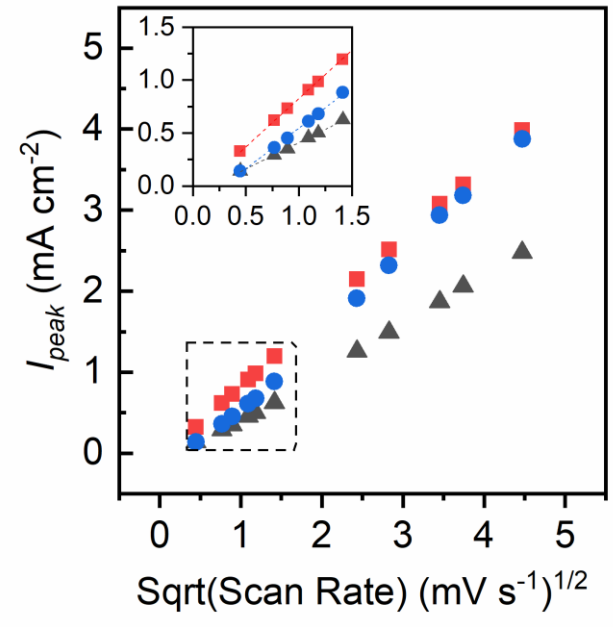


Figure 5.7. Cathodic peak current densities as a function of the square root of the applied scan rates in the electrochemical reversibility range. All linear fittings present a value of R^2>0.9985.

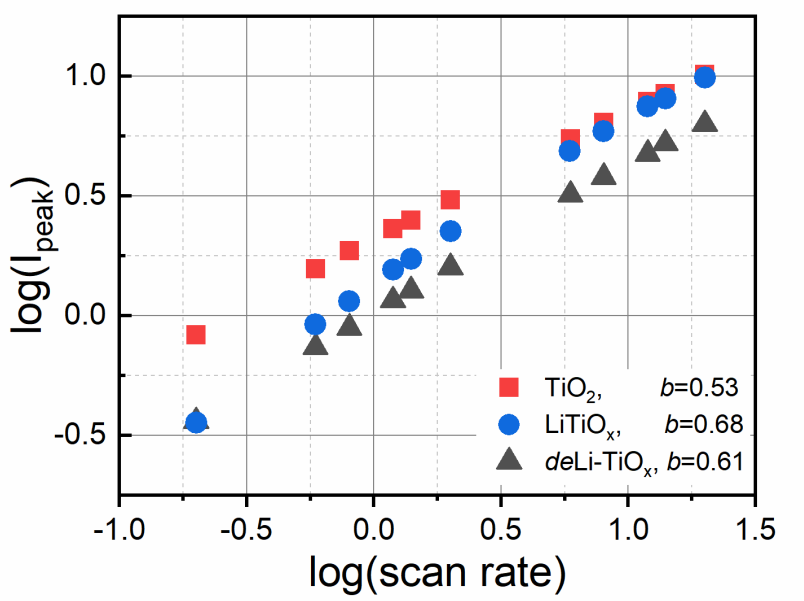


Figure 5.8. *b-value* graphs of the cathodic peak currents of the three electrodes analyzed.

the scan rates, all three electrodes appear to be mainly diffusion-controlled. Indeed all three linear relationships present R^2 values higher than 0.9985. It must be noted that not all scan rates were considered in this case, but only those in the electrochemical reversibility range were taken into consideration. This choice was motivated by the fact that the electrodes herein considered were solid electrodes without any additional additive and therefore can show high ohmic losses at higher scan rates, which could be misleading in this kind of graphs. This diffusion-controlled behavior is different from what previously reported in literature where anodically grown anatase nanotubes, TiO_2-B and hydrogen titanate nanostructures showed predominantly pseudo-capacitive behavior.[234,331–333]

To further investigate this difference from what previously reported, *b-value* calculations were also performed on the three data sets from the cyclic voltammetries, see Figure 5.8. This was also performed in light of the fact that the previous analysis only considered the peak value and not its dispersity, and the three samples presented fairly different shapes of the peaks. *b-values* were calculated for all electrodes and while in the case of anatase NTs the value of 0.53 was confirmed, slightly higher values of 0.68 and 0.61 were found for $LiTiO_x$ and *de*Li-TiO_x respectively. However, the purely capacitive component of the current had not been subtracted because of the shape of the voltammograms did not allow for an easy determination of this contribution.

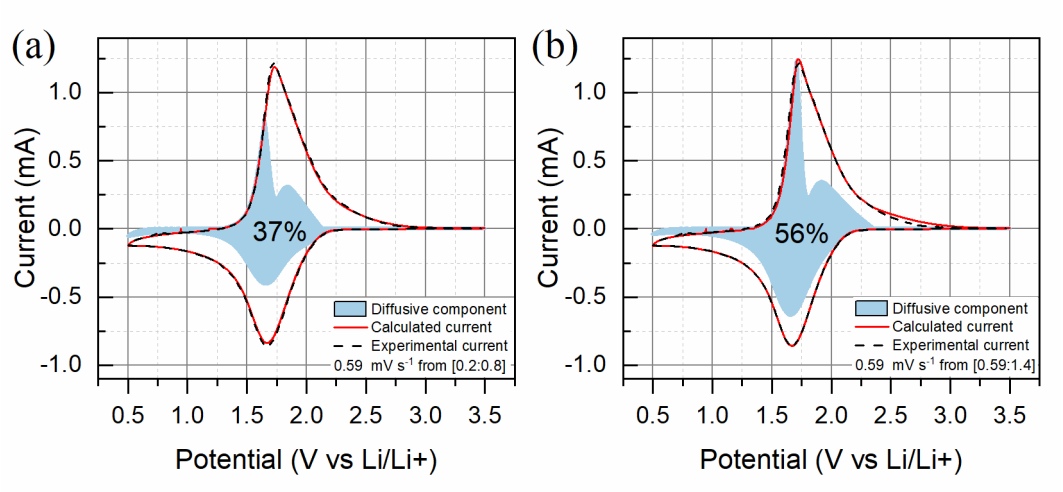


Figure 5.9. Deconvolution of the current into diffusive and capacitive components by applying the Dunn method on the 0.59 mV s^{-1} voltammograms in the (a) 0.2 mV s^{-1} to 0.8 mV s^{-1} and (b) 0.59 mV s^{-1} to 1.4 mV s^{-1} ranges.

A tentative attempt to discern the capacitive and diffusive components of the current was performed trying to apply Dunn's methodology to the lithiated electrodes, which presented the highest *b-value*. To this end, the voltammograms at low scan rates, lower than 1.5 mV s^{-1} were employed to deconvolute the two contributions. However, this calculation proved to be mostly unreliable for these electrodes, probably in light of the tortuosity of the lithiated samples which makes them less suitable for this kind of analysis. An example of the results obtained for 0.59 mV s^{-1} is reported in Figure 5.9. It is possible to see that two quite different deconvolutions were obtained for the same voltammogram using a slightly different set of voltammograms. Furthermore, while the shape of the diffusive component remains the same in one case it is the predominant component, as could be presumed by the previous analyses that indicated a process predominantly diffusion controlled, whereas in the other it is only a small percentage of the total current.

In light of these contrasting results, but with a tendency towards diffusion-controlled processes, these electrodes will be henceforth considered controlled by diffusion processes. The difficulties encountered in properly analyzing these results could derive from the fact that these electrodes present an *anomalous diffusion*. Indeed the data of electrochemical impedance spectroscopy of these electrodes were found to fit a modified Bisquert model adapted for porous electrodes.[334] In the case of anomalous diffusion, in fact, the general continuity equation should be

rewritten as a time-fractional equation.[335] In the case of these electrodes this coefficient was found to be equal to 0.9, demonstrating a sub-diffusive behavior.

Assuming a diffusive behavior, a calculation of the diffusion coefficient of lithium ion into the lithiated nanotubes was attempted by using Randles-Ševčik equation (3.7). To do so, at first the results of the cyclic voltammetries at increasing scan rates were used. The ratio between the slopes of the linear fittings of the anodic and cathodic peaks versus the square root of the scan rates were calculated and following equation (3.10) a first estimation of the transport coefficients was obtained.

The transport coefficients were also independently calculated from the Tafel plot reported in Figure 5.10. Several potentio-dynamic analyses were performed at different scan rates and with different percentages of current integrated in order to reduce the capacitive component of the current. The measurements consisted of a first potentiostatic conditioning of the cell followed by a potentio-dynamic step in the polarization window of ±100 mV. The integrated current percentage was varied between 10% and 100% with 10% steps, and the scan rates were varied between 500 μV s^{-1} and 10 mV s^{-1}. However, these changes did not alter the shape nor the slope of the two branches significantly, showing again that the capacitive

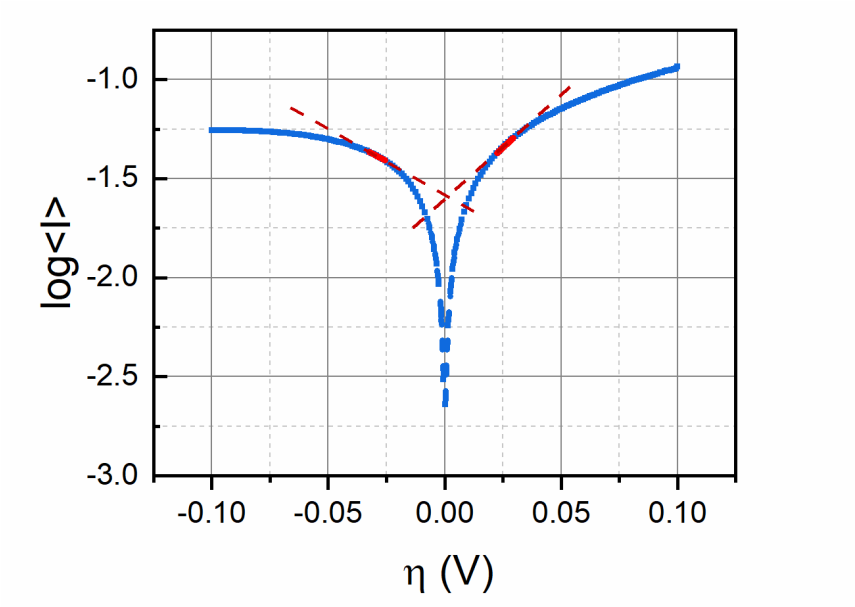


Figure 5.10. Tafel plot of the lithiated electrodes with 50% of the current integrated at 100 μV s^{-1}.

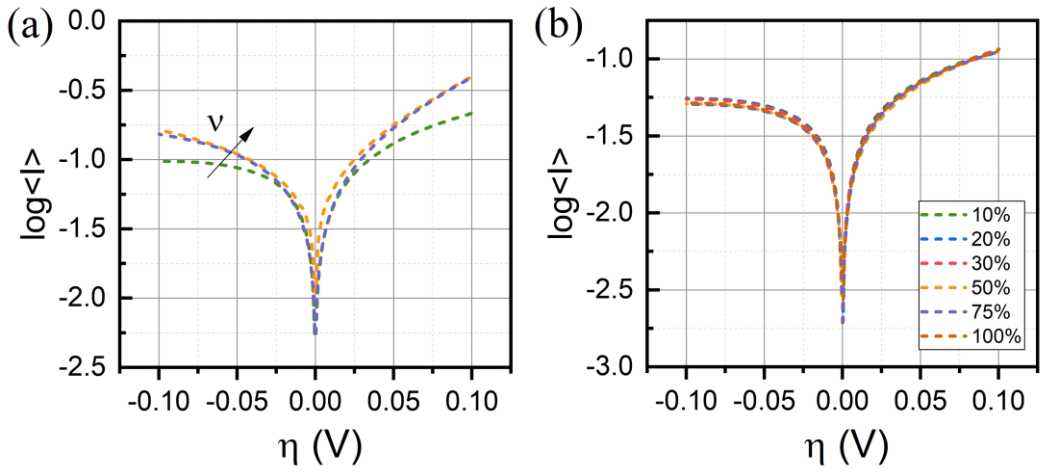


Figure 5.11. Tafel plots of the lithiated electrodes performed at (a) different scan rates with 50% off current integrated and (b) different % of integrated current at 100 μV s^{-1}.

component of the current can be considered negligible for these electrodes. As can be easily seen in Figure 5.11, while increasing the integrated current had no effect on the curves, the increasing of the scan rate only affected the plateau at the edges of the polarization window which is not useful for this kind of calculations, while the slope of the interpolated region remained fairly constant (only a shift to higher currents can be seen).

By extrapolating the slope of the linear region of each branch (highlighted in red in Figure 5.10) and following Butler-Volmer Equation (3.19) one can find the reduction and oxidation charge transfer coefficients to be 0.36 and 0.64, respectively. As previously stated, by acquiring Tafel plots at different scan rates, it was also possible to see that the charge transfer coefficient could be mostly considered independent from the scan rates, as the values obtained were almost the same with scan rates spanning over two decades. In particular, the charge transfer coefficient values obtained from the Tafel plot performed at 10 mV s^{-1} were 0.38 and 0.62 for the reduction and the oxidation branches, respectively.

The seemingly acceptable accordance between these two separate calculations allowed to conclude that the obtained value of the charge transfer coefficient could be considered reliable. The diffusion coefficient was then calculated as follows. Since for these electrodes, the cyclic voltammetries appeared to be irreversible reactions, as can be seen in Figure 5.12, where the voltage peaks appear to be

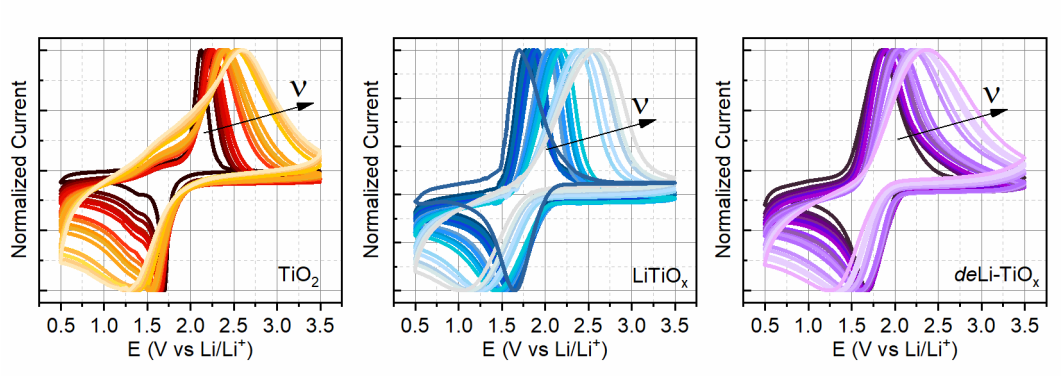


Figure 5.12. Normalized cyclic voltammetries of TiO_2, $LiTiO_x$ and *de*Li-TiO_x electrodes with scan rates spanning from 0.2 mV s^{-1} to 200 mV s^{-1}.

dependent from the scan rate,[312] the rearranged version from equation (3.8) was used.

Inserting the slope of the graph of the current peak (in A) versus the square root of the scan rate (in V s^{-1}), α=0.64 and C_0 = 1 M = 10^3 mol m^{-3}, one should only define the area of the electrode to obtain the diffusion coefficient. Two different routes were here employed, with a first considering the geometrical area of the electrode and a second one where an estimation of the real superficial area of the porous electrode was attempted. Considering the geometrical area of 2.54 cm^2, the diffusion coefficient resulted to be equal to $1.165*10^{-8}$ cm^2 s^{-1}. This value was reduced of almost an order of magnitude to $1.57*10^{-9}$ cm^2 s^{-1} when considering the estimated superficial area. The superficial area was estimated following equation (3.11), where the capacitance value was obtained from the high frequency slope of the logarithmic Nyquist plot. The Debye length was calculated according to equation (3.12) and resulted equal to $3.43*10^{-10}$ m, using a dielectric constant equal to 50.[229] The superficial area was then estimated to be around 6.9 cm^2. An estimation of the diffusion coefficient of TiO_2 and *de*Li-TiO_x was also calculated by means of equations (3.8) and (3.10). The results are reported along with the other characteristics of the electrodes in Table 5.2. It is possible to notice that the lithiated and delithiated samples present lower diffusion coefficients than the more ordered TiO_2 structure but still the lithiated samples are of the same order of magnitude.

Mott-Schottky analyses were performed on the three kind of electrodes to assess their flat bland potential and carrier density (referred to the geometrical area), following equation (3.18). The dielectric constant was assumed equal to 50 for all three electrodes, as previously stated.[229] Flat band potentials were estimated from

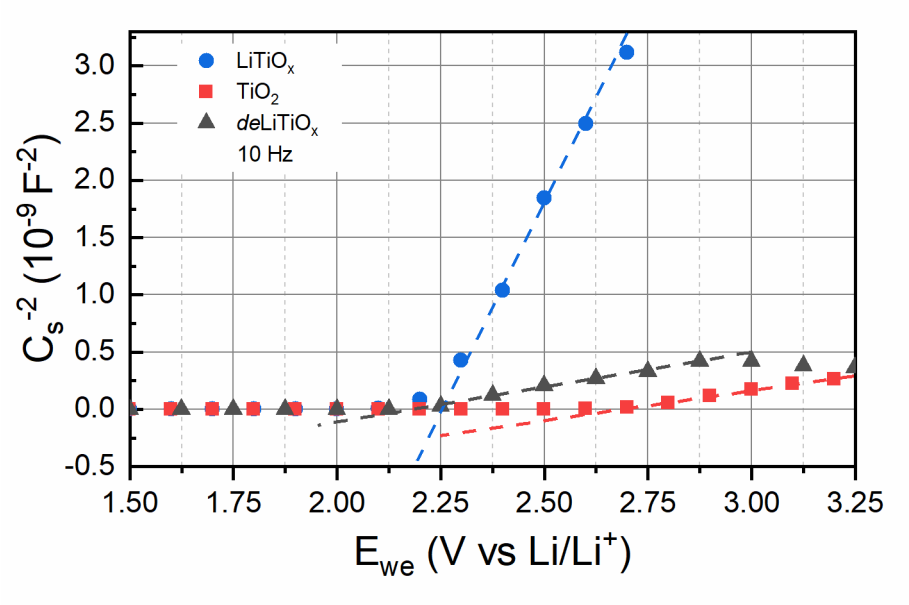


Figure 5.13. Mott-Schottky plots of TiO_2, $LiTiO_x$ and deLi-TiO_x electrodes at 10 Hz. The potential window was restricted to focus on the region near the intercept of the linear fitting.

the intercept of the linear fittings of the curves at 10 Hz while the carrier density was obtained applying equation (3.18) on the slopes of the linear fittings. As can be seen in Figure 5.13 and in the data reported in Table 5.2, the delithiated electrodes present intermediates values of carrier density between the other two electrodes, as could be seen from the slope. However it presents a very close flat band potential to the lithiated samples. The delithiated samples represent therefore a close intermediate solutions between the anatase and the lithiated samples.

Table 5.2. Summary of the electrochemical properties of the TiO_2-based electrodes in organic electrolyte at 0.2 mV s^{-1}. V_{red} and V_{ox} represent the potentials of the reduction and oxidation peaks, Q_{red} and Q_{ox} the specific capacities in reduction and oxidation, $\eta_{coulombic}$ the coulombic efficiency, α the charge transfer coefficient, *D* the diffusion coefficient, E_{fb} and n the flat band potential and the charge density.

	TiO_2	**$LiTiO_x$**	***de*Li-TiO_x**
V_{red} (V)	1.70	1.65	1.68
Q_{red} (mAh cm^{-2})	0.120	0.100	0.116
V_{ox} (V)	2.12	1.69	1.85
$\eta_{coulombic}$	0.95	0.96	0.90

Q_{ox} (mAh cm^{-2})	0.114	0.096	0.105
α	0.52	0.64	0.55
D **(cm^2 s^{-1})**	2.098 * 10^{-8}	1.165 * 10^{-8}	5.753 * 10^{-9}
E_{fb} (V)	2.67	2.24	2.20
n (cm^{-3})	5.56 * 10^{19}	3.78 * 10^{18}	4.56 * 10^{19}

XRD analyses were performed on all samples before and after the electrochemical characterizations. By looking at Figure 5.14 it is possible to see that the TiO_2 anatase NTs underwent no crystallographic change during their use. In particular, although lithium could be well inserted in and removed from the structure during the cycling, no lithium was left stored into it at the end of the characterization. This could be interpreted as a possible use of this structure as electrodes in energy storage (batteries and/or capacitors) but not as electrodes for lithium recovery applications. Contrarily, the lithiated samples present some

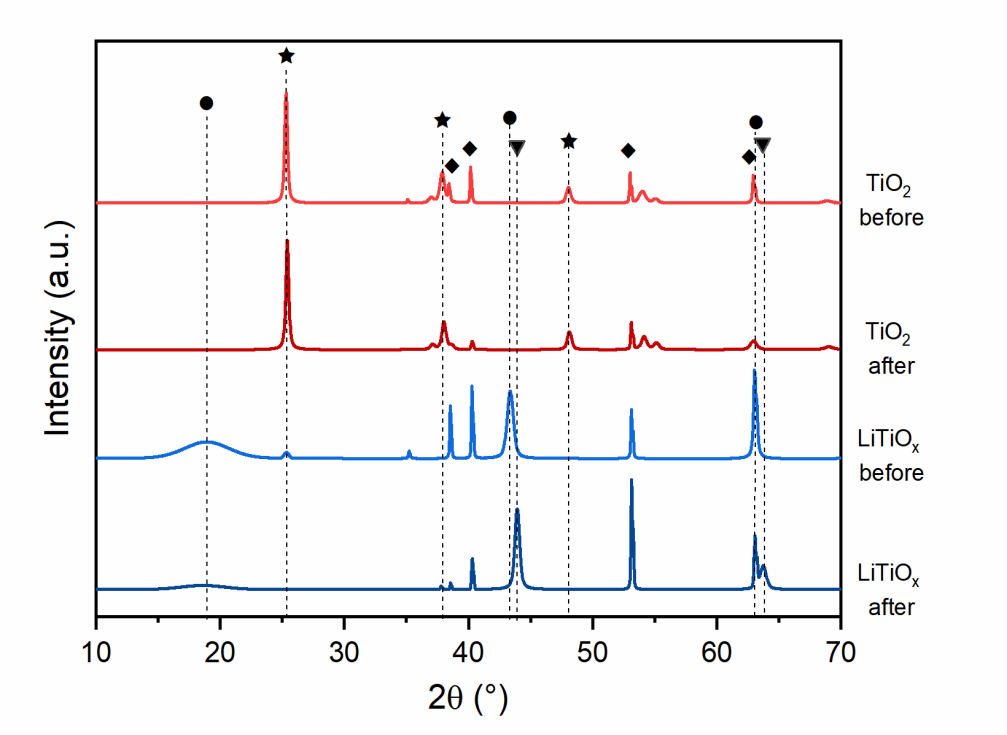


Figure 5.14. XRD patterns of the TiO_2 and lithiated samples before and after the EC characterizations. Stars indicate the anatase phase, circles the lithium-poor phase, reversed triangles the lithium-rich phase, and rhombuses the titanium foil underneath.

differences in their diffractograms before and after cycling. In fact, it is possible to see that the peak at around 43° shifts to slowly higher angles (around 44.5°) and similarly does the one at 63° which splits into two smaller peaks, with the one of the lithiated phase at around 64°. These shifts cannot be attributable to the position of the samples, as the peaks of titanium do not shift. This new phase was indexed with reversed triangles on the patterns and could be attributed to a phase richer in lithium and with an average Li:Ti ratio of 2:1. Furthermore, morphological analyses showed that the morphology was also conserved after the electrochemical characterizations, as can be seen in Figure 5.15.

Compositional analyses were also performed on the different lithiated samples to better understand the changes observed through XRD diffractograms between the before and after the electrochemical characterizations (both crystallographic and compositional analyses on delithiated samples will be discussed in *De-lithiation mechanism*). At first wide-energy scans were performed on all samples to confirm the presence of lithium in the samples (see Figure 5.16). HR spectra of the lithium 1s region were then acquired for the lithiated samples both before and after the EC characterizations (see Figure 5.17). Each acquisition was deconvoluted into separate components, but only the one attributed to the lithium/titanium phase was

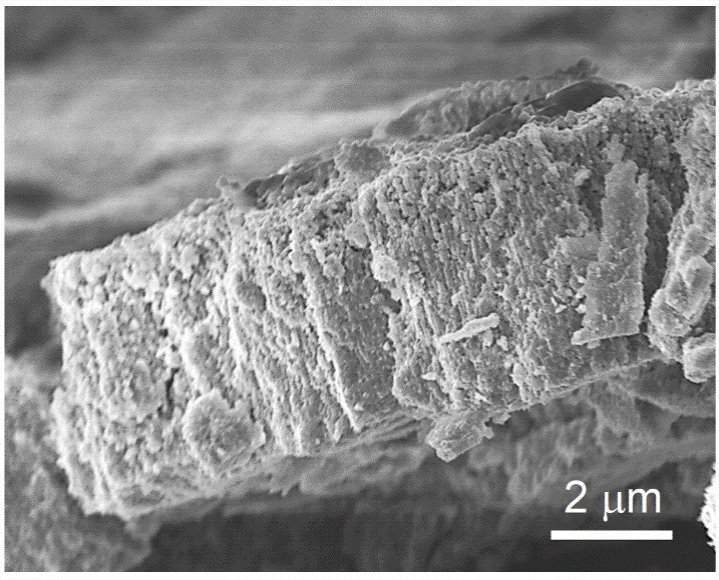


Figure 5.15. SEM micrography of the $LiTiO_x$ nanotubes after the EC characterizations. Adapted under the CC-BY license.[308] Copyright 2022, The Authors, published by Wiley-VCH.

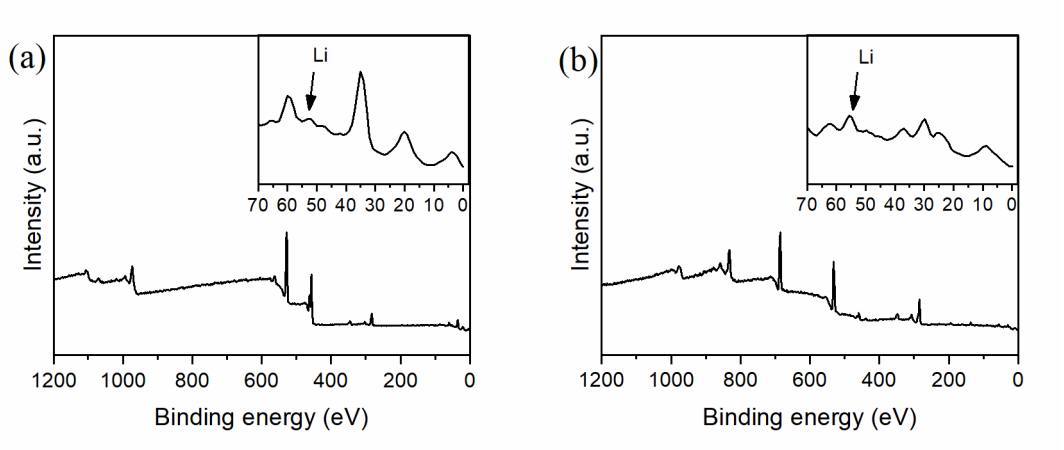


Figure 5.16. Survey XPS acquisition of (a) $LiTiO_x$ NTs after the hydrothermal conversion and (b) $LiTiO_x$ samples after the EC characterization.

considered for the quantification of lithium effectively stored into the structure. Focusing first on the $LiTiO_x$ sample after the hydrothermal conversion (Figure 5.17 (a)), it can be seen that a single peak centered at 54.6 ± 0.1 eV can fit the whole signal attributable to a Li_2TiO_3 phase.[336] The amount of lithium stored in this kind of samples resulted to be equal to 9 at.%, but increased up to 17 at.% after the electrochemical characterizations. In this case, it can be seen in Figure 5.17 (b) that the Li 1s peak can be deconvoluted in three different components, positioned at

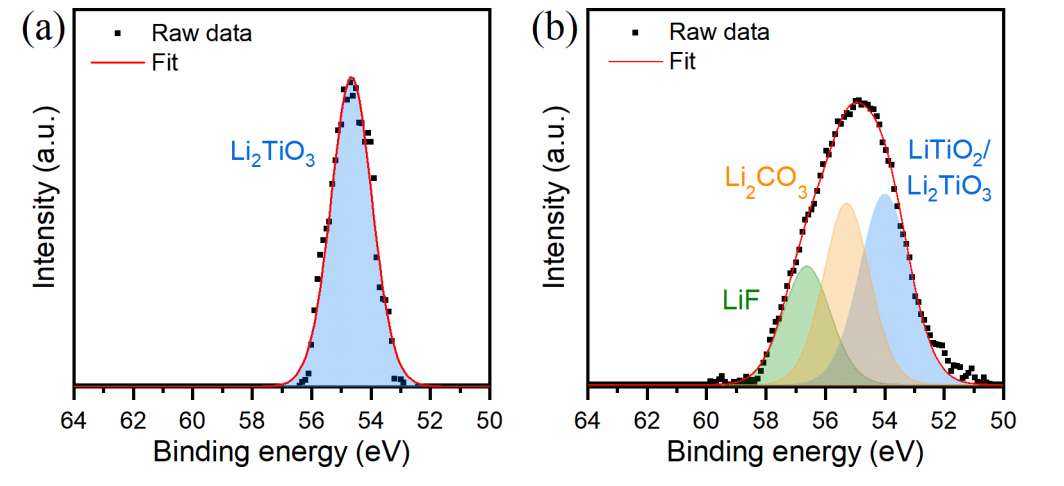


Figure 5.17. HR XPS aquisition of the Li 1s region of (a) $LiTiO_x$ NTs after the hydrothermal conversion and (b) $LiTiO_x$ samples after the EC characterization. Adapted under the CC-BY license.[308] Copyright 2022, The Authors, published by Wiley-VCH.

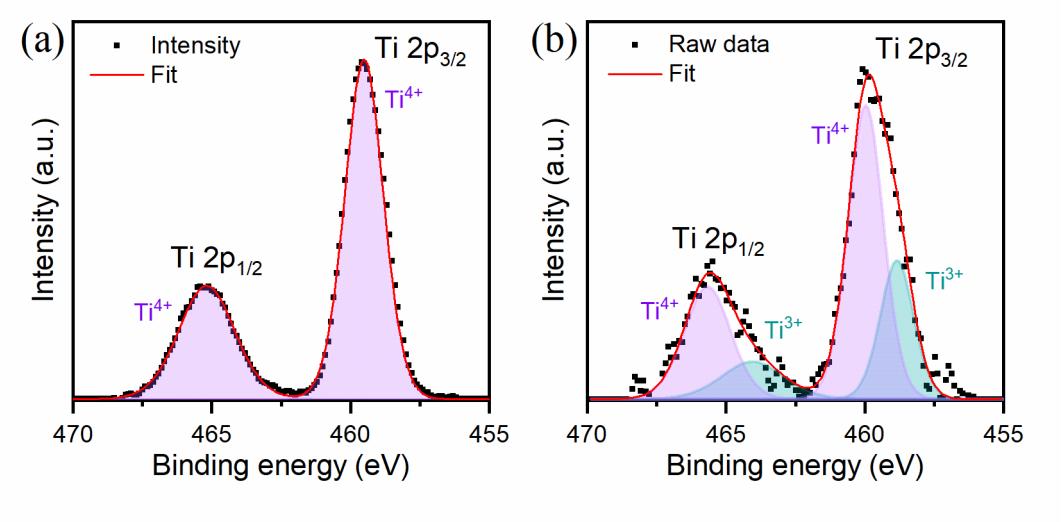


Figure 5.18. HR XPS aquisition of the Ti 2p region of (a) $LiTiO_x$ NTs after the hydrothermal conversion and (b) $LiTiO_x$ samples after the EC characterization. Adapted under the CC-BY license.[308] Copyright 2022, The Authors, published by Wiley-VCH.

56.7±0.1 eV, 55.4±0.1 eV, and 54.1±0.1 eV. These were attributed to LiF, Li_2CO_3 and the titanate phases, respectively, with the first two a result of the decomposition of the organic electrolyte and the last one a mix of two different lithium titanates.[337,338] The co-existence of two different lithium titanate species, Li_2TiO_3 and $LiTiO_2$, derives from the presence of two different lithiation processes that undergo in the samples, one during the hydrothermal conversion and the other during the electrochemical lithiation. This can also be explained by looking at the HR Ti 2p spectra, displayed in Figure 5.18 where it is possible to see that the only titanium valence state present after hydrothermal conversion is Ti^{4+}. However, after the electrochemical characterizations Ti^{3+} valence states can also be observed as a result of a partial reduction.[339] These results appear to be in good agreement with the other characterizations in which lithium storage properties of the lithiated nanotubes had been first seen, therefore suggesting a possible use of this material for lithium harvesting applications.

5.3 Electrochemical characterizations in aqueous solutions

5.3.1 De-lithiation mechanism

As anticipated in section 3.2.4, *Cell assemblage and testing*, the lithiated nanotubes underwent a static de-lithiation treatment to assess their recyclability and stability.

Several other mixed oxide structures, indeed, can undergo crystallographic changes when exposed to acidic environments and can revert back to the rutile phase.[286,287,291]

Lithiated samples subjected to electrochemical characterizations, i.e. with 17 at.% of lithium stored into their structure, were exposed to HCl for 48 hours. The OCP and EIS profiles of the electrodes were monitored to detect any change in the electrodes. The delithiated samples were then subjected to the same morphological, compositional, crystallographic and electrochemical characterizations of the lithiated samples. While the electrochemical properties of the de-lithiated samples in organic electrolyte were already presented, the focus of this paragraph will be the physico-chemical analyses performed on them.

A comparison between the diffractograms of the lithiated and delithiated samples before and after the electrochemical characterizations is displayed in Figure 5.19. One can see that the diffractograms of the lithiated and delithiated

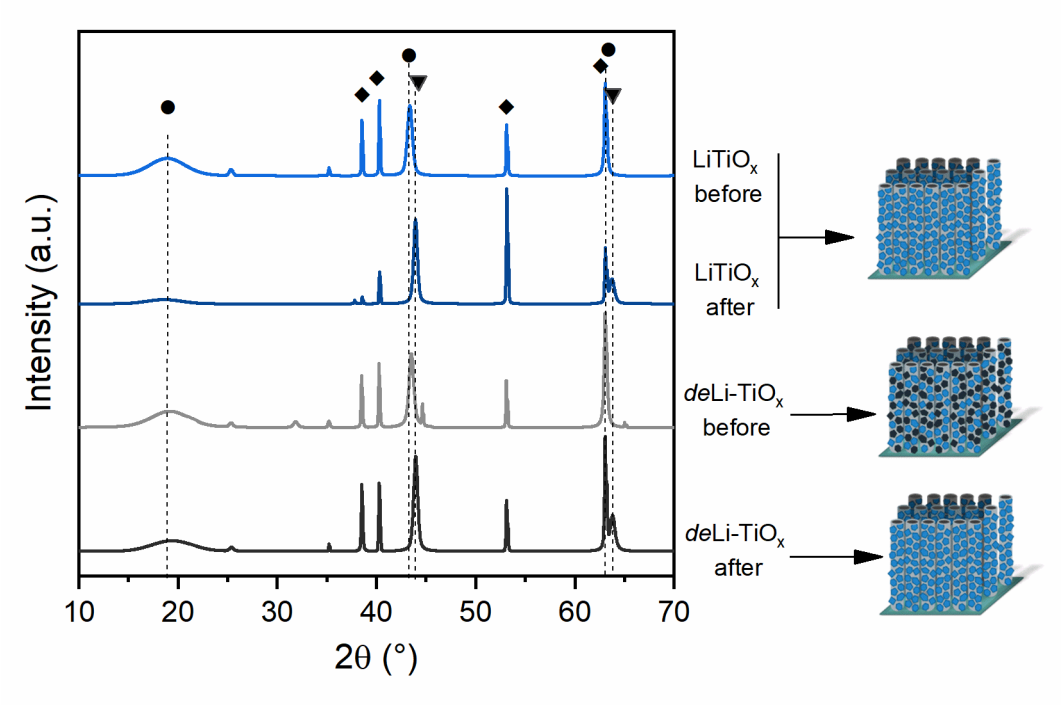


Figure 5.19. XRD patterns of the lithiated and de-lithiated samples before and after the EC characterizations, with schematic representations of the morphologies of lithium-rich and lithium-poor structures. Circles index the lithium-poor mixed oxide, reversed triangles the lithium-rich mixed oxide, and rhombuses the titanium foil underneath. Adapted under the CC-BY license.[308] Copyright 2022, The Authors, published by Wiley-VCH.

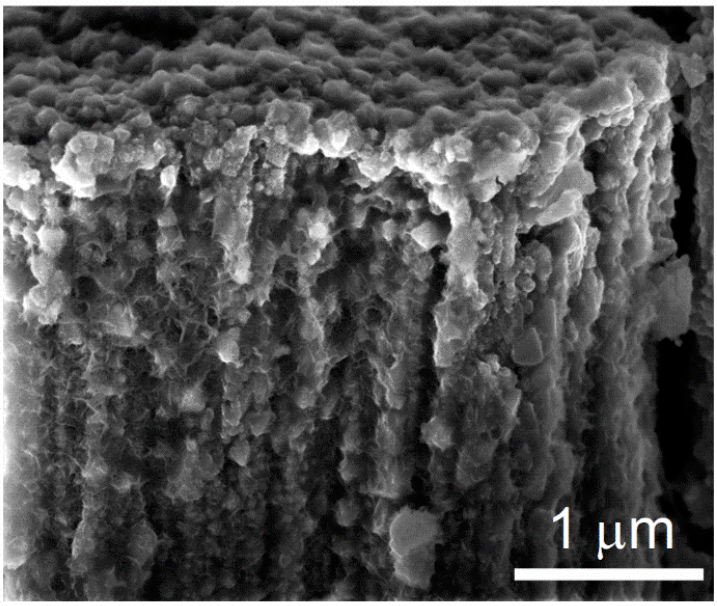


Figure 5.20. SEM micrograph of the delithiated samples.

samples are very similar in terms of peaks, although the ones of the delithiated phase appear less symmetrical and slightly shifted to 0.5° higher. This is in fact in accordance with what previously reported in literature.[292,307] Furthermore, contrary to what was already reported for titanate nanotubes and other sodium titanates, no signs of transformations into rutile phase nor structural disorders were appreciable in these patterns.[286,287] More interestingly, the delithiated nanotubes appear to undergo the same enrichment process as the lithiated ones during the electrochemical characterizations, leading to a lithium-richer phase, indexed with reversed triangles, and their morphology was indeed mostly conserved as can be seen in Figure 5.20. Indeed, although the nanotubes appear more fragile and weathered after the electrochemical characterizations and de-lithiation, they do maintain their tubular morphology. This suggests a good recyclability of the electrodes which was further investigated by means of XPS analyses.

The survey scans of the delithiated samples before and after are shown in Figure 5.21, whereas the HR Li 1s regions of both electrodes are reported in Figure 5.22. Similarly to what happened with the lithiated samples, the Li 1s spectral region was deconvoluted in two to three components. The nanotubes were shown to still have 4 at.% of lithium after the static de-lithiation, and the peak was divided between the Li_2CO_3 component centered at 55.6±0.1 eV and the titanates component centered at 54.7±0.1 eV. However, although the de-lithiation was only partially achieved,

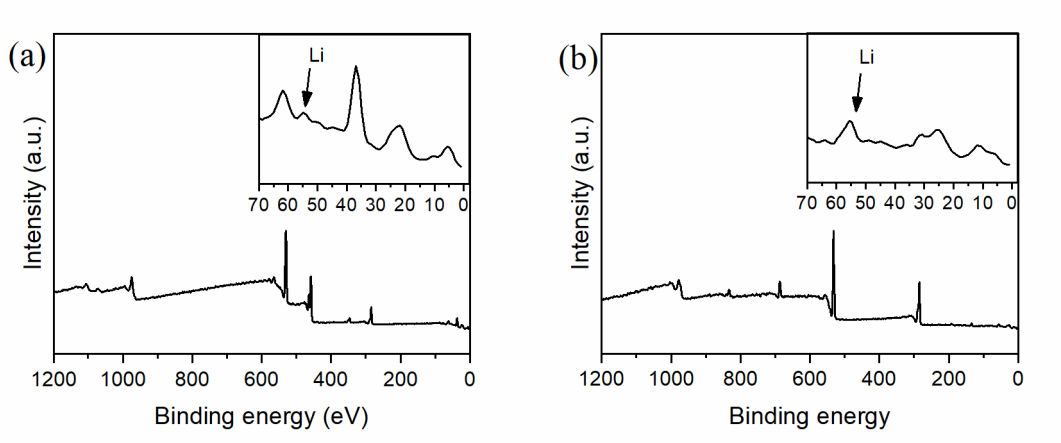


Figure 5.21. Survey XPS acquisition of *de*Li-TiO_x NTs (a) before and (b) after the EC characterizations.

the structure presented incredible reversibility as it was shown to store again up to 17 at.% of lithium after the electrochemical characterizations in organic electrolyte.

The HR Li 1s spectrum of the de-lithiated and lithiated samples after the EC are indeed very similar. These results showed again that these materials, by exhibiting stable and reversible lithium storage properties are excellent candidates for lithium recovery applications.

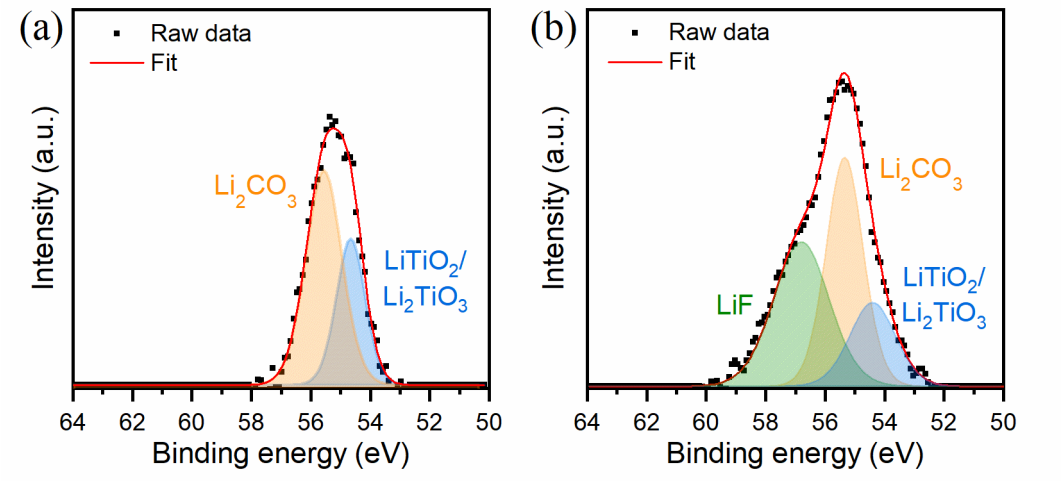


Figure 5.22. HR XPS aquisition of the Li 1s region of *de*Li-TiO_x NTs (a) before and (b) after the EC characterizations. Adapted under the CC-BY license.[308] Copyright 2022, The Authors, published by Wiley-VCH.

5.3.2 Selectivity in LiCl, NaCl, Li/NaCl

The lithiated nanotubes were also tested in aqueous solutions, in the cell described in section 3.2.4. *Cell assemblage and testing.* To this mean, three different solutions were chosen, lithium chloride, sodium chloride and an equimolar mix of lithium and sodium chloride, in order to also assess the selectivity of the electrodes.

The choice of using two-electrode measurements for this kind of analyses was motivated by the fact that a lithium reference electrode was not suitable in aqueous solutions. Furthermore, it had been previously observed that the carbon-based counter electrode with high superficial area resulted virtually non polarizable and with a very stable potential with respect to the working electrode. As can be seen in Figure 5.23 the potential of the carbon-based counter electrode varied of less than 200 mV during the cycling of the lithiated electrodes in a three volt potential window, i.e. 6%: its influence on the system was therefore deemed negligible. This can be further seen when comparing the Nyquist plots of the two electrodes. The impedance of the counter electrode (see Figure 5.24 b) is much smaller than the one of the working electrode (see Figure 5.24 a) and can therefore be considered negligible in the series of the two impedances. Furthermore the capacitance is shown to be dominated by the working electrode as can be seen from the reactance orders of magnitude of the two electrodes.

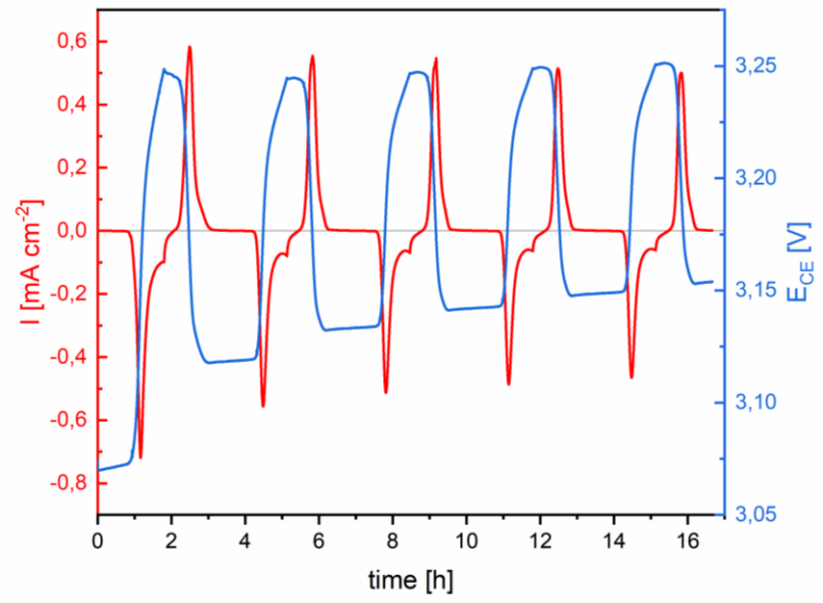


Figure 5.23. Polarization of the carbon-based counter electrode during the cycling of the working electrode of lithiated nanotubes over a 3V potential window.

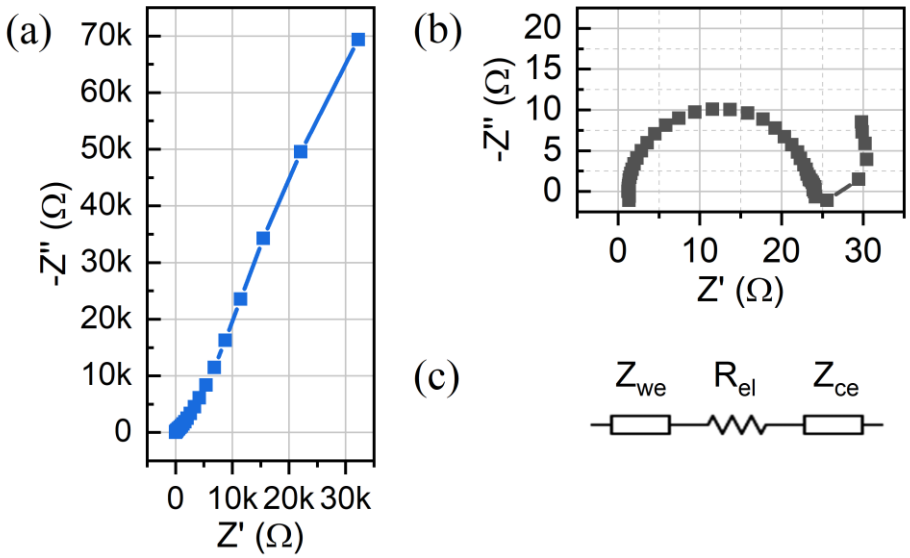


Figure 5.24. Nyquist plot of the (a) lithiated nanotube electrode and (b) carbon-based counter electrode, (c) equivalent circuit of the cell.

A three-electrode trial was also performed for the sake of completeness in batch mode with a platinum counter electrode and an Ag/AgCl reference electrode, since the successive tests would be performed in chloride solutions. The results of the comparison between the two-electrode cell and the three-electrode one is shown in Figure 5.25, where one can see that the two profiles are quite similar. In particular it can be seen that as previously mentioned the carbona-based counter electrode contribution to the profile was only resistive and that the current peak was of similar magnitude in the two cases. The two electrode measurement was therefore chosen

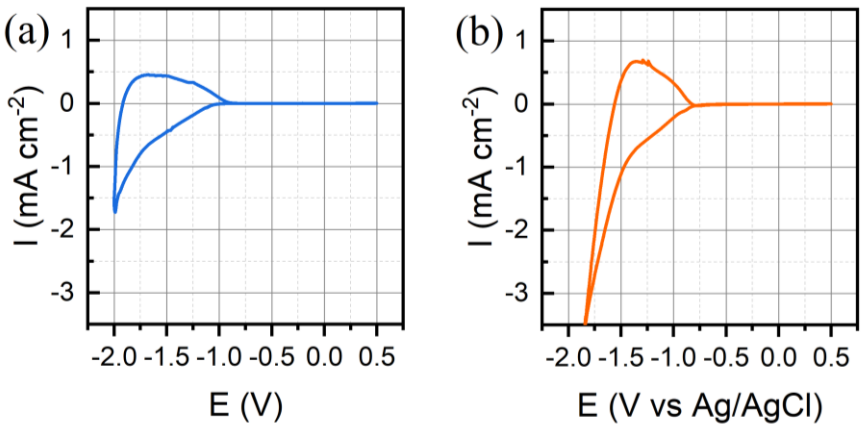


Figure 5.25. (a) two-electrodes and (b) three-electrode cyclic voltammetries profiles of LiTiOx samples in LiCl 100 mM.

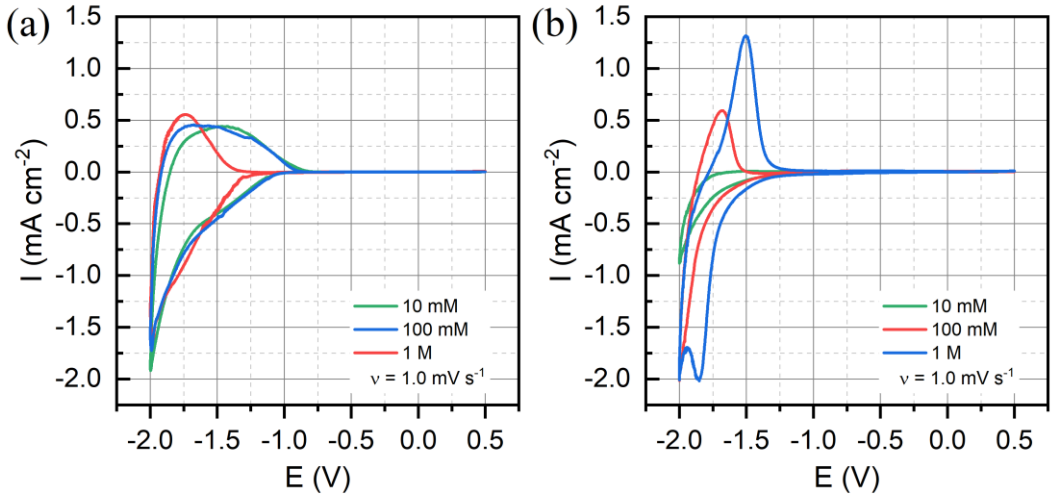


Figure 5.26. Cyclic voltammetries of (a) $LiTiO_x$ and (b) TiO_2 anatase samples in LiCl at different concentrations.

for the successive tests in order to have the same architecture of the cell in the two environments, organic and aqueous, and as proof of concept for future devices.

At first, cyclic voltammetries in pure LiCl solutions were conducted on lithiated samples and pristine anatase samples. Different solutions were tested, i.e. 10 mM, 100 mM and 1 M and the concentration of 100 mM was chosen for the successive tests for all solutions as it provided the best results. Indeed, it can be seen that in the case of $LiTiO_x$, no significant differences could be appreciated when shifting from 10 mM to 100 mM, and the capacity was reduced at higher concentrations (see Figure 5.26 (a)). Instead, for anatase samples at low concentrations no peaks were appreciable, whereas at higher concentrations the profile seemed to suggest a competition between hydrogen evolution and lithium intercalation (see Figure 5.26 (b)). The presence of the competing process was further confirmed by performing a galvanostatic charge-discharge sequence which highlighted the presence of two separate phenomena while testing the anatase nanotubes.

$LiTiO_x$ samples were then tested in aqueous solutions of different compositions to assess their selectivity and properties. Cyclic voltammetries and EIS profiles of the tests in LiCl 100 mM, NaCl 100 mM and a mix of LiCl and NaCl 100 mM are displayed in Figure 5.27. It is possible to notice that the electrodes behave in a similar way in the three solutions, presenting similar values of cell resistance, coulombic efficiencies and similar peaks. The color code used in Figure 5.27 will

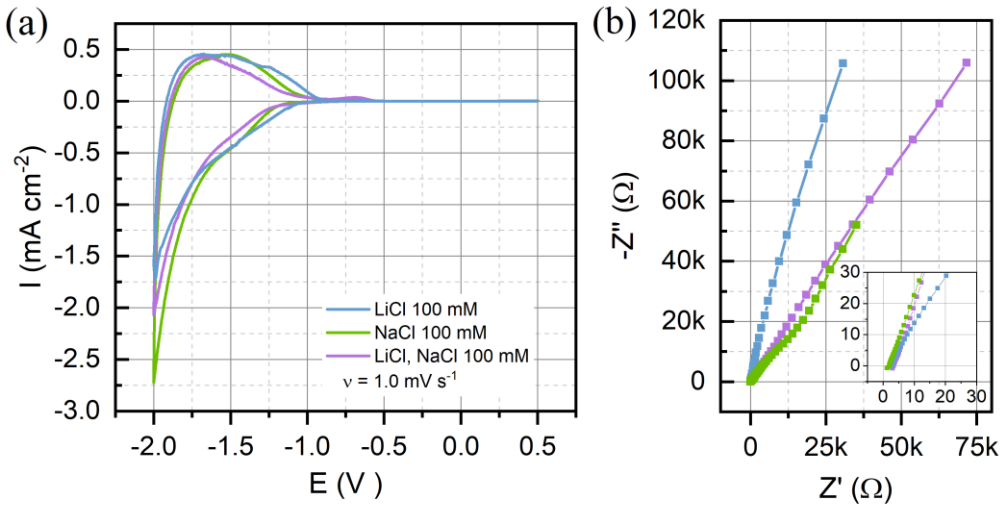


Figure 5.27. (a) Cyclic voltammetries and (b) EIS profiles of $LiTiO_x$ samples in LiCl (blue), NaCl (green) and LiCl/NaCl 100 mM (purple).

be used from here on for the measurements in aqueous environment: blue will be used for tests in LiCl, green for NaCl and purple for the mixed cation solution.

XRD measurements were then performed on the electrodes both at *full cycle* and *half cycle* conditions, by performing a linear sweep voltammetry on the electrodes. This was done to assess whether the cations could be successfully introduced in the structure and whether they could be stored as was the case of $LiTiO_x$ when tested in organic environment. The results of the analyses at half cycle are displayed in Figure 5.28. It is possible to see that at half cycle in lithium chloride there is indeed the presence of a lithium-rich phase which can be identified by the shift of the peak at 43° and the second small peak at around 63°. Similarly to the case of the samples cycled in organic electrolyte (see Figure 5.19), this phase has been indexed with reverse triangles, whereas the initial Li-Ti-O phase is again indexed with circles and the titanium foil with rhombuses. It is interesting to focus on the peak at around 43°, which in the case of the mixed cation solution shows an additional peak related to the intercalation of sodium ions. This is the same contribution visible in the sample tested in NaCl whose peak at around 43° is broader and slightly shifted with respect to the one of lithium.

The diffractograms at full cycle are instead displayed in Figure 5.29. Conversely to what previously observed in organic environments, here the peaks of the lithium-rich phase are not particularly visible. There is a shift in the peak at 43° but no

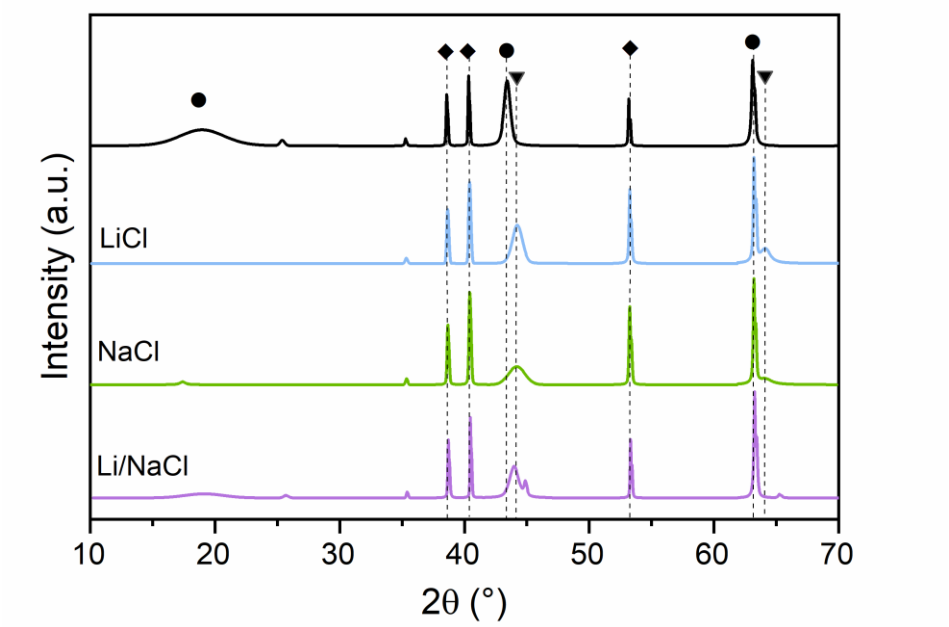


Figure 5.28. XRD patterns of $LiTiO_x$ in LiCl (in blue), NaCl (in green) and mixed cation solution (in purple) at half cycle. The reference sample of $LiTiO_x$ is shown in black. Circles index the lithium-poor mixed oxide, reversed triangles the lithium-rich mixed oxide and rhombuses the titanium foil underneath.

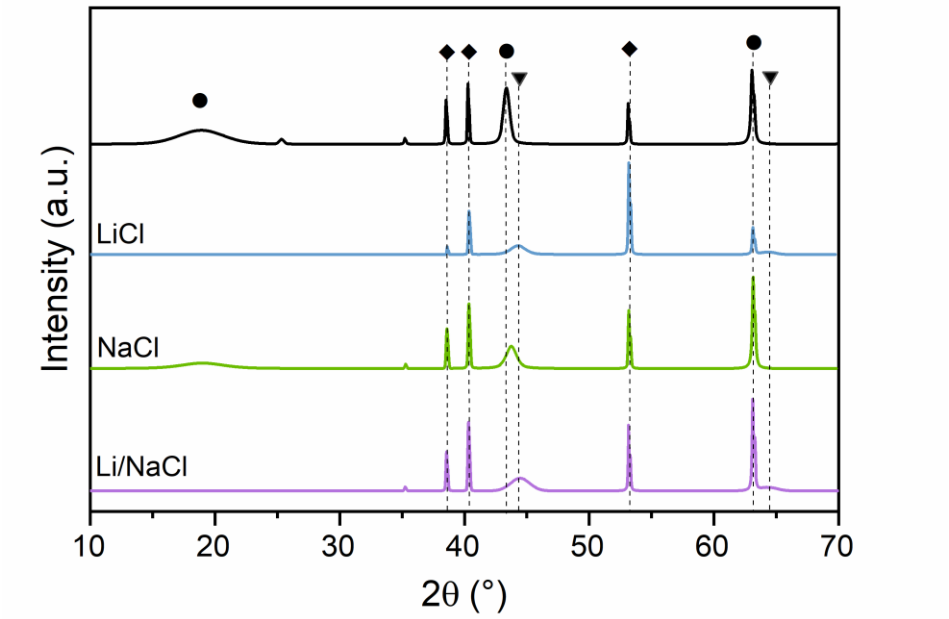


Figure 5.29. XRD patterns of $LiTiO_x$ in LiCl (in blue), NaCl (in green) and mixed cation solution (in purple) at full cycle. The reference sample of $LiTiO_x$ is shown in black. Circles index the lithium-poor mixed oxide, reversed triangles the lithium-rich mixed oxide and rhombuses the titanium foil underneath.

second peak between 63° and 64° are appreciable. It is worth-mentioning, however, that in the case of sodium chloride the broad peak at 18° is again visible, hinting at a possible conservation of the lithium-poor mixed oxide.XPS measurements were finally performed on these samples to further investigate their composition and determine whether they could be used for lithium recovery from aqueous solutions. Both survey scans and HR spectra were obtained for the different samples and the peaks corresponding to Li 1s, Ti 2p and Na 1s were analyzed in addition to the classical C 1s and O 1s.

In all samples, the Li 1s peak only showed one component attributable to the titanate phase centered at 54.7±0.1 eV, but the concentrations of lithium here encountered were fairly lower than what previously reported for the other samples. Indeed, no uptake was found in these samples at *full cycle* conditions. Instead, the samples appeared to have very low amounts of lithium still in the structure (2.76 at.% in the sample cycled in pure LiCl, and lower in the others).

However, it is interesting to notice that a certain selectivity whenever sodium is present seem to be maintained. As it is possible to see in Table 5.3, where the concentrations of the half cycle samples are reported, in presence of equimolar cations in the aqueous electrolyte, the amount of sodium at half cycle was lower than when only sodium was present. Furthermore, the amount of lithium stored in the structure in presence of only lithium and both cations seems to be the same. It must be highlighted that these results cannot be considered conclusive and exhaustive, as they were performed on samples that had undergone only a few cycles of electrochemical testing. Instead, the samples tested in organic electrolyte underwent several weeks of cycling before the compositional characterizations. These can however be seen as a first encouraging step in the characterization of these electrodes.

In order to fully characterize these electrodes, these should be tested as previously said for longer periods of time and at different concentrations. Furthermore, the de-lithiation process of these samples in which some sodium could be intercalated should also be investigated from half cycle conditions. However, based on the results thus obtained, a possible use of these electrodes in hybrid CDI or as hybrid supercapacitor setups could be envisaged.

Table 5.3. Compositional analyses of the samples tested in Li/NaCl, NaCl and LiCl at half cycle conditions.

Sample	C (at.%)	O (at.%)	Ti (at.%)	Li (at.%)	Na (at.%)
Li/Na half cycle	29.10 ± 0.52	48.50 ± 0.54	14.12 ± 0.17	5.37 ± 0.68	2.91 ± 0.24
Na half cycle	27.75 ± 0.50	50.31 ± 0.52	14.20 ± 0.16	4.37 ± 0.68	3.37 ± 0.24
Li half cycle	22.31 ± 0.47	56.62 ± 0.53	15.74 ± 0.17	5.33 ± 0.64	--

Chapter 6

Conclusions

The world of lithium recovery from unconventional resources is vast and dynamical. Almost every day new sources become available and new technologies are discovered to unlock the untapped amounts of this critical material. To contextualize the importance of lithium in today's economy and of its sustainable government, a summary of lithium market share, applications and availability was first addressed.

An overview of the state of the art of this topic was then provided in Chapter 2, underlining the differences between passive adsorption processes, among which one can find ion sieves and membranes, and electrochemical processes, like ion pumping and capacitive deionization. While addressing these technologies, a particular focus on the materials used in the experimental part was provided.

In this work, two different approaches were presented, one from each family of processes. The experimental methods for each one was presented in Chapter 3. Details on the optimization of the synthesis of the functionalized graphene oxide membranes and the filtration protocols were provided as well as specifics of the anodic oxidation and hydrothermal treatment of the titania nanotubes. The cell configuration of the electrochemical analyses of the nanotubes was then discussed in relation to the different environments tested. This chapter ended with an overview of the different techniques to characterize both setups from a physico-chemical and electrochemical point of view.

The lithium recovery process by means of a functionalized graphene oxide membrane was then presented. The success of the functionalization treatment was proved with several different characterizations, as well as the better mechanical stability of the formulation with an additional polymeric binder. Furthermore, the first tests on mono-cation solutions confirmed the selectivity of the membranes thus prepared. An impressive recovery of 70% of the lithium contained in a diluted solution of 1 mM LiCl was also achieved, making the system competitive with other membranes already present in the literature.

A second approach was then displayed, involving the hydrothermal conversion of anodically grown TiO_2 nanotubes. Initially, the best conversion conditions to optimize the crystallinity and morphology of the resulting $LiTiO_x$ nanotubes were addressed. Their properties when cycling in an organic electrolyte were then discussed, with a particular focus on the lithium diffusion in the structure and a possible uptake at the end of the characterization, which reached a content of 17 at.% of lithium. A possible static de-lithiation treatment of the $LiTiO_x$ nanotubes was then investigated, with a similar approach of the one used with ion sieves. The nanotubes showed excellent stability both from a morphological and structural point of view when almost all lithium could be extracted from the samples. Furthermore, the electrochemical properties of the *de*Li-TiO_x showed that these samples could again store lithium ions up to 17 at.% proving a stable and reversible behavior while cycling in organic electrolyte. Their possible use in aqueous solutions was then addressed, although only the preliminary tests were carried out. From these initial analyses, it was possible to see that the nanotubes could indeed show some selectivity even in aqueous solutions, although their performance resulted to be lower than in organic environment. Indeed, the tests in LiCl, NaCl and Li/NaCl seemed to hint that the amount of lithium stored in the structure at half cycle conditions was independent from the presence of other co-existing cations, whereas a secondary uptake of sodium was low and reduced when both lithium and sodium were present.

6.1 Future developments

The results herein reported constitute only a preliminary set of tests to assess the suitability of these two technologies for a successful lithium recovery process. In the case of the f-GO membranes, multi-cation solutions should be tested, first in equimolar concentration and then with more realistic concentrations. Although the membranes could be used with streams already pre-treated to remove most of the

unwanted elements, limiting these additional steps could simplify a potential scaling up of the technology. A possible automation of the setup, now requiring a manual change of the solutions should also be addressed, as explained elsewhere.[64] However, this technology could be easily implemented to recover different elements at once. An example of this strategy, where Fe_3O_4@SiO_2 particles had been functionalized with two different crown ether molecules to recover both lithium and rubidium from the same stream.[113] This strategy could be tested with graphene oxide flakes in order to target several critical raw materials at once with the same membrane. These systems could be further used in sensing, which was the first sector in which crown ether molecules were studied, for example is environmental monitoring[340] or biomedical applications.

$LiTiO_x$ NTs, instead, appear to be a more mature technology. Reactors have indeed been already designed in the literature to allow for an easy flow of solutions in the chambers of an electrochemical cell.[64] However, only the properties of the samples in organic electrolyte were here fully studied. Two different approaches could be proposed to further study this material. A first one consists in testing their behavior in organic electrolytes with other cations present, to assess their selectivity in this kind of systems. A second direction that should be taken, instead, is the full testing of properties and selectivity of the NTs in aqueous solutions of different complexity and for longer periods of time. The preliminary trials reported in this work, in fact, comprised only short tests with less than 10 cycles. This could be one of the reasons for which less lithium was stored in the structure. Furthermore, by optimizing the asymmetric cell configuration herein proposed with a carbon-based counter electrode, one could investigate the application of the NTs in hybrid capacitive deionization setups for either lithium recovery or desalination purposes. Another option would be to investigate a possible hydrothermal conversion of the titania nanotubes in other mixed oxides, to use for example in batteries, in the case of sodium or potassium.

Chapter 7

References

(1) International Organization for Standardization. ISO 14000 family - Environmental management https://www.iso.org/iso-14001-environmental-management.html (accessed Mar 1, 2022).

(2) The 17 Goals | Sustainable Development https://sdgs.un.org/goals (accessed Nov 29, 2021).

(3) Critical raw materials https://ec.europa.eu/growth/sectors/raw-materials/areas-specific-interest/critical-raw-materials_en (accessed Nov 29, 2021).

(4) Burton, J. U.S. Geological Survey Releases 2022 List of Critical Minerals | U.S. Geological Survey https://www.usgs.gov/news/national-news-release/us-geological-survey-releases-2022-list-critical-minerals# (accessed Feb 24, 2022).

(5) Goal 12 | Department of Economic and Social Affairs https://sdgs.un.org/goals/goal12 (accessed Nov 29, 2021).

(6) Meshram, P.; Pandey, B. D.; Mankhand, T. R. Extraction of Lithium from Primary and Secondary Sources by Pre-Treatment, Leaching and Separation: A Comprehensive Review. *Hydrometallurgy* **2014**, *150*, 192–208. https://doi.org/10.1016/j.hydromet.2014.10.012.

(7) Choubey, P. K.; Chung, K.-S.; Kim, M.; Lee, J.; Srivastava, R. R. Advance Review on the Exploitation of the Prominent Energy-Storage Element Lithium. Part II: From Sea Water and Spent Lithium Ion Batteries (LIBs). *Miner. Eng.* **2017**, *110*, 104–121. https://doi.org/10.1016/j.mineng.2017.04.008.

(8) Swain, B. Recovery and Recycling of Lithium: A Review. *Sep. Purif. Technol.* **2017**, *172*, 388–403. https://doi.org/10.1016/j.seppur.2016.08.031.

(9) Grosjean, C.; Herrera Miranda, P.; Perrin, M.; Poggi, P. Assessment of World Lithium Resources and Consequences of Their Geographic Distribution on the Expected Development of the Electric Vehicle Industry. *Renew. Sustain. Energy Rev.* **2012**, *16* (3), 1735–1744. https://doi.org/10.1016/j.rser.2011.11.023.

(10) Meng, F.; McNeice, J.; Zadeh, S. S.; Ghahreman, A. Review of Lithium Production and Recovery from Minerals, Brines, and Lithium-Ion Batteries. *Miner. Process. Extr. Metall. Rev.* **2021**, *42* (2), 123–141. https://doi.org/10.1080/08827508.2019.1668387.

(11) Flexer, V.; Baspineiro, C. F.; Galli, C. I. Lithium Recovery from Brines: A Vital Raw Material for Green Energies with a Potential Environmental Impact in Its Mining and Processing. *Sci. Total Environ.* **2018**, *639*, 1188–1204. https://doi.org/10.1016/j.scitotenv.2018.05.223.

(12) Narins, T. P. The Battery Business: Lithium Availability and the Growth of the Global Electric Car Industry. *Extr. Ind. Soc.* **2017**, *4* (2), 321–328. https://doi.org/10.1016/j.exis.2017.01.013.

(13) IEA. *Global EV Outlook 2019*; OECD: Paris, 2019. https://doi.org/10.1787/35fb60bd-en.

(14) MarketsandMarkets. *Lithium-Ion Battery Market with COVID-19 Impact Analysis, by Type (Li-NMC, LFP, LCO, LTO, LMO, NCA), Capacity, Voltage, Industry (Consumer Electronics, Automotive, Power, Industrial), & Region (North America, Europe, APAC & RoW) - Global Forecast to 2030*; 2021.

(15) Li, L.; Deshmane, V. G.; Paranthaman, M. P.; Bhave, R.; Moyer, B. A.; Harrison, S. Lithium Recovery from Aqueous Resources and Batteries: A Brief Review. *Johnson Matthey Technol. Rev.* **2018**, *62* (2), 161–176. https://doi.org/10.1595/205651317X696676.

(16) United States Geological Survey. *Mineral Commodity Summaries 2020: U.S. Geological Survey*; Reston, VA, 2020. https://doi.org/10.3133/mcs2020.

(17) Choubey, P. K.; Kim, M. S.; Srivastava, R. R.; Lee, J. C.; Lee, J. Y. Advance Review on the Exploitation of the Prominent Energy-Storage Element: Lithium. Part I: From Mineral and Brine Resources. *Miner. Eng.* **2016**, *89*, 119–137. https://doi.org/10.1016/j.mineng.2016.01.010.

(18) Kesler, S. E.; Gruber, P. W.; Medina, P. A.; Keoleian, G. A.; Everson, M. P.; Wallington, T. J. Global Lithium Resources: Relative Importance of Pegmatite, Brine and Other Deposits. *Ore Geol. Rev.* **2012**, *48*, 55–69. https://doi.org/10.1016/j.oregeorev.2012.05.006.

(19) Liu, G.; Zhao, Z.; Ghahreman, A. Novel Approaches for Lithium Extraction from Salt-Lake Brines: A Review. *Hydrometallurgy* **2019**, *187*, 81–100. https://doi.org/10.1016/j.hydromet.2019.05.005.

(20) Martin, G.; Rentsch, L.; Höck, M.; Bertau, M. Lithium Market Research – Global Supply, Future Demand and Price Development. *Energy Storage Mater.* **2017**, *6*, 171–179. https://doi.org/10.1016/j.ensm.2016.11.004.

(21) Bradley, D. C.; Stillings, L. L.; Jaskula, B. W.; McCauley, A. D. Lithium. U.S. Geological Survey Professional Paper 1802-K. In *Critical Mineral Resources of the United States—Economic and Environmental Geology and Prospects for Future Supply*; Schulz, K. J., DeYoung, J. H. J., Seal, R. R. I., Bradley, D. C., Eds.; 2017; pp K1–K21. https://doi.org/10.3133/pp1802.

(22) United States Geological Survey. *Mineral Commodity Summaries 2022: U.S. Geological Survey*; Reston, VA, 2022. https://doi.org/10.3133/mcs2022.

(23) Gruber, P. W.; Medina, P. A.; Keoleian, G. A.; Kesler, S. E.; Everson, M. P.; Wallington, T. J. Global Lithium Availability: A Constraint for Electric Vehicles? *J. Ind. Ecol.* **2011**, *15* (5), 760–775. https://doi.org/10.1111/j.1530-9290.2011.00359.x.

(24) Vikström, H.; Davidsson, S.; Höök, M. Lithium Availability and Future Production Outlooks. *Appl. Energy* **2013**, *110*, 252–266. https://doi.org/10.1016/j.apenergy.2013.04.005.

(25) Li, W.; Zhang, W.; Li, T.; Wei, A.; Liu, Y.; Wang, H. An Important Factor Affecting the Supercapacitive Properties of Hydrogenated TiO2 Nanotube Arrays: Crystal Structure. *Nanoscale Res. Lett.* **2019**, *14* (1), 229. https://doi.org/10.1186/s11671-019-3047-2.

(26) Talens Peiró, L.; Villalba Méndez, G.; Ayres, R. U. Lithium: Sources, Production, Uses, and Recovery Outlook. *JOM* **2013**, *65* (8), 986–996. https://doi.org/10.1007/s11837-013-0666-4.

(27) Lemaire, J.; Svecova, L.; Lagallarde, F.; Laucournet, R.; Thivel, P. X. Lithium Recovery from Aqueous Solution by Sorption/Desorption. *Hydrometallurgy* **2014**, *143*, 1–11. https://doi.org/10.1016/j.hydromet.2013.11.006.

(28) Dunn, J. B.; Gaines, L.; Sullivan, J.; Wang, M. Q. Impact of Recycling on Cradle-to-Gate Energy Consumption and Greenhouse Gas Emissions of Automotive Lithium-Ion Batteries. *Environ. Sci. Technol.* **2012**, *46* (22), 12704–12710. https://doi.org/10.1021/es302420z.

(29) Calvo, E. J. Electrochemical Methods for Sustainable Recovery of Lithium from Natural Brines and Battery Recycling. *Curr. Opin. Electrochem.* **2019**, *15* (1), 102–108. https://doi.org/10.1016/j.coelec.2019.04.010.

(30) Prior, T.; Wäger, P. A.; Stamp, A.; Widmer, R.; Giurco, D. Sustainable Governance of Scarce Metals: The Case of Lithium. *Sci. Total Environ.* **2013**, *461–462*, 785–791. https://doi.org/10.1016/j.scitotenv.2013.05.042.

(31) André, H.; Ljunggren, M. Towards Comprehensive Assessment of Mineral Resource Availability? Complementary Roles of Life Cycle, Life Cycle Sustainability and Criticality Assessments. *Resour. Conserv. Recycl.* **2021**, *167*, 105396. https://doi.org/10.1016/j.resconrec.2021.105396.

(32) Ambrose, H.; Kendall, A. Understanding the Future of Lithium: Part 2, Temporally and Spatially Resolved Life-cycle Assessment Modeling. *J. Ind. Ecol.* **2020**, *24* (1), 90–100. https://doi.org/10.1111/jiec.12942.

(33) Huang, T.-Y.; Pérez-Cardona, J. R.; Zhao, F.; Sutherland, J. W.; Paranthaman, M. P. Life Cycle Assessment and Techno-Economic Assessment of Lithium Recovery from Geothermal Brine. *ACS Sustain. Chem. Eng.* **2021**, *9* (19), 6551–6560. https://doi.org/10.1021/acssuschemeng.0c08733.

(34) Manjong, N. B.; Usai, L.; Burheim, O. S.; Strømman, A. H. Life Cycle Modelling of Extraction and Processing of Battery Minerals—A Parametric Approach. *Batteries* **2021**, *7* (3), 57. https://doi.org/10.3390/batteries7030057.

(35) Bello, A. S.; Zouari, N.; Da'ana, D. A.; Hahladakis, J. N.; Al-Ghouti, M. A. An Overview of Brine Management: Emerging Desalination Technologies, Life Cycle Assessment, and Metal Recovery Methodologies. *J. Environ. Manage.* **2021**, *288*, 112358. https://doi.org/10.1016/j.jenvman.2021.112358.

(36) Bardi, U. Extracting Minerals from Seawater: An Energy Analysis. *Sustainability* **2010**, *2* (4), 980–992. https://doi.org/10.3390/su2040980.

(37) Loganathan, P.; Naidu, G.; Vigneswaran, S. Mining Valuable Minerals from Seawater: A Critical Review. *Environ. Sci. Water Res. Technol.* **2017**, *3* (1), 37–53. https://doi.org/10.1039/c6ew00268d.

(38) Can Sener, S. E.; Thomas, V. M.; Hogan, D. E.; Maier, R. M.; Carbajales-Dale, M.; Barton, M. D.; Karanfil, T.; Crittenden, J. C.; Amy, G. L. Recovery of Critical Metals from Aqueous Sources. *ACS Sustain. Chem. Eng.* **2021**, *9* (35), 11616–11634. https://doi.org/10.1021/acssuschemeng.1c03005.

(39) Park, J.; Sato, H.; Nishihama, S.; Yoshizuka, K. Separation and Recovery of Lithium from Geothermal Water by Sequential Adsorption Process with λ-MnO 2 and TiO2. *Ion Exch. Lett.* **2012**, *5*, 1–5. https://doi.org/10.3260/iel.2012.08.001.

(40) Paranthaman, M. P.; Li, L.; Luo, J.; Hoke, T.; Ucar, H.; Moyer, B. A.; Harrison, S. Recovery of Lithium from Geothermal Brine with Lithium–Aluminum Layered Double Hydroxide Chloride Sorbents. *Environ. Sci. Technol.* **2017**, *51* (22), 13481–13486. https://doi.org/10.1021/acs.est.7b03464.

(41) Stringfellow, W. T.; Dobson, P. F. Technology for the Recovery of Lithium from Geothermal Brines. *Energies* **2021**, *14* (20), 6805. https://doi.org/10.3390/en14206805.

(42) Chen, S.; Chen, Z.; Wei, Z.; Hu, J.; Guo, Y.; Deng, T. Titanium-Based Ion Sieve with Enhanced Post-Separation Ability for High Performance Lithium Recovery from Geothermal Water. *Chem. Eng. J.* **2021**, *410*, 128320. https://doi.org/10.1016/j.cej.2020.128320.

(43) Toba, A.-L. L.; Nguyen, R. T.; Cole, C.; Neupane, G.; Paranthaman, M. P. U.S. Lithium Resources from Geothermal and Extraction Feasibility. *Resour. Conserv. Recycl.* **2021**, *169*, 105514. https://doi.org/10.1016/j.resconrec.2021.105514.

(44) Miao, J.; Zhao, K.; Guo, F.; Xu, L.; Xie, Y.; Deng, T. Novel LIS-Doped Mixed Matrix Membrane Absorbent with High Structural Stability for Sustainable Lithium Recovery from Geothermal Water. *Desalination* **2022**, *527*, 115570. https://doi.org/10.1016/j.desal.2022.115570.

(45) Zhao, K.; Tong, B.; Yu, X.; Guo, Y.; Xie, Y.; Deng, T. Synthesis of Porous Fiber-Supported Lithium Ion-Sieve Adsorbent for Lithium Recovery from Geothermal Water. *Chem. Eng. J.* **2022**, *430*, 131423. https://doi.org/10.1016/j.cej.2021.131423.

(46) BRGM. EuGeLi: Lithium extraction from geothermal brines in Europe https://www.brgm.fr/en/current-project/eugeli-lithium-extraction-geothermal-brines-europe (accessed Feb 28, 2022).

(47) Eramet. Projet EuGeLi: Du Lithium européen pour les futures batteries des véhicules électriques https://www.eramet.com/fr/activites/innover-concevoir/projet-eugeli (accessed Feb 28, 2022).

(48) Border, S.; Sawyer, L. Evaporites and Brines – Geological, Hydrological and Chemical Aspects of Resource Estimation. *Appl. Earth Sci.* **2014**, *123* (2), 95–106. https://doi.org/10.1179/1743275814Y.0000000053.

(49) Liu, C.; Lin, J.; Cao, H.; Zhang, Y.; Sun, Z. Recycling of Spent Lithium-Ion Batteries in View of Lithium Recovery: A Critical Review. *Journal of Cleaner Production*. Elsevier Ltd 2019, pp 801–813. https://doi.org/10.1016/j.jclepro.2019.04.304.

(50) Khalil, A.; Mohammed, S.; Hashaikeh, R.; Hilal, N. Lithium Recovery from Brine: Recent Developments and Challenges. *Desalination* **2022**, *528*, 115611. https://doi.org/10.1016/j.desal.2022.115611.

(51) Zhang, X.; Zhao, W.; Zhang, Y.; Jegatheesan, V. A Review of Resource Recovery from Seawater Desalination Brine. *Rev. Environ. Sci. Bio/Technology* **2021**, 1–29. https://doi.org/10.1007/s11157-021-09570-4.

(52) Li, X.; Mo, Y.; Qing, W.; Shao, S.; Tang, C. Y.; Li, J. Membrane-Based Technologies for Lithium Recovery from Water Lithium Resources: A Review. *J. Memb. Sci.* **2019**, *591*, 117317. https://doi.org/10.1016/j.memsci.2019.117317.

(53) Zhang, Y.; Sun, W.; Xu, R.; Wang, L.; Tang, H. Lithium Extraction from Water Lithium Resources through Green Electrochemical-Battery Approaches: A Comprehensive Review. *J. Clean. Prod.* **2020**, *285*, 124905. https://doi.org/10.1016/j.jclepro.2020.124905.

(54) Zhou, G.; Chen, L.; Chao, Y.; Li, X.; Luo, G.; Zhu, W. Progress in Electrochemical Lithium Ion Pumping for Lithium Recovery. *J. Energy Chem.* **2021**, *59*, 431–445. https://doi.org/10.1016/j.jechem.2020.11.012.

(55) Orooji, Y.; Nezafat, Z.; Nasrollahzadeh, M.; Shafiei, N.; Afsari, M.; Pakzad, K.; Razmjou, A. Recent Advances in Nanomaterial Development for Lithium Ion-Sieving Technologies. *Desalination* **2022**, *529*, 115624. https://doi.org/10.1016/j.desal.2022.115624.

(56) Xu, X.; Chen, Y.; Wan, P.; Gasem, K.; Wang, K.; He, T.; Adidharma, H.; Fan, M. Extraction of Lithium with Functionalized Lithium Ion-Sieves. *Prog. Mater. Sci.* **2016**, *84*, 276–313. https://doi.org/10.1016/j.pmatsci.2016.09.004.

(57) Safari, S.; Lottermoser, B. G.; Alessi, D. S. Metal Oxide Sorbents for the Sustainable Recovery of Lithium from Unconventional Resources. *Appl. Mater. Today* **2020**, *19*, 100638. https://doi.org/10.1016/J.APMT.2020.100638.

(58) Zhang, Y.; Hu, Y.; Wang, L.; Sun, W. Systematic Review of Lithium Extraction from Salt-Lake Brines via Precipitation Approaches. *Miner. Eng.* **2019**, *139*, 105868. https://doi.org/10.1016/j.mineng.2019.105868.

(59) Gmar, S.; Chagnes, A. Recent Advances on Electrodialysis for the Recovery of Lithium from Primary and Secondary Resources. *Hydrometallurgy* **2019**, *189*, 105124. https://doi.org/10.1016/j.hydromet.2019.105124.

(60) Zhao, X.; Yang, H.; Wang, Y.; Sha, Z. Review on the Electrochemical Extraction of Lithium from Seawater/Brine. *J. Electroanal. Chem.* **2019**, *850*, 113389. https://doi.org/10.1016/j.jelechem.2019.113389.

(61) Joo, H.; Lee, J.; Yoon, J. Short Review: Timeline of the Electrochemical Lithium Recovery System Using the Spinel LiMn2O4 as a Positive Electrode. *Energies* **2020**, *13* (23), 6235. https://doi.org/10.3390/en13236235.

(62) Weng, D.; Duan, H.; Hou, Y.; Huo, J.; Chen, L.; Zhang, F.; Wang, J. Introduction of Manganese Based Lithium-Ion Sieve-A Review. *Prog. Nat. Sci. Mater. Int.* **2020**, *30*, 139–152. https://doi.org/10.1016/j.pnsc.2020.01.017.

(63) LiVecchi, A.; Copping, A.; Jenne, D.; Gorton, A.; Preus, R.; Gill, G.; Robichaud, R.; Green, R.; Geerlofs, S.; Gore, S.; Hume, D.; McShane, W.; Schmaus, C.; Spence, H. *Powering the Blue Economy: Exploring Opportunities for Marine Renewable Energy in Maritime Markets*; Washington, D.C., 2019.

(64) Baudino, L.; Santos, C.; Pirri, C. F.; La Mantia, F.; Lamberti, A. Recent Advances

in the Lithium Recovery from Water Resources: From Passive to Electrochemical Methods. *Adv. Sci.* **2022**, 2201380. https://doi.org/10.1002/advs.202201380.

(65) Battistel, A.; Palagonia, M. S.; Brogioli, D.; La Mantia, F.; Trócoli, R. Electrochemical Methods for Lithium Recovery: A Comprehensive and Critical Review. *Adv. Mater.* **2020**, *1905440*, 1905440. https://doi.org/10.1002/adma.201905440.

(66) Wang, J.; Yue, X.; Wang, P.; Yu, T.; Du, X.; Hao, X.; Abudula, A.; Guan, G. Electrochemical Technologies for Lithium Recovery from Liquid Resources: A Review. *Renew. Sustain. Energy Rev.* **2022**, *154*, 111813. https://doi.org/10.1016/j.rser.2021.111813.

(67) Zavahir, S.; Elmakki, T.; Gulied, M.; Ahmad, Z.; Al-Sulaiti, L.; Shon, H. K.; Chen, Y.; Park, H.; Batchelor, B.; Han, D. S. A Review on Lithium Recovery Using Electrochemical Capturing Systems. *Desalination* **2021**, *500*, 114883. https://doi.org/10.1016/j.desal.2020.114883.

(68) Bustos-Gallardo, B.; Bridge, G.; Prieto, M. Harvesting Lithium: Water, Brine and the Industrial Dynamics of Production in the Salar de Atacama. *Geoforum* **2021**, *119*, 177–189. https://doi.org/10.1016/j.geoforum.2021.01.001.

(69) Volkhin, V. V.; Shulga, E. A.; Zilberman, M. V. Ion-Exchange Properties of Mixed Ferrocyanides of Some Transition Metals. *Newsletters USSR Acad. Sci. Inorg. Mater.* **1971**, *7(1)*, 77–81.

(70) Dai, X.; Zhan, H.; Qian, Z.; Li, J.; Liu, Z.; Wu, Z. Al-Doped H 2 TiO 3 Ion Sieve with Enhanced Li + Adsorption Performance. *RSC Adv.* **2021**, *11* (55), 34988–34995. https://doi.org/10.1039/D1RA06535A.

(71) Zhou, S.; Guo, X.; Yan, X.; Chen, Y.; Lang, W. Zr-Doped Titanium Lithium Ion Sieve and EP-Granulated Composite: Superb Adsorption and Recycling Performance. *Particuology* **2022**, *69*, 100–110. https://doi.org/10.1016/j.partic.2021.12.002.

(72) Chitrakar, R.; Makita, Y.; Ooi, K.; Sonoda, A. Magnesium-Doped Manganese Oxide with Lithium Ion-Sieve Property: Lithium Adsorption from Salt Lake Brine. *Bull. Chem. Soc. Jpn.* **2013**, *86* (7), 850–855. https://doi.org/10.1246/bcsj.20130019.

(73) Chitrakar, R.; Makita, Y.; Ooi, K.; Sonoda, A. Synthesis of Iron-Doped Manganese Oxides with an Ion-Sieve Property: Lithium Adsorption from Bolivian Brine. *Ind. Eng. Chem. Res.* **2014**, *53*, 3682–3688. https://doi.org/10.1021/ie4043642.

(74) Hunter, J. C. Preparation of a New Crystal Form of Manganese Dioxide: λ-MnO2. *J. Solid State Chem.* **1981**, *39* (2), 142–147. https://doi.org/10.1016/0022-4596(81)90323-6.

(75) Feng, Q.; Miyai, Y.; Kanoh, H.; Ooi, K. Li+ Extraction/Insertion with Spinel-Type Lithium Manganese Oxides. Characterization of Redox-Type and Ion-Exchange-Type Sites. *Langmuir* **1992**, *8* (7), 1861–1867. https://doi.org/10.1021/la00043a029.

(76) Thackeray, M. M. Spinel Electrodes for Lithium Batteries. *J. Am. Ceram. Soc.* **2004**, *82* (12), 3347–3354. https://doi.org/10.1111/j.1151-2916.1999.tb02250.x.

(77) Marthi, R.; Asgar, H.; Gadikota, G.; Smith, Y. R. On the Structure and Lithium Adsorption Mechanism of Layered H2TiO3. *ACS Appl. Mater. Interfaces* **2021**, *13* (7), 8361–8369. https://doi.org/10.1021/ACSAMI.0C20691.

(78) Sagara, F.; Ning, W. B.; Yoshida, I.; Ueno, K. Preparation and Adsorption Properties of λ-MnO2- Cellulose Hybrid-Type Lon- Exchanger for Lithium Ion. Application to the Enrichment of Lithium Ion from Seawater. *Sep. Sci. Technol.* **1989**, *24* (14), 1227–1243. https://doi.org/10.1080/01496398908049899.

(79) Hong, H. J.; Park, I. S.; Ryu, T.; Ryu, J.; Kim, B. G.; Chung, K.-S. Granulation of Li1.33Mn1.67O4(LMO) through the Use of Cross-Linked Chitosan for the Effective Recovery of Li+from Seawater. *Chem. Eng. J.* **2013**, *234*, 16–22. https://doi.org/10.1016/j.cej.2013.08.060.

(80) Ding, W.; Zhang, J.; Liu, Y.; Guo, Y.; Deng, T.; Yu, X. Synthesis of Granulated H4Mn5O12/Chitosan with Improved Stability by a Novel Cross-Linking Strategy for Lithium Adsorption from Aqueous Solutions. *Chem. Eng. J.* **2021**, *426*, 131689. https://doi.org/10.1016/J.CEJ.2021.131689.

(81) Ryu, T.; Haldorai, Y.; Rengaraj, A.; Shin, J.; Hong, H.-J.; Lee, G.-W.; Han, Y.-K.; Huh, Y. S.; Chung, K.-S. Recovery of Lithium Ions from Seawater Using a Continuous Flow Adsorption Column Packed with Granulated Chitosan–Lithium Manganese Oxide. *Ind. Eng. Chem. Res.* **2016**, *55* (26), 7218–7225. https://doi.org/10.1021/acs.iecr.6b01632.

(82) Nishihama, S.; Onishi, K.; Yoshizuka, K. Selective Recovery Process of Lithium from Seawater Using Integrated Ion Exchange Methods. *Solvent Extr. Ion Exch.* **2011**, *29* (3), 421–431. https://doi.org/10.1080/07366299.2011.573435.

(83) Han, Y.; Kim, S.; Kim, H.; Park, J. Preparation of Sizable and Uniform-Sized Spherical Ceramic Foams: Drop-in-Oil and Agar Gelation. *J. Am. Ceram. Soc.* **2011**, *94* (9), 2742–2745. https://doi.org/10.1111/j.1551-2916.2011.04681.x.

(84) Han, Y.; Kim, H.; Park, J. Millimeter-Sized Spherical Ion-Sieve Foams with Hierarchical Pore Structure for Recovery of Lithium from Seawater. *Chem. Eng. J.* **2012**, *210*, 482–489. https://doi.org/10.1016/j.cej.2012.09.019.

(85) Zhang, Y.; Wang, L.; Sun, W.; Hu, Y.; Tang, H. Membrane Technologies for Li+/Mg2+ Separation from Salt-Lake Brines and Seawater: A Comprehensive Review. *J. Ind. Eng. Chem.* **2020**, *81*, 7–23.

https://doi.org/10.1016/j.jiec.2019.09.002.

(86) Hou, J.; Zhang, H.; Thornton, A. W.; Hill, A. J.; Wang, H.; Konstas, K. Lithium Extraction by Emerging Metal–Organic Framework-Based Membranes. *Adv. Funct. Mater.* **2021**, 2105991. https://doi.org/10.1002/adfm.202105991.

(87) Thanuttamavong, M.; Yamamoto, K.; Ik Oh, J.; Ho Choo, K.; June Choi, S. Rejection Characteristics of Organic and Inorganic Pollutants by Ultra Low-Pressure Nanofiltration of Surface Water for Drinking Water Treatment. *Desalination* **2002**, *145* (1–3), 257–264. https://doi.org/10.1016/S0011-9164(02)00420-4.

(88) Zaviska, F.; Drogui, P.; Grasmick, A.; Azais, A.; Héran, M. Nanofiltration Membrane Bioreactor for Removing Pharmaceutical Compounds. *J. Memb. Sci.* **2013**, *429*, 121–129. https://doi.org/10.1016/j.memsci.2012.11.022.

(89) Nghiem, L. D.; Schäfer, A. I.; Elimelech, M. Pharmaceutical Retention Mechanisms by Nanofiltration Membranes. *Environ. Sci. Technol.* **2005**, *39* (19), 7698–7705. https://doi.org/10.1021/es0507665.

(90) Zheng, K.; Li, S.; Chen, Z.; Chen, Y.; Hong, Y.; Lan, W. Highly Stable Graphene Oxide Composite Nanofiltration Membrane. *Nanoscale* **2021**, *13* (22), 10061–10066. https://doi.org/10.1039/d1nr01823j.

(91) Drioli, E.; Laganà, F.; Criscuoli, A.; Barbieri, G. Integrated Membrane Operations in Desalination Processes. *Desalination* **1999**, *122* (2–3), 141–145. https://doi.org/10.1016/S0011-9164(99)00034-X.

(92) Wen, X.; Ma, P.; Zhu, C.; He, Q.; Deng, X. Preliminary Study on Recovering Lithium Chloride from Lithium-Containing Waters by Nanofiltration. *Sep. Purif. Technol.* **2006**, *49* (3), 230–236. https://doi.org/10.1016/j.seppur.2005.10.004.

(93) Fievet, P. Donnan Effect. In *Encyclopedia of Membranes*; Drioli, E., Giorno, L., Eds.; Springer Berlin Heidelberg: Berlin, Heidelberg, 2015; pp 1–3. https://doi.org/10.1007/978-3-642-40872-4_1714-1.

(94) Somrani, A.; Hamzaoui, A. H.; Pontie, M. Study on Lithium Separation from Salt Lake Brines by Nanofiltration (NF) and Low Pressure Reverse Osmosis (LPRO). *Desalination* **2013**, *317*, 184–192. https://doi.org/10.1016/j.desal.2013.03.009.

(95) Li, W.; Shi, C.; Zhou, A.; He, X.; Sun, Y.; Zhang, J. A Positively Charged Composite Nanofiltration Membrane Modified by EDTA for LiCl/MgCl2 Separation. *Sep. Purif. Technol.* **2017**, *186*, 233–242. https://doi.org/10.1016/j.seppur.2017.05.044.

(96) Wu, H.; Lin, Y.; Feng, W.; Liu, T.; Wang, L.; Yao, H.; Wang, X. A Novel Nanofiltration Membrane with [MimAP][Tf2N] Ionic Liquid for Utilization of Lithium from Brines with High Mg2+/Li+ Ratio. *J. Memb. Sci.* **2020**, *603*, 117997.

https://doi.org/10.1016/j.memsci.2020.117997.

(97) Wu, M.-B.; Ye, H.; Zhu, Z.-Y.; Chen, G.-T.; Ma, L.-L.; Liu, S.-C.; Liu, L.; Yao, J.; Xu, Z.-K. Positively-Charged Nanofiltration Membranes Constructed via Gas/Liquid Interfacial Polymerization for Mg2+/Li+ Separation. *J. Memb. Sci.* **2022**, *644*, 119942. https://doi.org/10.1016/j.memsci.2021.119942.

(98) Xu, Y.; Peng, H.; Luo, H.; Zhang, Q.; Liu, Z.; Zhao, Q. High Performance Mg2+/Li+ Separation Membranes Modified by a Bis-Quaternary Ammonium Salt. *Desalination* **2022**, *526*, 115519. https://doi.org/10.1016/j.desal.2021.115519.

(99) Zhao, Y.; Li, N.; Shi, J.; Xia, Y.; Zhu, B.; Shao, R.; Min, C.; Xu, Z.; Deng, H. Extra-Thin Composite Nanofiltration Membranes Tuned by γ-Cyclodextrins Containing Amphipathic Cavities for Efficient Separation of Magnesium/Lithium Ions. *Sep. Purif. Technol.* **2022**, 120419. https://doi.org/10.1016/j.seppur.2021.120419.

(100) Wang, L.; Rehman, D.; Sun, P.-F.; Deshmukh, A.; Zhang, L.; Han, Q.; Yang, Z.; Wang, Z.; Park, H.-D.; Lienhard, J. H.; Tang, C. Y. Novel Positively Charged Metal-Coordinated Nanofiltration Membrane for Lithium Recovery. *ACS Appl. Mater. Interfaces* **2021**, *13* (14), 16906–16915. https://doi.org/10.1021/acsami.1c02252.

(101) Peng, H.; Zhao, Q. A Nano-Heterogeneous Membrane for Efficient Separation of Lithium from High Magnesium / Lithium Ratio Brine. *Adv. Funct. Mater.* **2021**, *2009430*, 1–7. https://doi.org/10.1002/adfm.202009430.

(102) Bi, Q.; Zhang, C.; Liu, J.; Liu, X.; Xu, S. Positively Charged Zwitterion-Carbon Nitride Functionalized Nanofiltration Membranes with Excellent Separation Performance of Mg2+/Li+ and Good Antifouling Properties. *Sep. Purif. Technol.* **2021**, *257*, 117959. https://doi.org/10.1016/j.seppur.2020.117959.

(103) Curcio, E.; Criscuoli, A.; Drioli, E. Membrane Crystallizers. *Ind. Eng. Chem. Res.* **2001**, *40* (12), 2679–2684. https://doi.org/10.1021/ie000906d.

(104) Quist-Jensen, C. A.; Ali, A.; Mondal, S.; Macedonio, F.; Drioli, E. A Study of Membrane Distillation and Crystallization for Lithium Recovery from High-Concentrated Aqueous Solutions. *J. Memb. Sci.* **2016**, *505*, 167–173. https://doi.org/10.1016/j.memsci.2016.01.033.

(105) Park, S. H.; Kim, J. H.; Moon, S. J.; Jung, J. T.; Wang, H. H.; Ali, A.; Quist-Jensen, C. A.; Macedonio, F.; Drioli, E.; Lee, Y. M. Lithium Recovery from Artificial Brine Using Energy-Efficient Membrane Distillation and Nanofiltration. *J. Memb. Sci.* **2020**, *598*, 117683. https://doi.org/10.1016/j.memsci.2019.117683.

(106) Steward, D. G.; Waddan, D. Y.; Borrows, E. T. Improvements in and Relating to the Production of Alkylene Oxide Polymers. 785229A, 1957.

(107) Pedersen, C. J. Cyclic Polyethers and Their Complexes with Metal Salts. *J. Am.*

Chem. Soc. **1967**, *89* (26), 7017–7036. https://doi.org/10.1021/ja01002a035.

(108) Kitazawa, S.; Kimura, K.; Yano, H.; Shono, T. Lipophilic Crown-4 Derivatives as Lithium Ionophores. *J. Am. Chem. Soc.* **1984**, *106* (23), 6978–6983. https://doi.org/10.1021/ja00335a019.

(109) Kimura, K.; Tanaka, M.; Kitazawa. Highly Lithium-Selective Crown Ether Dyes for Extraction Photometry. *Chem. Lett.* **1985**, 1239–1240.

(110) Kimura, K.; Oishi, H.; Miura, T.; Shono, T. Lithium Ion Selective Electrodes Based on Crown Ethers for Serum Lithium Assay. *Anal. Chem.* **1987**, *59* (19), 2331–2334. https://doi.org/10.1021/ac00146a004.

(111) Arnold, K. A.; Mallen, J.; Trafton, J. E.; White, B. D.; Fronczek, F. R.; Gehrig, L. M.; Gandour, R. D.; Gokel, G. W. Ring-Side-Arm Cooperativity in Cation Inclusion Complexes of 12-Membered Ring Lariat Ethers: Effect of Side-Arm Chain Length and a Clarification of Long-Side-Arm Binding Strengths. *J. Org. Chem* **1988**, *53*, 5652–5657.

(112) Tsukube, H. Armed Crown Ether Complexes in Supramolecular Assembly. *Coord. Chem. Rev.* **1996**, *148*, 1–17. https://doi.org/10.1016/0010-8545(95)01151-X.

(113) Xu, J.; Pu, Z.; Xu, X.; Wang, Y.; Yang, D.; Zhang, T.; Qiu, F. Simultaneous Adsorption of Li(I) and Rb(I) by Dual Crown Ethers Modified Magnetic Ion Imprinting Polymers. *Appl. Organomet. Chem.* **2019**, *33* (3), e4778. https://doi.org/10.1002/aoc.4778.

(114) Zofchak, E. S.; Zhang, Z.; Wheatle, B. K.; Sujanani, R.; Warnock, S. J.; Dilenschneider, T. J.; Hanson, K. G.; Zhao, S.; Mukherjee, S.; Abu-Omar, M. M.; Bates, C. M.; Freeman, B. D.; Ganesan, V. Origins of Lithium/Sodium Reverse Permeability Selectivity in 12-Crown-4-Functionalized Polymer Membranes. *ACS Macro Lett.* **2021**, *19*, 1167–1173. https://doi.org/10.1021/acsmacrolett.1c00243.

(115) Kazemabad, M.; Verliefde, A.; Cornelissen, E. R.; D'Haese, A. Crown Ether Containing Polyelectrolyte Multilayer Membranes for Lithium Recovery. *J. Memb. Sci.* **2020**, *595* (September 2019), 117432. https://doi.org/10.1016/j.memsci.2019.117432.

(116) Hangarge, R. V; Duong Duc, L.; Boguslavsky, M.; Jones, L. A.; Yong Kim, S.; Bhosale, S. V. An Aza-12-Crown-4 Ether-Substituted Naphthalene Diimide Chemosensor for the Detection of Lithium Ion. *Chem. Sel.* **2017**, *2*, 11487–11491. https://doi.org/10.1002/slct.201702085.

(117) Li, H.; Wang, Y.; Li, T.; Ren, X.-K.; Wang, J.; Wang, Z.; Zhao, S. Nanofiltration Membrane with Crown Ether as Exclusive Li+ Transport Channels Achieving Efficient Extraction of Lithium from Salt Lake Brine. *Chem. Eng. J.* **2022**, *438*, 135658. https://doi.org/10.1016/j.cej.2022.135658.

(118) Zhou, M.; Yang, G.; Tian, X.; Xue, S.; Li, H.; Pan, J. Selective Capture of Lithium on Crown Ether Functionalized Hybrid Polymer Nanosheets Prepared by One-Step Emulsified Pickering O/W/O Double Emulsion Droplet Reactors. *J. Environ. Chem. Eng.* **2021**, 106997. https://doi.org/10.1016/j.jece.2021.106997.

(119) Zheng, X.; Li, A.; Hua, J.; Zhang, Y.; Li, Z. Crown Ether Grafted Graphene Oxide/Chitosan/Polyvinyl Alcohol Nanofiber Membrane for Highly Selective Adsorption and Separation of Lithium Ion. *Nanomaterials* **2021**, *11* (10), 2668. https://doi.org/10.3390/NANO11102668.

(120) Cheng, Q.; Zhang, Y.; Zheng, X.; Sun, W.; Li, B. T.; Wang, D.; Li, Z. High Specific Surface Crown Ether Modified Chitosan Nanofiber Membrane by Low-Temperature Phase Separation for Efficient Selective Adsorption of Lithium. *Sep. Purif. Technol.* **2021**, *262*, 118312. https://doi.org/10.1016/j.seppur.2021.118312.

(121) Luo, X.; Guo, B.; Luo, J.; Deng, F.; Zhang, S.; Luo, S.; Crittenden, J. Recovery of Lithium from Wastewater Using Development of Li Ion-Imprinted Polymers. *ACS Sustain. Chem. Eng.* **2015**, *3* (3), 460–467. https://doi.org/10.1021/sc500659h.

(122) Lu, J.; Qin, Y.; Zhang, Q.; Wu, Y.; Cui, J.; Li, C.; Wang, L.; Yan, Y. Multilayered Ion-Imprinted Membranes with High Selectivity towards Li + Based on the Synergistic Effect of 12-Crown-4 and Polyether Sulfone. *Appl. Surf. Sci.* **2018**, *427*, 931–941. https://doi.org/10.1016/j.apsusc.2017.08.016.

(123) Bai, X.; Dai, J.; Ma, Y.; Bian, W.; Pan, J. 2-(Allyloxy) Methylol-12-Crown-4 Ether Functionalized Polymer Brushes from Porous PolyHIPE Using UV-Initiated Surface Polymerization for Recognition and Recovery of Lithium. *Chem. Eng. J.* **2020**, *380*, 122386. https://doi.org/10.1016/j.cej.2019.122386.

(124) Zhao, H.; Liang, Q.; Yang, Y.; Liu, W.; Liu, X. Magnetic Graphene Oxide Surface Lithium Ion-Imprinted Material towards Lithium Extraction from Salt Lake. *Sep. Purif. Technol.* **2021**, *265*, 118513. https://doi.org/10.1016/j.seppur.2021.118513.

(125) Inoue, Y.; Hakushi, T.; Liu, Y.; Tong, L. H. Molecular Design of Crown Ethers. 12. Complexation Thermodynamics of 12- to 16-Crown-4: Thermodynamic Origin of High Lithium Selectivity of 14-Crown-4. *J. Org. Chem.* **1993**, *58* (20), 5411–5413. https://doi.org/10.1021/jo00072a024.

(126) Suzuki, K.; Yamada, H.; Sato, K.; Watanabe, K.; Hisamoto, H.; Tobe, Y.; Kobiro, K. Design and Synthesis of Highly Selective Ionophores for Lithium Ion Based on 14-Crown-4 Derivatives for an Ion-Selective Electrode. *Anal. Chem.* **1993**, *65* (23), 3404–3410. https://doi.org/10.1021/ac00071a012.

(127) Danil de Namor, A. F.; Ng, J. C. Y.; Llosa Tanco, M. A.; Salomon, M. Thermodynamics of Lithium−Crown Ether (12-Crown-4 and 1-Benzyl-1-Aza-12-Crown-4) Interactions in Acetonitrile and Propylene Carbonate. The Anion Effect on the Coordination Process. *J. Phys. Chem.* **1996**, *100* (34), 14485–14491. https://doi.org/10.1021/jp960519a.

(128) El-Azhary, A. A.; Al-Kahtani, A. A. Experimental and Theoretical Study of the Vibrational Spectra of Free 12-Crown-4. *J. Phys. Chem. A* **2005**, *109* (20), 4505–4511. https://doi.org/10.1021/jp050213g.

(129) Al-Rusaese, S.; Al-Kahtani, A. A.; El-Azhary, A. A. Experimental and Theoretical Study of the Vibrational Spectra of 12-Crown-4−Alkali Metal Cation Complexes. *J. Phys. Chem. A* **2006**, *110* (28), 8676–8687. https://doi.org/10.1021/jp062654l.

(130) Torrejos, R. E. C.; Nisola, G. M.; Song, H. S.; Limjuco, L. A.; Lawagon, C. P.; Parohinog, K. J.; Koo, S.; Han, J. W.; Chung, W.-J. Design of Lithium Selective Crown Ethers: Synthesis, Extraction and Theoretical Binding Studies. *Chem. Eng. J.* **2017**, *326*, 921–933. https://doi.org/10.1016/j.cej.2017.06.005.

(131) Xiong, Y.; Ge, T.; Xu, L.; Wang, L.; He, J.; Zhou, X.; Tian, Y.; Zhao, Z. A Fundamental Study on Selective Extraction of Li+ with Dibenzo-14-Crown-4 Ether: Toward New Technology Development for Lithium Recovery from Brines. *J. Environ. Manage.* **2022**, *310*, 114705. https://doi.org/10.1016/j.jenvman.2022.114705.

(132) Warnock, S. J.; Sujanani, R.; Zofchak, E. S.; Zhao, S.; Dilenschneider, T. J.; Hanson, K. G.; Mukherjee, S.; Ganesan, V.; Freeman, B. D.; Abu-Omar, M. M.; Bates, C. M. Engineering Li/Na Selectivity in 12-Crown-4–Functionalized Polymer Membranes. *Proc. Natl. Acad. Sci.* **2021**, *118* (37), e2022197118. https://doi.org/10.1073/pnas.2022197118.

(133) Sun, D.; Zhu, Y.; Meng, M.; Qiao, Y.; Yan, Y.; Li, C. Fabrication of Highly Selective Ion Imprinted Macroporous Membranes with Crown Ether for Targeted Separation of Lithium Ion. *Sep. Purif. Technol.* **2017**, *175*, 19–26. https://doi.org/10.1016/j.seppur.2016.11.029.

(134) Cui, J.; Zhang, Y.; Wang, Y.; Ding, J.; Yu, P.; Yan, Y.; Li, C.; Zhou, Z. Fabrication of Lithium Ion Imprinted Hybrid Membranes with Antifouling Performance for Selective Recovery of Lithium. *New J. Chem.* **2018**, *42* (1), 118–128. https://doi.org/10.1039/C7NJ03152A.

(135) Sun, D.; Meng, M.; Lu, Y.; Hu, B.; Yan, Y.; Li, C. Porous Nanocomposite Membranes Based on Functional GO with Selective Function for Lithium Adsorption. *New J. Chem.* **2018**, *42* (6), 4432–4442. https://doi.org/10.1039/C7NJ04733A.

(136) Park, M. J.; Nisola, G. M.; Vivas, E. L.; Limjuco, L. A.; Lawagon, C. P.; Seo, J. G.; Kim, H.; Shon, H. K.; Chung, W.-J. Mixed Matrix Nanofiber as a Flow-through Membrane Adsorber for Continuous Li + Recovery from Seawater. *J. Memb. Sci.* **2016**, *510*, 141–154. https://doi.org/10.1016/j.memsci.2016.02.062.

(137) Ma, J.; Ping, D.; Dong, X. Recent Developments of Graphene Oxide-Based Membranes: A Review. *Membranes (Basel).* **2017**, *7* (3), 52. https://doi.org/10.3390/membranes7030052.

(138) Abraham, J.; Vasu, K. S.; Williams, C. D.; Gopinadhan, K.; Su, Y.; Cherian, C. T.; Dix, J.; Prestat, E.; Haigh, S. J.; Grigorieva, I. V.; Carbone, P.; Geim, A. K.; Nair, R. R. Tunable Sieving of Ions Using Graphene Oxide Membranes. *Nat. Nanotechnol.* **2017**, *12* (6), 546–550. https://doi.org/10.1038/nnano.2017.21.

(139) Mi, B. Graphene Oxide Membranes for Ionic and Molecular Sieving. *Science (80-.).* **2014**, *343* (6172), 740–742. https://doi.org/10.1126/science.1250247.

(140) Joshi, R. K.; Carbone, P.; Wang, F. C.; Kravets, V. G.; Su, Y.; Grigorieva, I. V.; Wu, H. A.; Geim, A. K.; Nair, R. R. Precise and Ultrafast Molecular Sieving Through Graphene Oxide Membranes. *Science (80-.).* **2015**, *343* (6172), 752–754. https://doi.org/0.1126/science.1245711.

(141) Pedico, A.; Fontana, M.; Bianco, S.; Kara, S.; Periolatto, M.; Carminati, S.; Pirri, C. F.; Tresso, E.; Lamberti, A. Graphene Oxide Membranes for Trace Hydrocarbon Contaminant Removal from Aqueous Solution. *Nanomaterials* **2020**, *10* (11), 2242. https://doi.org/10.3390/nano10112242.

(142) Moghadam, F.; Park, H. B. 2D Nanoporous Materials: Membrane Platform for Gas and Liquid Separations. *2D Mater.* **2019**, *6* (4). https://doi.org/10.1088/2053-1583/ab1519.

(143) Liu, W.; Li, R.; Liu, J.; Ma, X.; Xiao, Y.; Wang, Y. Nacre-like Ultra-Robust Supramolecular-Functionalized Graphene Oxide Membrane for Bifunctional Separation. *Carbon N. Y.* **2021**, *184*, 618–626. https://doi.org/10.1016/j.carbon.2021.08.068.

(144) Li, M.; Li, Q.; Xu, M.; Liu, B.; Calatayud, D. G.; Wang, L.; Hu, Z.; James, T. D.; Mao, B. Amphiphilic Engineering of Reduced Graphene Oxides Using a Carbon Nitride Coating for Superior Removal of Organic Pollutants from Wastewater. *Carbon N. Y.* **2021**, *184*, 479–491. https://doi.org/10.1016/j.carbon.2021.08.045.

(145) Gu, Y.; Zhao, J.; Zhou, H.; Jiang, H.; Li, J.; Zhang, B.; Ma, H. Crosslinking Imidazolium-Intercalated GO Membrane for Acid Recovery from Low Concentration Solution. *Carbon N. Y.* **2021**, *183*, 830–839. https://doi.org/10.1016/j.carbon.2021.07.050.

(146) Han, Y.; Xu, Z.; Gao, C. Ultrathin Graphene Nanofiltration Membrane for Water Purification. *Adv. Funct. Mater.* **2013**, *23* (29), 3693–3700. https://doi.org/10.1002/adfm.201202601.

(147) Wei, Y.; Zhang, Y.; Gao, X.; Ma, Z.; Wang, X.; Gao, C. Multilayered Graphene Oxide Membrane for Water Treatment: A Review. *Carbon N. Y.* **2018**, *139* (238), 964–981. https://doi.org/10.1016/j.carbon.2018.07.040.

(148) Cohen-Tanugi, D.; Grossman, J. C. Water Desalination across Nanoporous Graphene. *Nano Lett.* **2012**, *12* (7), 3602–3608. https://doi.org/10.1021/nl3012853.

(149) Raza, A.; Hassan, J. Z.; Mahmood, A.; Nabgan, W.; Ikram, M. Recent Advances in Membrane-Enabled Water Desalination by 2D Frameworks: Graphene and Beyond. *Desalination* **2022**, *531*, 115684. https://doi.org/10.1016/j.desal.2022.115684.

(150) Perreault, F.; Fonseca de Faria, A.; Elimelech, M. Environmental Applications of Graphene-Based Nanomaterials. *Chem. Soc. Rev.* **2015**, *44* (16), 5861–5896. https://doi.org/10.1039/C5CS00021A.

(151) Bang, K. R.; Bahamon, D.; Vega, L. F.; Cho, E. S. Design of Sub-Nanochannels between Graphene Oxide Sheets via Crown Ether Intercalation to Selectively Regulate Cation Permeation. *Adv. Mater. Interfaces* **2020**, *7* (8), 1901876. https://doi.org/10.1002/admi.201901876.

(152) Ahmadi, H.; Hosseini, E.; Cha-Umpong, W.; Abdollahzadeh, M.; Korayem, A. H.; Razmjou, A.; Chen, V.; Asadnia, M. Incorporation of Natural Lithium-Ion Trappers into Graphene Oxide Nanosheets. *Adv. Mater. Technol.* **2020**, 2000665. https://doi.org/10.1002/admt.202000665.

(153) Nicolaï, A.; Sumpter, B. G.; Meunier, V. Tunable Water Desalination across Graphene Oxide Framework Membranes. *Phys. Chem. Chem. Phys.* **2014**, *16* (18), 8646. https://doi.org/10.1039/c4cp01051e.

(154) Lin, L.-C.; Grossman, J. C. Atomistic Understandings of Reduced Graphene Oxide as an Ultrathin-Film Nanoporous Membrane for Separations. *Nat. Commun.* **2015**, *6* (1), 8335. https://doi.org/10.1038/ncomms9335.

(155) Tsou, C. H.; An, Q. F.; Lo, S. C.; De Guzman, M.; Hung, W. S.; Hu, C. C.; Lee, K. R.; Lai, J. Y. Effect of Microstructure of Graphene Oxide Fabricated through Different Self-Assembly Techniques on 1-Butanol Dehydration. *J. Memb. Sci.* **2015**, *477*, 93–100. https://doi.org/10.1016/J.MEMSCI.2014.12.039.

(156) Ahmadi, H.; Hosseini, E.; Cha-Umpong, W.; Abdollahzadeh, M.; Korayem, A. H.; Razmjou, A.; Chen, V.; Asadnia, M.; Cha-Umpong, W.; Abdollahzadeh, M.; Korayem, A. H.; Razmjou, A.; Chen, V.; Asadnia, M. Incorporation of Natural Lithium-Ion Trappers into Graphene Oxide Nanosheets. *Adv. Mater. Technol.* **2020**, *2000665*, 1–12. https://doi.org/10.1002/admt.202000665.

(157) Ching, K.; Baker, A.; Tanaka, R.; Zhao, T.; Su, Z.; Ruoff, R. S.; Zhao, C.; Chen, X. Liquid-Phase Water Isotope Separation Using Graphene-Oxide Membranes. *Carbon N. Y.* **2021**. https://doi.org/10.1016/j.carbon.2021.10.009.

(158) Hu, M.; Mi, B. Enabling Graphene Oxide Nanosheets as Water Separation Membranes. *Environ. Sci. Technol.* **2013**, *47* (8), 3715–3723. https://doi.org/10.1021/es400571g.

(159) Devanathan, R.; Chase-Woods, D.; Shin, Y.; Gotthold, D. W. Molecular Dynamics Simulations Reveal That Water Diffusion between Graphene Oxide Layers Is Slow. *Sci. Rep.* **2016**, *6* (1), 29484. https://doi.org/10.1038/srep29484.

(160) Huang, H.; Song, Z.; Wei, N.; Shi, L.; Mao, Y.; Ying, Y.; Sun, L.; Xu, Z.; Peng, X. Ultrafast Viscous Water Flow through Nanostrand-Channelled Graphene Oxide Membranes. *Nat. Commun.* **2013**, *4* (1), 2979. https://doi.org/10.1038/ncomms3979.

(161) Huang, Y.; Li, H.; Wang, L.; Qiao, Y.; Tang, C.; Jung, C.; Yoon, Y.; Li, S.; Yu, M. Ultrafiltration Membranes with Structure-Optimized Graphene-Oxide Coatings for Antifouling Oil/Water Separation. *Adv. Mater. Interfaces* **2015**, *2* (2), 1400433. https://doi.org/10.1002/admi.201400433.

(162) Zinadini, S.; Vatanpour, V.; Zinatizadeh, A. A.; Rahimi, M.; Rahimi, Z.; Kian, M. Preparation and Characterization of Antifouling Graphene Oxide/Polyethersulfone Ultrafiltration Membrane: Application in MBR for Dairy Wastewater Treatment. *J. Water Process Eng.* **2015**, *7*, 280–294. https://doi.org/10.1016/j.jwpe.2015.07.005.

(163) Baudino, L.; Pedico, A.; Bianco, S.; Periolatto, M.; Pirri, C. F.; Lamberti, A. Crown-Ether Functionalized Graphene Oxide Membrane for Lithium Recovery from Water. *Membranes (Basel).* **2022**, *12* (2), 233. https://doi.org/10.3390/membranes12020233.

(164) Palagonia, M. S.; Brogioli, D.; La Mantia, F. Lithium Recovery from Diluted Brine by Means of Electrochemical Ion Exchange in a Flow-through-Electrodes Cell. *Desalination* **2020**, *475*, 114192. https://doi.org/10.1016/j.desal.2019.114192.

(165) Bryjak, M.; Siekierka, A.; Kujawski, J.; Smolińska-Kempisty, K. ìatarzyn.; Kujawski, W. Capacitive Deionization for Selective Extraction of Lithium from Aqueous Solutions. *J. Membr. Sep. Technol.* **2015**, *4* (3), 110–115. https://doi.org/10.6000/1929-6037.2015.04.03.2.

(166) Ryu, T.; Ryu, J. C.; Shin, J.; Lee, D. H.; Kim, Y. H.; Chung, K.-S. Recovery of Lithium by an Electrostatic Field-Assisted Desorption Process. *Ind. Eng. Chem. Res.* **2013**, *52* (38), 13738–13742. https://doi.org/10.1021/ie401977s.

(167) Ryu, T.; Lee, D.-H.; Ryu, J. C.; Shin, J.; Chung, K.-S.; Kim, Y. H. Lithium Recovery System Using Electrostatic Field Assistance. *Hydrometallurgy* **2015**, *151*, 78–83. https://doi.org/10.1016/j.hydromet.2014.11.005.

(168) Barksdale, A. C.; Yoon, J.; Kwon, H. J.; Han, J. Refinement of Brine for Lithium Extraction Using Ion Concentration Polarization. *Sep. Purif. Technol.* **2022**, *282*, 120055. https://doi.org/10.1016/j.seppur.2021.120055.

(169) Kim, N.; Su, X.; Kim, C. Electrochemical Lithium Recovery System through the Simultaneous Lithium Enrichment via Sustainable Redox Reaction. *Chem. Eng. J.* **2021**, *420*, 127715. https://doi.org/10.1016/j.cej.2020.127715.

(170) Kanoh, H.; Ooi, K.; Miyai, Y.; Katoh, S. Selective Electroinsertion of Lithium. *Langmuir* **1991**, *7*, 1841–1842. https://doi.org/10.1021/la00057a002 (https://doi.org/10.1021/la00057a002).

(171) Kanoh, H.; Ooi, K.; Miyai, Y.; Katoh, S. Electrochemical Recovery of Lithium Ions in the Aqueous Phase. *Sep. Sci. Technol.* **1993**, *28* (1–3), 643–651. https://doi.org/10.1080/01496399308019512.

(172) Pasta, M.; Wessells, C. D.; Cui, Y.; La Mantia, F. A Desalination Battery. *Nano Lett.* **2012**, *12* (2), 839–843. https://doi.org/10.1021/nl203889e.

(173) Pasta, M.; Battistel, A.; La Mantia, F. Batteries for Lithium Recovery from Brines. *Energy Environ. Sci.* **2012**, *5* (11), 9487. https://doi.org/10.1039/c2ee22977c.

(174) Calvo, E. J. Direct Lithium Recovery from Aqueous Electrolytes with Electrochemical Ion Pumping and Lithium Intercalation. *ACS Omega* **2021**, *6* (51), 35213–35220. https://doi.org/10.1021/acsomega.1c05516.

(175) Lee, J.; Yu, S.-H.; Kim, C.; Sung, Y.-E.; Yoon, J. Highly Selective Lithium Recovery from Brine Using a λ-MnO 2-Ag Battery. *Phys. Chem. Chem. Phys.* **2013**, *15* (20), 7690–7695. https://doi.org/10.1039/c3cp50919b.

(176) Zhao, A.; Liu, J.; Ai, X.; Yang, H.; Cao, Y. Highly Selective and Pollution-Free Electrochemical Extraction of Lithium by a Polyaniline/Li x Mn 2 O 4 Cell. *ChemSusChem* **2019**, *12* (7), 1361–1367. https://doi.org/10.1002/cssc.201803045.

(177) Marchini, F.; Williams, F. J.; Calvo, E. J. Sustainable Selective Extraction of Lithium Chloride from Natural Brine Using a Li1-XMn2O4 Ion Pump. *J. Electrochem. Soc.* **2018**, *165* (14), A3292–A3298. https://doi.org/10.1149/2.0291814jes.

(178) Zhao, X.; Yang, H.; Wang, Y.; Yang, L.; Zhu, L. Lithium Extraction from Brine by an Asymmetric Hybrid Capacitor Composed of Heterostructured Lithium-Rich Cathode and Nano-Bismuth Anode. *Sep. Purif. Technol.* **2021**, *274*, 119078. https://doi.org/10.1016/j.seppur.2021.119078.

(179) Niu, J.; Yan, W.; Song, X.; Ji, W.; Wang, Z.; Hao, X.; Guan, G. An Electrically Switched Ion Exchange System with Self-Electrical-Energy Recuperation for Efficient and Selective LiCl Separation from Brine Lakes. *Sep. Purif. Technol.* **2021**, *274*, 118995. https://doi.org/10.1016/j.seppur.2021.118995.

(180) Marchini, F.; Rubi, D.; Del Pozo, M.; Williams, F. J.; Calvo, E. J. Surface Chemistry and Lithium-Ion Exchange in LiMn2O4 for the Electrochemical Selective Extraction of LiCl from Natural Salt Lake Brines. *J. Phys. Chem. C* **2016**, *120* (29), 15875–15883. https://doi.org/10.1021/acs.jpcc.5b11722.

(181) Marchini, F.; Calvo, E. J.; Williams, F. J. Effect of the Electrode Potential on the Surface Composition and Crystal Structure of LiMn2O4 in Aqueous Solutions. *Electrochim. Acta* **2018**, *269*, 706–713. https://doi.org/10.1016/j.electacta.2018.02.108.

(182) Missoni, L. L.; Marchini, F.; del Pozo, M.; Calvo, E. J. A LiMn2O4-Polypyrrole

System for the Extraction of LiCl from Natural Brine. *J. Electrochem. Soc.* **2016**, *163* (9), A1898–A1902. https://doi.org/10.1149/2.0591609jes.

(183) Padhi, A. K. Phospho-Olivines as Positive-Electrode Materials for Rechargeable Lithium Batteries. *J. Electrochem. Soc.* **1997**, *144* (4), 1188. https://doi.org/10.1149/1.1837571.

(184) La Mantia, F.; Pasta, M.; Deshazer, H. D.; Logan, B. E.; Cui, Y. Batteries for Efficient Energy Extraction from a Water Salinity Difference. *Nano Lett.* **2011**, *11* (4), 1810–1813. https://doi.org/10.1021/nl200500s.

(185) Trócoli, R.; Battistel, A.; La Mantia, F. Selectivity of a Lithium-Recovery Process Based on LiFePO4. *Chem. - A Eur. J.* **2014**, *20* (32), 9888–9891. https://doi.org/10.1002/chem.201403535.

(186) Zhao, Z.; Si, X.; Liu, X.; He, L.; Liang, X. Li Extraction from High Mg/Li Ratio Brine with LiFePO4/FePO4 as Electrode Materials. *Hydrometallurgy* **2013**, *133*, 75–83. https://doi.org/10.1016/j.hydromet.2012.11.013.

(187) Trócoli, R.; Erinmwingbovo, C.; La Mantia, F. Optimized Lithium Recovery from Brines by Electrochemical Ion Pumping Technology Based on λ-MnO2 and NiHCF. *ChemElectroChem* **2017**, *4* (1), 143–149. https://doi.org/10.1002/celc.201600509.

(188) Kim, S.; Kang, J. S.; Joo, H.; Sung, Y.-E.; Yoon, J. Understanding the Behaviors of λ-MnO2in Electrochemical Lithium Recovery: Key Limiting Factors and a Route to the Enhanced Performance. *Environ. Sci. Technol.* **2020**, *54* (14), 9044–9051. https://doi.org/10.1021/acs.est.9b07646.

(189) Marchini, F.; Williams, F. J.; Calvo, E. J. Electrochemical Impedance Spectroscopy Study of the LixMn2O4 Interface with Natural Brine. *J. Electroanal. Chem.* **2018**, *819*, 428–434. https://doi.org/10.1016/j.jelechem.2017.11.071.

(190) Xu, X.; Zhou, Y.; Feng, Z.; Kahn, N. U.; Haq Khan, Z. U.; Tang, Y.; Sun, Y.; Wan, P.; Chen, Y.; Fan, M. A Self-Supported λ-MnO2 Film Electrode Used for Electrochemical Lithium Recovery from Brines. *Chempluschem* **2018**, *83* (6), 521–528. https://doi.org/10.1002/cplu.201800185.

(191) Zhao, M.-Y.; Ji, Z.-Y.; Zhang, Y.-G.; Guo, Z.-Y.; Zhao, Y.-Y.; Liu, J.; Yuan, J.-S. Study on Lithium Extraction from Brines Based on LiMn2O4/Li1-XMn2O4 by Electrochemical Method. *Electrochim. Acta* **2017**, *252*, 350–361. https://doi.org/10.1016/j.electacta.2017.08.178.

(192) Guo, Z.-Y.; Ji, Z.-Y.; Wang, J.; Chen, H.-Y.; Liu, J.; Zhao, Y.-Y.; Li, F.; Yuan, J.-S. Development of Electrochemical Lithium Extraction Based on a Rocking Chair System of LiMn2O4/Li1-XMn2O4: Self-Driven plus External Voltage Driven. *Sep. Purif. Technol.* **2021**, *259*, 118154. https://doi.org/10.1016/j.seppur.2020.118154.

(193) Blair, J. W.; Murphy, G. W. Electrochemical Demineralization of Water with Porous Electrodes of Large Surface Area. In *Saline Water conversion*; American Chemical Society, 1960; Vol. 27, pp 206–223. https://doi.org/10.1021/ba-1960-0027.ch020.

(194) Zhang, X.; Zuo, K.; Zhang, X.; Zhang, C.; Liang, P. Selective Ion Separation by Capacitive Deionization (CDI) Based Technologies: A State-of-the-Art Review. *Environ. Sci. Water Res. Technol.* **2020**, *6* (2), 243–257. https://doi.org/10.1039/c9ew00835g.

(195) Lee, J.-B.; Park, K.-K.; Eum, H.-M.; Lee, C.-W. Desalination of a Thermal Power Plant Wastewater by Membrane Capacitive Deionization. *Desalination* **2006**, *196* (1–3), 125–134. https://doi.org/10.1016/j.desal.2006.01.011.

(196) Biesheuvel, P. M.; van der Wal, A. Membrane Capacitive Deionization. *J. Memb. Sci.* **2010**, *346* (2), 256–262. https://doi.org/10.1016/j.memsci.2009.09.043.

(197) Lee, D. H.; Ryu, T.; Shin, J.; Ryu, J. C.; Chung, K.-S.; Kim, Y. H. Selective Lithium Recovery from Aqueous Solution Using a Modified Membrane Capacitive Deionization System. *Hydrometallurgy* **2017**, *173*, 283–288. https://doi.org/10.1016/j.hydromet.2017.09.005.

(198) Shi, W.; Liu, X.; Ye, C.; Cao, X.; Gao, C.; Shen, J. Efficient Lithium Extraction by Membrane Capacitive Deionization Incorporated with Monovalent Selective Cation Exchange Membrane. *Sep. Purif. Technol.* **2019**, *210* (July 2018), 885–890. https://doi.org/10.1016/j.seppur.2018.09.006.

(199) Ha, Y.; Jung, H. Bin; Lim, H.; Jo, P. S.; Yoon, H.; Yoo, C.-Y.; Pham, T. K.; Ahn, W.; Cho, Y. Continuous Lithium Extraction from Aqueous Solution Using Flow-Electrode Capacitive Deionization. *Energies* **2019**, *12* (15), 2913. https://doi.org/10.3390/en12152913.

(200) Siekierka, A.; Kujawa, J.; Kujawski, W.; Bryjak, M. Lithium Dedicated Adsorbent for the Preparation of Electrodes Useful in the Ion Pumping Method. *Sep. Purif. Technol.* **2018**, *194*, 231–238. https://doi.org/10.1016/j.seppur.2017.11.045.

(201) Siekierka, A.; Tomaszewska, B.; Bryjak, M. Lithium Capturing from Geothermal Water by Hybrid Capacitive Deionization. *Desalination* **2018**, *436*, 8–14. https://doi.org/10.1016/j.desal.2018.02.003.

(202) Tang, W.; Liang, J.; He, D.; Gong, J.; Tang, L.; Liu, Z.; Wang, D.; Zeng, G. Various Cell Architectures of Capacitive Deionization: Recent Advances and Future Trends. *Water Research*. Elsevier Ltd 2019, pp 225–251. https://doi.org/10.1016/j.watres.2018.11.064.

(203) Lee, J.; Kim, S.; Kim, C.; Yoon, J. Hybrid Capacitive Deionization to Enhance the Desalination Performance of Capacitive Techniques. *Energy Environ. Sci.* **2014**, *7* (11), 3683–3689. https://doi.org/10.1039/c4ee02378a.

(204) Kim, S.; Lee, J.; Kang, J. S.; Jo, K.; Kim, S.; Sung, Y. E.; Yoon, J. Lithium Recovery from Brine Using a λ-MnO2/Activated Carbon Hybrid Supercapacitor System. *Chemosphere* **2015**, *125*, 50–56. https://doi.org/10.1016/j.chemosphere.2015.01.024.

(205) Parsa, N.; Moheb, A.; Mehrabani-Zeinabad, A.; Masigol, M. A. Recovery of Lithium Ions from Sodium-Contaminated Lithium Bromide Solution by Using Electrodialysis Process. *Chem. Eng. Res. Des.* **2015**, *98*, 81–88. https://doi.org/10.1016/j.cherd.2015.03.025.

(206) Guo, Z.-Y.; Ji, Z.-Y.; Chen, Q.-B.; Liu, J.; Zhao, Y.-Y.; Li, F.; Liu, Z.-Y.; Yuan, J.-S. Prefractionation of LiCl from Concentrated Seawater/Salt Lake Brines by Electrodialysis with Monovalent Selective Ion Exchange Membranes. *J. Clean. Prod.* **2018**, *193*, 338–350. https://doi.org/10.1016/j.jclepro.2018.05.077.

(207) Nie, X. Y.; Sun, S. Y.; Sun, Z.; Song, X.; Yu, J. G. Ion-Fractionation of Lithium Ions from Magnesium Ions by Electrodialysis Using Monovalent Selective Ion-Exchange Membranes. *Desalination* **2017**, *403*, 128–135. https://doi.org/10.1016/j.desal.2016.05.010.

(208) Nie, X. Y.; Sun, S. Y.; Song, X.; Yu, J. G. Further Investigation into Lithium Recovery from Salt Lake Brines with Different Feed Characteristics by Electrodialysis. *J. Memb. Sci.* **2017**, *530*, 185–191. https://doi.org/10.1016/j.memsci.2017.02.020.

(209) Hoshino, T. Development of Technology for Recovering Lithium from Seawater by Electrodialysis Using Ionic Liquid Membrane. *Fusion Eng. Des.* **2013**, *88* (11), 2956–2959. https://doi.org/10.1016/j.fusengdes.2013.06.009.

(210) Hoshino, T. Preliminary Studies of Lithium Recovery Technology from Seawater by Electrodialysis Using Ionic Liquid Membrane. *Desalination* **2013**, *317*, 11–16. https://doi.org/10.1016/j.desal.2013.02.014.

(211) Liu, G.; Zhao, Z.; He, L. Highly Selective Lithium Recovery from High Mg/Li Ratio Brines. *Desalination* **2020**, *474*, 114185. https://doi.org/10.1016/j.desal.2019.114185.

(212) Mani, K. N. Electrodialysis Water Splitting Technology. *J. Memb. Sci.* **1991**, *58* (2), 117–138. https://doi.org/10.1016/S0376-7388(00)82450-3.

(213) Bunani, S.; Kabay, N.; Bunani, S.; Arda, M.; Yoshizuka, K.; Nishihama, S.; Bunani, S. Effect of Process Conditions on Recovery of Lithium and Boron from Water Using Bipolar Membrane Electrodialysis (BMED). *Desalination* **2017**, *416*, 10–15. https://doi.org/10.1016/j.desal.2017.04.017.

(214) Bunani, S.; Yoshizuka, K.; Nishihama, S.; Arda, M.; Kabay, N. Application of Bipolar Membrane Electrodialysis (BMED) for Simultaneous Separation and Recovery of Boron and Lithium from Aqueous Solutions. *Desalination* **2017**, *424*,

37–44. https://doi.org/10.1016/j.desal.2017.09.029.

(215) İpekçi, D.; Altıok, E.; Bunani, S.; Yoshizuka, K.; Nishihama, S.; Arda, M.; Kabay, N. Effect of Acid-Base Solutions Used in Acid-Base Compartments for Simultaneous Recovery of Lithium and Boron from Aqueous Solution Using Bipolar Membrane Electrodialysis (BMED). *Desalination* **2018**, *448*, 69–75. https://doi.org/10.1016/j.desal.2018.10.001.

(216) Jarma, Y. A.; Çermikli, E.; İpekçi, D.; Altıok, E.; Kabay, N. Comparison of Two Electrodialysis Stacks Having Different Ion Exchange and Bipolar Membranes for Simultaneous Separation of Boron and Lithium from Aqueous Solution. *Desalination* **2021**, *500*, 114850. https://doi.org/10.1016/j.desal.2020.114850.

(217) Li, Z.; Wang, S.; Wu, J.; Zhou, W. Recent Progress in Defective TiO2 Photocatalysts for Energy and Environmental Applications. *Renew. Sustain. Energy Rev.* **2022**, *156*, 111980. https://doi.org/10.1016/j.rser.2021.111980.

(218) Yang, Z.; Choi, D.; Kerisit, S.; Rosso, K. M.; Wang, D.; Zhang, J.; Graff, G.; Liu, J. Nanostructures and Lithium Electrochemical Reactivity of Lithium Titanites and Titanium Oxides: A Review. *J. Power Sources* **2009**, *192* (2), 588–598. https://doi.org/10.1016/j.jpowsour.2009.02.038.

(219) Zhang, Y.; Jiang, Z.; Huang, J.; Lim, L. Y.; Li, W.; Deng, J.; Gong, D.; Tang, Y.; Lai, Y.; Chen, Z. Titanate and Titania Nanostructured Materials for Environmental and Energy Applications: A Review. *RSC Adv.* **2015**, *5* (97), 79479–79510. https://doi.org/10.1039/C5RA11298B.

(220) Roy, P.; Berger, S.; Schmuki, P. TiO2 Nanotubes: Synthesis and Applications. *Angew. Chemie Int. Ed.* **2011**, *50* (13), 2904–2939. https://doi.org/10.1002/anie.201001374.

(221) Marchand, R.; Brohan, L.; Tournoux, M. TiO2(B) a New Form of Titanium Dioxide and the Potassium Octatitanate K2Ti8O17. *Mater. Res. Bull.* **1980**, *15* (8), 1129–1133. https://doi.org/10.1016/0025-5408(80)90076-8.

(222) Tournoux, M.; Marchand, R.; Brohan, L. Layered K2Ti4O9 and the Open Metastable TiO2(B) Structure. *Prog. Solid State Chem.* **1986**, *17* (1), 33–52. https://doi.org/10.1016/0079-6786(86)90003-8.

(223) Vittadini, A.; Casarin, M.; Selloni, A. Structure and Stability of TiO2-B Surfaces: A Density Functional Study. *J. Phys. Chem. C* **2009**, *113* (44), 18973–18977. https://doi.org/10.1021/jp9073009.

(224) Zhang, H.; Banfield, J. F. Understanding Polymorphic Phase Transformation Behavior during Growth of Nanocrystalline Aggregates: Insights from TiO2. *J. Phys. Chem. B* **2000**, *104* (15), 3481–3487. https://doi.org/10.1021/jp000499j.

(225) Lazzeri, M.; Vittadini, A.; Selloni, A. Structure and Energetics of Stoichiometric

TiO2 Anatase Surfaces. *Phys. Rev. B* **2001**, *63* (15), 155409. https://doi.org/10.1103/PhysRevB.63.155409.

(226) Nuspl, G.; Yoshizawa, K.; Yamabe, T. Lithium Intercalation in TiO2 Modifications. *J. Mater. Chem.* **1997**, *7* (12), 2529–2536. https://doi.org/10.1039/a703935b.

(227) Lee, D.-H.; Lee, B.-H.; Sinha, A. K.; Park, J.-H.; Kim, M.; Park, J.; Shin, H.; Lee, K.; Sung, Y.; Hyeon, T. Engineering Titanium Dioxide Nanostructures for Enhanced Lithium-Ion Storage. *J. Am. Chem. Soc.* **2018**, *140* (48), 16676–16684. https://doi.org/10.1021/jacs.8b09487.

(228) Madian, M.; Eychmüller, A.; Giebeler, L. Current Advances in TiO2-Based Nanostructure Electrodes for High Performance Lithium Ion Batteries. *Batteries* **2018**, *4* (7), 1–36. https://doi.org/10.3390/batteries4010007.

(229) van de Krol, R.; Goossens, A.; Schoonman, J. Spatial Extent of Lithium Intercalation in Anatase TiO2. *J. Phys. Chem. B* **1999**, No. 103, 7151–7159. https://doi.org/10.1021/jp9909964.

(230) Lindström, H.; Södergren, S.; Solbrand, A.; Rensmo, H.; Hjelm, J.; Hagfeldt, A.; Lindquist, S.-E. Li+ Ion Insertion in TiO2 (Anatase). 2. Voltammetry on Nanoporous Films. *J. Phys. Chem. B* **1997**, *101* (39), 7717–7722. https://doi.org/10.1021/jp970490q.

(231) Gentili, V.; Brutti, S.; Hardwick, L. J.; Armstrong, A. R.; Panero, S.; Bruce, P. G. Lithium Insertion into Anatase Nanotubes. *Chem. Mater.* **2012**, *24* (22), 4468–4476. https://doi.org/10.1021/cm302912f.

(232) Xiao, L.; Cao, M.; Mei, D.; Guo, Y.; Yao, L.; Qu, D.; Deng, B. Preparation and Electrochemical Lithium Storage Features of TiO2 Hollow Spheres. *J. Power Sources* **2013**, *238*, 197–202. https://doi.org/10.1016/j.jpowsour.2013.03.081.

(233) Wagemaker, M.; Borghols, W. J. H. H.; Mulder, F. M. Large Impact of Particle Size on Insertion Reactions. A Case for Anatase LixTiO2. *J. Am. Chem. Soc.* **2007**, *129* (14), 4323–4327. https://doi.org/10.1021/ja067733p.

(234) Zukalová, M.; Kalbáč, M.; Kavan, L.; Exnar, I.; Grätzel, M. Pseudocapacitive Lithium Storage in TiO 2 (B). *Chem. Mater.* **2005**, *17* (5), 1248–1255. https://doi.org/10.1021/cm048249t.

(235) Wittich, O.; Meyer, F.; Wark, M. Lithium Insertion into Mixed Phase Titania Nanotubes. *Zeitschrift fur Phys. Chemie* **2017**, *231* (7–8), 1407–1421. https://doi.org/10.1515/zpch-2016-0917.

(236) Yasuda, K.; Macak, J. M.; Berger, S.; Ghicov, A.; Schmuki, P. Mechanistic Aspects of the Self-Organization Process for Oxide Nanotube Formation on Valve Metals. *J. Electrochem. Soc.* **2007**, *154* (9), C472. https://doi.org/10.1149/1.2749091.

(237) Yasuda, K.; Schmuki, P. Control of Morphology and Composition of Self-Organized Zirconium Titanate Nanotubes Formed in (NH 4) 2 SO 4 /NH 4 F Electrolytes. *Electrochim. Acta* **2007**, *52*, 4053–4061. https://doi.org/10.1016/j.electacta.2006.11.023.

(238) Macak, J. M.; Hildebrand, H.; Marten-Jahns, U.; Schmuki, P. Mechanistic Aspects and Growth of Large Diameter Self-Organized TiO2 Nanotubes. *J. Electroanal. Chem.* **2008**, *621* (2), 254–266. https://doi.org/10.1016/j.jelechem.2008.01.005.

(239) Bauer, S.; Kleber, S.; Schmuki, P. TiO2 Nanotubes: Tailoring the Geometry in H3PO4/HF Electrolytes. *Electrochem. commun.* **2006**, *8* (8), 1321–1325. https://doi.org/10.1016/j.elecom.2006.05.030.

(240) Beranek, R.; Hildebrand, H.; Schmuki, P. Self-Organized Porous Titanium Oxide Prepared in H2SO4/HF Electrolytes. *Electrochem. Solid-State Lett.* **2003**, *6* (3), B12. https://doi.org/10.1149/1.1545192/XML.

(241) Song, Y.-Y.; Schmuki, P. Modulated TiO2 Nanotube Stacks and Their Use in Interference Sensors. *Electrochem. commun.* **2010**, *12* (4), 579–582. https://doi.org/10.1016/j.elecom.2010.02.004.

(242) Macak, J. M.; Tsuchiya, H.; Taveira, L.; Aldabergerova, S.; Schmuki, P. Smooth Anodic TiO2 Nanotubes. *Angew. Chemie Int. Ed.* **2005**, *44* (45), 7463–7465. https://doi.org/10.1002/anie.200502781.

(243) Albu, S. P.; Ghicov, A.; Macak, J. M.; Schmuki, P. 250 Mm Long Anodic TiO2 Nanotubes with Hexagonal Self-Ordering. *Phys. status solidi – Rapid Res. Lett.* **2007**, *1* (2), R65–R67. https://doi.org/10.1002/pssr.200600069.

(244) Zwilling, V.; Aucouturier, M.; Darque-Ceretti, E. Anodic Oxidation of Titanium and TA6V Alloy in Chromic Media. An Electrochemical Approach. *Electrochim. Acta* **1999**, *45* (6), 921–929. https://doi.org/10.1016/S0013-4686(99)00283-2.

(245) Gong, D.; Grimes, C. A.; Varghese, O. K.; Hu, W.; Singh, R. S.; Chen, Z.; Dickey, E. C. Titanium Oxide Nanotube Arrays Prepared by Anodic Oxidation. *J. Mater. Res.* **2001**, *16* (12), 3331–3334. https://doi.org/10.1557/JMR.2001.0457.

(246) Jen, H.-P.; Lin, M.-H.; Li, L.-L.; Wu, H.-P.; Huang, W.-K.; Cheng, P.-J.; Diau, E. W.-G. High-Performance Large-Scale Flexible Dye-Sensitized Solar Cells Based on Anodic TiO 2 Nanotube Arrays. *ACS Appl. Mater. Interfaces* **2013**, *5* (20), 10098–10104. https://doi.org/10.1021/am402687j.

(247) Ge, M.; Cao, C.; Huang, J.; Li, S.; Chen, Z.; Zhang, K. Q.; Al-Deyab, S. S.; Lai, Y. A Review of One-Dimensional TiO2 Nanostructured Materials for Environmental and Energy Applications. *J. Mater. Chem. A* **2016**, *4* (18), 6772–6801. https://doi.org/10.1039/c5ta09323f.

(248) Krbal, M.; Ng, S.; Motola, M.; Hromadko, L.; Dvorak, F.; Prokop, V.; Sopha, H.;

Macak, J. M. Sulfur Treated 1D Anodic TiO2 Nanotube Layers for Significant Photo- and Electroactivity Enhancement. *Appl. Mater. Today* **2019**, *17*, 104–111. https://doi.org/10.1016/j.apmt.2019.07.018.

(249) Dvorak, F.; Zazpe, R.; Krbal, M.; Sopha, H.; Prikryl, J.; Ng, S.; Hromadko, L.; Bures, F.; Macak, J. M. One-Dimensional Anodic TiO2 Nanotubes Coated by Atomic Layer Deposition: Towards Advanced Applications. *Appl. Mater. Today* **2019**, *14*, 1–20. https://doi.org/10.1016/j.apmt.2018.11.005.

(250) Kupferer, A.; Holm, A.; Lotnyk, A.; Mändl, S.; Mayr, S. G. Compositional Patterning in Carbon Implanted Titania Nanotubes. *Adv. Funct. Mater.* **2021**, *31* (35), 2104250. https://doi.org/10.1002/ADFM.202104250.

(251) Qiu, Z.; Wang, M.; Chen, Y.; Zhang, T.; Yang, D.; Qiu, F. Li4Mn5O12 Doped Cellulose Acetate Membrane with Low Mn Loss and High Stability for Enhancing Lithium Extraction from Seawater. *Desalination* **2021**, *506*, 115003. https://doi.org/10.1016/j.desal.2021.115003.

(252) Razzaboni, L.; Altomare, M.; Pedeferri, M.; Diamanti, M. V.; Schmuki, P. Hierarchical Anodic TiO2 Nanostructures Formed in Ethylene Glycol/o-H3PO4 Electrolytes for Direct Photocatalysis. *ChemElectroChem* **2020**, *7* (13), 2859–2863. https://doi.org/10.1002/CELC.202000673.

(253) Mohajernia, S.; Hejazi, S.; Andryskova, P.; Zoppellaro, G.; Tomanec, O.; Zboril, R.; Schmuki, P. Conductive Cu-Doped TiO2 Nanotubes for Enhanced Photoelectrochemical Methanol Oxidation and Concomitant Hydrogen Generation. *ChemElectroChem* **2019**, *6* (4), 1244–1249. https://doi.org/10.1002/CELC.201900076.

(254) Touni, A.; Liu, X.; Kang, X.; Carvalho, P. A.; Diplas, S.; Both, K. G.; Sotiropoulos, S.; Chatzitakis, A. Galvanic Deposition of Pt Nanoparticles on Black TiO2 Nanotubes for Hydrogen Evolving Cathodes. *ChemSusChem* **2021**, *14* (22), 4993–5003. https://doi.org/10.1002/CSSC.202101559.

(255) Abbas, W. A.; Abdullah, I. H.; Ali, B. A.; Ahmed, N.; Mohamed, A. M.; Rezk, M. Y.; Ismail, N.; Mohamed, M. A.; Allam, N. K. Recent Advances in the Use of TiO2 Nanotube Powder in Biological, Environmental, and Energy Applications. *Nanoscale Adv.* **2019**, *1* (8), 2801–2816. https://doi.org/10.1039/c9na00339h.

(256) Zhang, M.-M.; Chen, J.-Y.; Li, H.; Wang, C.-R. Recent Progress in Li-Ion Batteries with TiO2 Nanotube Anodes Grown by Electrochemical Anodization. *Rare Met.* **2021**, *40* (2), 249–271. https://doi.org/10.1007/s12598-020-01499-x.

(257) Kyerematen, N. A. Self-Organised TiO2 Nanotubes for 2D or 3D Li-Ion Microbatteries. *ChemElectroChem* **2014**, *1* (9), 1442–1466. https://doi.org/10.1002/CELC.201402109.

(258) Fu, Y.; Mo, A. A Review on the Electrochemically Self-Organized Titania

Nanotube Arrays: Synthesis, Modifications, and Biomedical Applications. *Nanoscale Res. Lett.* **2018**, *13*. https://doi.org/10.1186/s11671-018-2597-z.

(259) Nah, Y. C.; Paramasivam, I.; Schmuki, P. Doped TiO2 and TiO2 Nanotubes: Synthesis and Applications. *ChemPhysChem* **2010**, *11* (13), 2698–2713. https://doi.org/10.1002/CPHC.201000276.

(260) Liu, Y.; Yang, Y. Recent Progress of TiO 2 -Based Anodes for Li Ion Batteries. *J. Nanomater.* **2016**, *2016*, 1–15. https://doi.org/10.1155/2016/8123652.

(261) López, M. C.; Ortiz, G. F.; González, J. R.; Alcántara, R.; Tirado, J. L. Improving the Performance of Titania Nanotube Battery Materials by Surface Modification with Lithium Phosphate. *ACS Appl. Mater. Interfaces* **2014**, *6* (8), 5669–5678. https://doi.org/10.1021/AM500189H/SUPPL_FILE/AM500189H_SI_001.PDF.

(262) Pan, D.; Huang, H.; Wang, X.; Wang, L.; Liao, H.; Li, Z.; Wu, M. C-Axis Preferentially Oriented and Fully Activated TiO 2 Nanotube Arrays for Lithium Ion Batteries and Supercapacitors. *J. Mater. Chem. A* **2014**, *2* (29), 11454–11464. https://doi.org/10.1039/C4TA01613K.

(263) Brumbarov, J.; Vivek, J. P.; Leonardi, S.; Valero-Vidal, C.; Portenkirchner, E.; Kunze-Liebhäuser, J. Oxygen Deficient, Carbon Coated Self-Organized TiO2 Nanotubes as Anode Material for Li-Ion Intercalation. *J. Mater. Chem. A* **2015**, *3* (32), 16469–16477. https://doi.org/10.1039/c5ta03621f.

(264) Madian, M.; Giebeler, L.; Klose, M.; Jaumann, T.; Uhlemann, M.; Gebert, A.; Oswald, S.; Ismail, N.; Eychmüller, A.; Eckert, J. Self-Organized TiO 2 /CoO Nanotubes as Potential Anode Materials for Lithium Ion Batteries. *ACS Sustain. Chem. Eng.* **2015**, *3* (5), 909–919. https://doi.org/10.1021/acssuschemeng.5b00026.

(265) Wen, W.; Wu, J. M.; Jiang, Y. Z.; Bai, J. Q.; Lai, L. L. Titanium Dioxide Nanotrees for High-Capacity Lithium-Ion Microbatteries. *J. Mater. Chem. A* **2016**, *4* (27), 10593–10600. https://doi.org/10.1039/C6TA03331H.

(266) Zhang, M.; Yin, K.; Hood, Z. D.; Bi, Z.; Bridges, C. A.; Dai, S.; Meng, Y. S.; Paranthaman, M. P.; Chi, M. In Situ TEM Observation of the Electrochemical Lithiation of N-Doped Anatase TiO2 Nanotubes as Anodes for Lithium-Ion Batteries. *J. Mater. Chem. A* **2017**, *5* (39), 20651–20657. https://doi.org/10.1039/C7TA05877B.

(267) Salian, G. D.; Krbal, M.; Sopha, H.; Lebouin, C.; Coulet, M.-V.; Michalicka, J.; Hromadko, L.; Tesfaye, A. T.; Macak, J. M.; Djenizian, T. Self-Supported Sulphurized TiO2 Nanotube Layers as Positive Electrodes for Lithium Microbatteries. *Appl. Mater. Today* **2019**, *16*, 257–264. https://doi.org/10.1016/j.apmt.2019.05.015.

(268) Tian, T.; Lu, L.-L.; Yin, Y.-C.; Li, F.; Zhang, T.-W.; Song, Y.-H.; Tan, Y.-H.; Yao, H.-B. Multiscale Designed Niobium Titanium Oxide Anode for Fast Charging

Lithium Ion Batteries. *Adv. Funct. Mater.* **2021**, *31* (4), 2007419. https://doi.org/10.1002/ADFM.202007419.

(269) Lu, Y.; Wang, J.; Chen, Y.; Zheng, X.; Yao, H.; Mathur, S.; Hong, Z. Spatially Controlled Lithium Deposition on Silver-Nanocrystals-Decorated TiO2 Nanotube Arrays Enabling Ultrastable Lithium Metal Anode. *Adv. Funct. Mater.* **2021**, *31* (9), 2009605. https://doi.org/10.1002/ADFM.202009605.

(270) Auer, A.; Portenkirchner, E.; Götsch, T.; Valero-Vidal, C.; Penner, S.; Kunze-Liebhäuser, J. Preferentially Oriented TiO 2 Nanotubes as Anode Material for Li-Ion Batteries: Insight into Li-Ion Storage and Lithiation Kinetics. *ACS Appl. Mater. Interfaces* **2017**, *9* (42), 36828–36836. https://doi.org/10.1021/acsami.7b11388.

(271) Liu, X.; Carvalho, P.; Getz, M. N.; Norby, T.; Chatzitakis, A. Black Anatase TiO 2 Nanotubes with Tunable Orientation for High Performance Supercapacitors. *J. Phys. Chem. C* **2019**, *123* (36), 21931–21940. https://doi.org/10.1021/acs.jpcc.9b05070.

(272) Raj, C. C.; Srimurugan, V.; Flamina, A.; Prasanth, R. Tuning the Carrier Density of TiO2 Nanotube Arrays by Controlling the Oxygen Vacancies for Improved Areal Capacitance in Supercapacitor Applications. *Mater. Chem. Phys.* **2020**, *248*, 122925. https://doi.org/10.1016/j.matchemphys.2020.122925.

(273) Ding, J.; Hu, W.; Paek, E.; Mitlin, D. Review of Hybrid Ion Capacitors: From Aqueous to Lithium to Sodium. *Chem. Rev.* **2018**, *118* (14), 6457–6498. https://doi.org/10.1021/acs.chemrev.8b00116.

(274) Haetge, J.; Hartmann, P.; Brezesinski, K.; Janek, J.; Brezesinski, T. Ordered Large-Pore Mesoporous Li4Ti5O12 Spinel Thin Film Electrodes with Nanocrystalline Framework for High Rate Rechargeable Lithium Batteries: Relationships among Charge Storage, Electrical Conductivity, and Nanoscale Structure. *Chem. Mater.* **2011**, *23* (19), 4384–4393. https://doi.org/10.1021/CM202185Y/SUPPL_FILE/CM202185Y_SI_001.PDF.

(275) Ji, G.; Ma, Y.; Ding, B.; Lee, J. Y. Improving the Performance of High Capacity Li-Ion Anode Materials by Lithium Titanate Surface Coating. *Chem. Mater.* **2012**, *24* (17), 3329–3334. https://doi.org/10.1021/CM301432W/SUPPL_FILE/CM301432W_SI_001.PDF.

(276) Zou, K.; Deng, W.; Cai, P.; Deng, X.; Wang, B.; Liu, C.; Li, J.; Hou, H.; Zou, G.; Ji, X. Prelithiation/Presodiation Techniques for Advanced Electrochemical Energy Storage Systems: Concepts, Applications, and Perspectives. *Adv. Funct. Mater.* **2020**, *2005581*, 1–23. https://doi.org/10.1002/adfm.202005581.

(277) Wang, F.; Wang, B.; Li, J.; Wang, B.; Zhou, Y.; Wang, D.; Liu, H.; Dou, S. Prelithiation: A Crucial Strategy for Boosting the Practical Application of Next-Generation Lithium Ion Battery. *ACS Nano* **2021**, acsnano.0c10664. https://doi.org/10.1021/acsnano.0c10664.

(278) Jin, L.; Shen, C.; Wu, Q.; Shellikeri, A.; Zheng, J.; Zhang, C.; Zheng, J. P. Pre-Lithiation Strategies for Next-Generation Practical Lithium-Ion Batteries. *Adv. Sci.* **2021**, *8* (12), 2005031. https://doi.org/10.1002/advs.202005031.

(279) Hong, Z.; Wei, M. Layered Titanate Nanostructures and Their Derivatives as Negative Electrode Materials for Lithium-Ion Batteries. *J. Mater. Chem. A* **2013**, *1* (14), 4403–4414. https://doi.org/10.1039/C2TA01312F.

(280) Chauque, S.; Oliva, F. Y.; Visintin, A.; Barraco, D.; Leiva, E. P. M.; Cámara, O. R. Lithium Titanate as Anode Material for Lithium Ion Batteries: Synthesis, Post-Treatment and Its Electrochemical Response. *J. Electroanal. Chem.* **2017**, *799*, 142–155. https://doi.org/10.1016/j.jelechem.2017.05.052.

(281) Yi, T.-F.; Yang, S.-Y.; Xie, Y. Recent Advances of Li4Ti5O12 as a Promising next Generation Anode Material for High Power Lithium-Ion Batteries. *J. Mater. Chem. A* **2015**, *3* (11), 5750–5777. https://doi.org/10.1039/C4TA06882C.

(282) Limjuco, L. A.; Nisola, G. M.; Lawagon, C. P.; Lee, S. P.; Seo, J. G.; Kim, H.; Chung, W.-J. H2TiO3 Composite Adsorbent Foam for Efficient and Continuous Recovery of Li+ from Liquid Resources. *Colloids Surfaces A Physicochem. Eng. Asp.* **2016**, *504*, 267–279. https://doi.org/10.1016/j.colsurfa.2016.05.072.

(283) Nisola, G. M.; Limjuco, L. A.; Vivas, E. L.; Lawagon, C. P.; Park, M. J.; Shon, H. K.; Mittal, N.; Nah, I. W.; Kim, H.; Chung, W.-J. Macroporous Flexible Polyvinyl Alcohol Lithium Adsorbent Foam Composite Prepared via Surfactant Blending and Cryo-Desiccation. *Chem. Eng. J.* **2015**, *280*, 536–548. https://doi.org/10.1016/j.cej.2015.05.107.

(284) Ohzuku, T.; Ueda, A.; Yamamoto, N. Zero-Strain Insertion Material of Li [Li1 / 3Ti5 / 3] O 4 for Rechargeable Lithium Cells. *J. Electrochem. Soc.* **1995**, *142* (5), 1431–1435. https://doi.org/10.1149/1.2048592.

(285) Scharner, S.; Weppner, W.; Schmid-Beurmann, P. Evidence of Two-Phase Formation upon Lithium Insertion into the Li1.33Ti1.67 O 4 Spinel. *J. Electrochem. Soc.* **1999**, *146* (3), 857–861. https://doi.org/10.1149/1.1391692.

(286) Nakahira, A.; Kubo, T.; Numako, C. TiO 2 -Derived Titanate Nanotubes by Hydrothermal Process with Acid Treatments and Their Microstructural Evaluation. *ACS Appl. Mater. Interfaces* **2010**, *2* (9), 2611–2616. https://doi.org/10.1021/am1004442.

(287) Bavykin, D. V.; Friedrich, J. M.; Lapkin, A. A.; Walsh, F. C. Stability of Aqueous Suspensions of Titanate Nanotubes. *Chem. Mater.* **2006**, *18* (5), 1124–1129. https://doi.org/10.1021/cm0521875.

(288) Kim, G.-S.; Kim, Y.-S.; Seo, H.-K.; Shin, H.-S. Hydrothermal Synthesis of Titanate Nanotubes Followed by Electrodeposition Process. *Korean J. Chem. Eng.* **2006**, *23* (6), 1037–1045. https://doi.org/10.1007/s11814-006-0027-x.

(289) Lamberti, A.; Garino, N.; Bejtka, K.; Bianco, S.; Stassi, S.; Chiodoni, A.; Canavese, G.; Pirri, C. F.; Quaglio, M. Synthesis of Ferroelectric BaTiO3 Tube-like Arrays by Hydrothermal Conversion of a Vertically Aligned TiO2 Nanotube Carpet. *New J. Chem.* **2014**, *38* (5), 2024–2030. https://doi.org/10.1039/c3nj01138k.

(290) Muñoz-Tabares, J. A.; Bejtka, K.; Lamberti, A.; Garino, N.; Bianco, S.; Quaglio, M.; Pirri, C. F.; Chiodoni, A. Nanostructural Evolution of One-Dimensional BaTiO3 Structures by Hydrothermal Conversion of Vertically Aligned TiO2 Nanotubes. *Nanoscale* **2016**, *8* (12), 6866–6876. https://doi.org/10.1039/c5nr07283b.

(291) Zhang, L.; He, G.; Zhou, D.; Zhou, J.; Yao, Q. Study on Transformation Mechanism of Lithium Titanate Modified with Hydrochloric Acid. *Ionics (Kiel).* **2016**, *22* (11), 2007–2014. https://doi.org/10.1007/S11581-016-1742-X/TABLES/2.

(292) Chitrakar, R.; Makita, Y.; Ooi, K.; Sonoda, A. Lithium Recovery from Salt Lake Brine by H2TiO3. *Dalt. Trans.* **2014**, *43* (23), 8933–8939. https://doi.org/10.1039/C4DT00467A.

(293) Zhang, L.; Zhou, D.; He, G.; Wang, F.; Zhou, J. Effect of Crystal Phases of Titanium Dioxide on Adsorption Performance of H2TiO3-Lithium Adsorbent. *Mater. Lett.* **2014**, *135*, 206–209. https://doi.org/10.1016/j.matlet.2014.07.176.

(294) Lawagon, C. P.; Nisola, G. M.; Mun, J.; Tron, A.; Torrejos, R. E. C.; Seo, J. G.; Kim, H.; Chung, W.-J. Adsorptive Li+ Mining from Liquid Resources by H2TiO3: Equilibrium, Kinetics, Thermodynamics, and Mechanisms. *J. Ind. Eng. Chem.* **2016**, *35*, 347–356. https://doi.org/10.1016/j.jiec.2016.01.015.

(295) Ji, Z.-Y.; Yang, F.-J.; Zhao, Y.-Y.; Liu, J.; Wang, N.; Yuan, J.-S. Preparation of Titanium-Base Lithium Ionic Sieve with Sodium Persulfate as Eluent and Its Performance. *Chem. Eng. J.* **2017**, *328*, 768–775. https://doi.org/10.1016/j.cej.2017.07.047.

(296) Zhang, Q. H.; Li, S. P.; Sun, S. Y.; Yin, X. S.; Yu, J. G. Lithium Selective Adsorption on Low-Dimensional Titania Nanoribbons. *Chem. Eng. Sci.* **2010**, *65* (1), 165–168. https://doi.org/10.1016/j.ces.2009.06.001.

(297) Zhang, Y.; Liu, J.; Yang, Y.; Lin, S.; Li, P. Preparation of Granular Titanium-Type Lithium-Ion Sieves and Recyclability Assessment for Lithium Recovery from Brines with Different PH Value. *Sep. Purif. Technol.* **2021**, *267*, 118613. https://doi.org/10.1016/j.seppur.2021.118613.

(298) Hossain, S. M.; Ibrahim, I.; Choo, Y.; Razmjou, A.; Naidu, G.; Tijing, L.; Kim, J.-H.; Shon, H. K. Preparation of Effective Lithium-Ion Sieve from Sludge-Generated TiO2. *Desalination* **2022**, *525*, 115491. https://doi.org/10.1016/J.DESAL.2021.115491.

(299) Li, X.; Chen, L.; Chao, Y.; Chen, W.; Luo, J.; Xiong, J.; Zhu, F.; Chu, X.; Li, H.;

Zhu, W. Amorphous TiO 2 -Derived Large-Capacity Lithium Ion Sieve for Lithium Recovery. *Chem. Eng. Technol.* **2020**, *43* (9), 1784–1791. https://doi.org/10.1002/ceat.201900374.

(300) Liu, J.; Zhang, Y.; Miao, Y.; Yang, Y.; Li, P. Alkaline Resins Enhancing Li + /H + Ion Exchange for Lithium Recovery from Brines Using Granular Titanium-Type Lithium Ion-Sieves. *Ind. Eng. Chem. Res.* **2021**, *60* (45), 16457–16468. https://doi.org/10.1021/acs.iecr.1c02361.

(301) Zhu, X.; Yue, H.; Sun, W.; Zhang, L.; Cui, Q.; Wang, H. Study on Adsorption Extraction Process of Lithium Ion from West Taijinar Brine by Shaped Titanium-Based Lithium Ion Sieves. *Sep. Purif. Technol.* **2021**, *274*, 119099. https://doi.org/10.1016/j.seppur.2021.119099.

(302) Gu, D.; Sun, W.; Han, G.; Cui, Q.; Wang, H. Lithium Ion Sieve Synthesized via an Improved Solid State Method and Adsorption Performance for West Taijinar Salt Lake Brine. *Chem. Eng. J.* **2018**, *350*, 474–483. https://doi.org/10.1016/j.cej.2018.05.191.

(303) Wang, S.; Li, P.; Zhang, X.; Zheng, S.; Zhang, Y. Selective Adsorption of Lithium from High Mg-Containing Brines Using HxTiO3 Ion Sieve. *Hydrometallurgy* **2017**, *174*, 21–28. https://doi.org/10.1016/j.hydromet.2017.09.009.

(304) Zhang, L.; Zhou, D.; Yao, Q.; Zhou, J. Preparation of H2TiO3-Lithium Adsorbent by the Sol-Gel Process and Its Adsorption Performance. *Appl. Surf. Sci.* **2016**, *368*, 82–87. https://doi.org/10.1016/j.apsusc.2016.01.203.

(305) Zhang, L.; Zhou, D.; He, G.; Yao, Q.; Wang, F.; Zhou, J. Synthesis of H2TiO3–Lithium Adsorbent Loaded on Ceramic Foams. *Mater. Lett.* **2015**, *145*, 351–354. https://doi.org/10.1016/j.matlet.2015.01.142.

(306) Moazeni, M.; Hajipour, H.; Askari, M.; Nusheh, M. Hydrothermal Synthesis and Characterization of Titanium Dioxide Nanotubes as Novel Lithium Adsorbents. *Mater. Res. Bull.* **2015**, *61*, 70–75. https://doi.org/10.1016/j.materresbull.2014.09.069.

(307) Taghvaei, N.; Taghvaei, E.; Askari, M. Synthesis of Anodized TiO2 Nanotube Arrays as Ion Sieve for Lithium Extraction. *ChemistrySelect* **2020**, *5* (33), 10339–10345. https://doi.org/10.1002/slct.202002222.

(308) Baudino, L.; Zaccagnini, P.; Garino, N.; Serrapede, M.; Laurenti, M.; Pedico, A.; Pirri, C. F.; Lamberti, A. Stable and Reversible Lithium Storage Properties of LiTiO x Nanotubes for Electrochemical Recovery from Aqueous Solutions. *ChemElectroChem* **2022**, *9* (10). https://doi.org/10.1002/celc.202101652.

(309) Lamberti, A.; Garino, N.; Sacco, A.; Bianco, S.; Chiodoni, A.; Gerbaldi, C. As-Grown Vertically Aligned Amorphous TiO2 Nanotube Arrays as High-Rate Li-Based Micro-Battery Anodes with Improved Long-Term Performance.

Electrochim. Acta **2015**, *151*, 222–229. https://doi.org/10.1016/j.electacta.2014.10.150.

(310) Lamberti, A.; Chiodoni, A.; Shahzad, N.; Bianco, S.; Quaglio, M.; Pirri, C. F. Ultrafast Room-Temperature Crystallization of TiO2 Nanotubes Exploiting Water-Vapor Treatment. *Sci. Rep.* **2015**, *5* (1), 7808. https://doi.org/10.1038/srep07808.

(311) Wu, J.-B.; Lin, M.-L.; Cong, X.; Liu, H.-N.; Tan, P.-H. Raman Spectroscopy of Graphene-Based Materials and Its Applications in Related Devices. *Chem. Soc. Rev.* **2018**, 1822–1873. https://doi.org/10.1039/C6CS00915H.

(312) Pletcher, D. *A First Course in Electrode Processes*, Second Edi.; RSC Publishing: Cambridge, 2009.

(313) Bockris, J. O.; Reddy, A. K. N.; Gamboa-Aldeco, M. *Modern Electrochemistry 2A*, Second Edi.; Kluwer Academic Publishers, 2000.

(314) Elgrishi, N.; Rountree, K. J.; McCarthy, B. D.; Rountree, E. S.; Eisenhart, T. T.; Dempsey, J. L. A Practical Beginner's Guide to Cyclic Voltammetry. *J. Chem. Educ.* **2018**, *95* (2), 197–206. https://doi.org/10.1021/acs.jchemed.7b00361.

(315) Fleischmann, S.; Mitchell, J. B.; Wang, R.; Zhan, C.; Jiang, D. E.; Presser, V.; Augustyn, V. Pseudocapacitance: From Fundamental Understanding to High Power Energy Storage Materials. *Chem. Rev.* **2020**, *120* (14), 6738–6782. https://doi.org/10.1021/acs.chemrev.0c00170.

(316) Wang, J.; Polleux, J.; Lim, J.; Dunn, B. Pseudocapacitive Contributions to Electrochemical Energy Storage in TiO 2 (Anatase) Nanoparticles. *J. Phys. Chem. C* **2007**, *111* (40), 14925–14931. https://doi.org/10.1021/jp074464w.

(317) Augustyn, V.; Simon, P.; Dunn, B. Pseudocapacitive Oxide Materials for High-Rate Electrochemical Energy Storage. *Energy Environ. Sci.* **2014**, *7* (5), 1597–1614. https://doi.org/10.1039/c3ee44164d.

(318) Lasia, A. *Electrochemical Impedance Spectroscopy and Its Applications*; Springer New York: New York, NY, 2014. https://doi.org/10.1007/978-1-4614-8933-7.

(319) Barsoukov, E.; Macdonald, J. R. *Impedance Spectroscopy. Theory, Experiments, and Applications*, Second Edi.; Wiley-Interscience, 2005.

(320) Sacco, A. Electrochemical Impedance Spectroscopy: Fundamentals and Application in Dye-Sensitized Solar Cells. *Renew. Sustain. Energy Rev.* **2017**, *79* (12), 814–829. https://doi.org/10.1016/j.rser.2017.05.159.

(321) Gu, Y.; Zhang, B.; Fu, Z.; Li, J.; Yu, M.; Li, L.; Li, J. Poly (Vinyl Alcohol) Modification of Poly(Vinylidene Fluoride) Microfiltration Membranes for Oil/Water Emulsion Separation via an Unconventional Radiation Method. *J. Memb. Sci.* **2021**, *619*, 118792. https://doi.org/10.1016/j.memsci.2020.118792.

(322) Zante, G.; Boltoeva, M.; Masmoudi, A.; Barillon, R.; Trébouet, D. Lithium Extraction from Complex Aqueous Solutions Using Supported Ionic Liquid Membranes. *J. Memb. Sci.* **2019**, *580*, 62–76. https://doi.org/10.1016/j.memsci.2019.03.013.

(323) Rezania, B.; Severin, N.; Talyzin, A. V; Rabe, J. P. Hydration of Bilayered Graphene Oxide. *Nano Lett.* **2014**, *14* (7), 3993–3998. https://doi.org/10.1021/nl5013689.

(324) Konkena, B.; Vasudevan, S. Understanding Aqueous Dispersibility of Graphene Oxide and Reduced Graphene Oxide through p K a Measurements. *J. Phys. Chem. Lett.* **2012**, *3* (7), 867–872. https://doi.org/10.1021/jz300236w.

(325) Mansur, H. S.; Sadahira, C. M.; Souza, A. N.; Mansur, A. A. P. FTIR Spectroscopy Characterization of Poly (Vinyl Alcohol) Hydrogel with Different Hydrolysis Degree and Chemically Crosslinked with Glutaraldehyde. *Mater. Sci. Eng. C* **2008**, *28* (4), 539–548. https://doi.org/10.1016/J.MSEC.2007.10.088.

(326) Alsabbagh, A.; Aljarrah, S.; Almahasneh, M. Lithium Enrichment Optimization from Dead Sea End Brine by Chemical Precipitation Technique. *Miner. Eng.* **2021**, *170*, 107038. https://doi.org/10.1016/j.mineng.2021.107038.

(327) Schaller, J.; Headley, T.; Prigent, S.; Breuer, R. Potential Mining of Lithium, Beryllium and Strontium from Oilfield Wastewater after Enrichment in Constructed Wetlands and Ponds. *Sci. Total Environ.* **2014**, *493*, 910–913. https://doi.org/10.1016/j.scitotenv.2014.06.097.

(328) Lamberti, A.; Manfredi, D.; Calignano, F.; Pirri, C. F. TiO2 Nanotube-Based Smart 3D Electrodes by Anodic Oxidation of Additively Manufactured Ti6Al4V Structures. *Mater. Today Commun.* **2018**, *15* (March), 165–170. https://doi.org/10.1016/j.mtcomm.2018.02.009.

(329) Cao, C.; Yan, J.; Zhang, Y.; Zhao, L. Stability of Titania Nanotube Arrays in Aqueous Environment and the Related Factors. *Sci. Rep.* **2016**, *6* (1), 23065. https://doi.org/10.1038/srep23065.

(330) Borghols, W. J. H.; Lützenkirchen-Hecht, D.; Haake, U.; van Eck, E. R. H.; Mulder, F. M.; Wagemaker, M. The Electronic Structure and Ionic Diffusion of Nanoscale LiTiO2 Anatase. *Phys. Chem. Chem. Phys.* **2009**, *11* (27), 5742–5748. https://doi.org/10.1039/b823142g.

(331) Li, J.; Tang, Z.; Zhang, Z. Layered Hydrogen Titanate Nanowires with Novel Lithium Intercalation Properties. *Chem. Mater.* **2005**, *17* (23), 5848–5855. https://doi.org/10.1021/cm0516199.

(332) Zhu, K.; Wang, Q.; Kim, J.; Pesaran, A. A.; Frank, A. J. Pseudocapacitive Lithium-Ion Storage in Oriented Anatase TiO 2 Nanotube Arrays. *J. Phys. Chem. C* **2012**, *116* (22), 11895–11899. https://doi.org/10.1021/jp301884x.

(333) Kavan, L.; Kalbáč, M.; Zukalová, M.; Exnar, I.; Lorenzen, V.; Nesper, R.; Grätzel, M. Lithium Storage in Nanostructured TiO 2 Made by Hydrothermal Growth. *Chem. Mater.* **2004**, *16* (3), 477–485. https://doi.org/10.1021/cm035046g.

(334) Zaccagnini, P.; Baudino, L.; Lamberti, A.; Alexe-Ionescu, A. L.; Barbero, G.; Evangelista, L. R.; Pirri, C. F. Electrode Polarization in the Presence of a First Order Ionic Trapping Reaction. *J. Electroanal. Chem.* **2022**, *918*, 116499. https://doi.org/10.1016/j.jelechem.2022.116499.

(335) Evangelista, L. R.; Lenzi, E. K. *Fractional Diffusion Equations and Anomalous Diffusion*; Cambridge University Press: Cambridge, 2018. https://doi.org/10.1017/9781316534649.

(336) Gu, S.; Ji, B.; Qi, Q.; Wang, J.; Zhou, H.; Zhang, Y.; Luo, G. The Effects of Irradiation and High Temperature on Chemical States in Li2TiO3. *Int. J. Hydrogen Energy* **2019**, *44* (60), 32151–32157. https://doi.org/10.1016/j.ijhydene.2019.10.121.

(337) Ismail, I.; Noda, A.; Nishimoto, A.; Watanabe, M. XPS Study of Lithium Surface after Contact with Lithium-Salt Doped Polymer Electrolytes. *Electrochim. Acta* **2001**, *46* (10–11), 1595–1603. https://doi.org/10.1016/S0013-4686(00)00758-1.

(338) Deschanvres, A.; Raveau, B.; Sekkal, Z. Mise En Evidence et Etude Cristallographique d'une Nouvelle Solution Solide de Type Spinelle Li1+xTi2-XO4 0 ≤ x ≤ 0, 333. *Mater. Res. Bull.* **1971**, *6* (8), 699–704. https://doi.org/10.1016/0025-5408(71)90103-6.

(339) Steiner, D.; Auer, A.; Portenkirchner, E.; Kunze-Liebhäuser, J. The Role of Surface Films during Lithiation of Amorphous and Anatase TiO2 Nanotubes. *J. Electroanal. Chem.* **2018**, *812*, 166–173. https://doi.org/10.1016/j.jelechem.2017.11.035.

(340) Olsen, G.; Ulstrup, J.; Chi, Q. Crown-Ether Derived Graphene Hybrid Composite for Membrane-Free Potentiometric Sensing of Alkali Metal Ions. *ACS Appl. Mater. Interfaces* **2016**, *8* (1), 37–41. https://doi.org/10.1021/acsami.5b11597.

(341) Atkins, P.; De Paula, J. *Physical Chemistry*, Ninth Edit.; W.H. Freeman and Company: New York, 2010.